NTNU – Trondheim
Norwegian University of
Science and Technology

Evaluation of Welded Clad Pipe

Microstructures and Properties

Helena Bjaaland

Materials Science and Engineering
Submission date: June 2015
Supervisor: Odd Magne Akselsen, IPM
Co-supervisor: Vigdis Olden, SINTEF Materialer og Kjemi

Norwegian University of Science and Technology
Department of Engineering Design and Materials

Preface

This master's thesis is carried out at the Department of Engineering Design and Materials at the Norwegian University of Science and Technology (NTNU). The thesis is submitted as part of the Materials Science and Engineering master's program. The responsible supervisor at NTNU has been adjunct professor Odd Magne Akselsen. Co-supervisor from SINTEF Materials and Chemistry has been Dr. Vigdis Olden.

The thesis is part of the SINTEF ROP (**r**epair c**o**ntingency of **p**ipelines) project, and is a continuation of a summer job and project work within said project. Samples have been supplied by Technip Orkanger AS. The project description and formal requirements are given in Appendix F, and the risk assessment for the experimental work is presented in Appendix G.

I would like to thank my supervisor Odd Magne Akselsen and co-supervisor Vigdis Olden at SINTEF Materials and Chemistry for helpful feedback, constructive conversations and guidance throughout this semester. This thesis could not have been completed without their support and knowledge. Additionally, I would like to express my gratitude to senior engineer Ragnhild Sæterli and adjunct professor John Walmsley at the Department of Physics at NTNU. Their help and guidance with TEM investigations has been pivotal to this thesis. I also want to thank everybody at SINTEF Materials and Chemistry who has helped me, either in the laboratory or regarding the theoretical aspects of the thesis. To Nils-Inge Nilsen, Bård Nyhus, Hans Lange, Antonio Alvaro, Elin Pettersen, Benedicte Adelheide and Birgitte Karlsen, I express my deepest gratitude.

Declaration

I hereby declare that this work has been carried out independently and according to the examination regulations of The Norwegian University of Science and Technology (NTNU).

Trondheim, June 11th, 2015

Helena Bjaaland

Helena Bjaaland

Abstract

Clad pipes are used in the oil and gas industry for transportation of corrosive substances. Maintenance, repairs and tie-in connections to existing subsea structures is done by hyperbaric welding. There is per today no repair contingency available for clad pipes, so that a knowledge basis must be established in order to maintain pipeline integrity. Welding of clad pipes can result in a variety of complex microstructures due to the presence of dissimilar alloys. The difference in chemical composition and thermal properties will influence the integrity of the welded joint, and may result in a crack susceptible microstructure.

Previous work has shown that carbon migration and subsequent carbide precipitation in the clad, mainly during production, results in a hardened region in the clad. After welding, this region is susceptible to cracking. However, adding a Ni-interlayer between the clad and base metal (BM) provides a solution to the cracking related to the formation of a hard zone in the clad. Nevertheless, cracks may also arise from hydrogen charging from welding or from cathodic protection (CP) or H_2S during service, so that the cold cracking mechanisms of clad pipes is still highly relevant.

In this master's thesis, clad pipes with and without a Ni-interlayer have been investigated. The dissimilar interface region and carbides in the clad adjacent to the interface have been investigated using scanning electron microscope (SEM) and transmission electron microscope (TEM). The clad immediately adjacent to the interface contained $Cr_{23}C_6$ carbides, present both inside grains and at grain boundaries. The dissimilar interface showed a jagged distribution of Ni towards the clad side and segregation of Cr to carbides. The dissimilar interface showed a lath-like structure, however, there was no clear evidence of martensite. This should be further investigated.

Slow strain rate (SSR) testing was successfully performed on miniature compact tension (CT) specimens in air and under CP to evaluate the fracture mechanical properties of the dissimilar interface, with respect to material combination and environment. Generally, samples without a Ni-interlayer tested in air showed the highest fracture toughness values, followed by samples with a Ni-interlayer tested in both air and under CP. The lowest fracture toughness values were obtained for samples without a Ni-interlayer tested under CP. Samples with a Ni-interlayer showed an average reduction in CTOD of 7 % in the presence of hydrogen. The minute effect of hydrogen is attributed to the samples failing mainly in the softer Ni-interlayer close to the BM, which has low susceptibility to hydrogen embrittlement (HE). Samples without a Ni-interlayer showed an average reduction in CTOD of 77 % in the presence of hydrogen. The samples failed mainly in the decarburized BM adjacent to the interface, and along the interface. None of the samples failed in the previously suspected crack susceptible region in the clad. Future work should focus on determining the mechanisms behind cracking in the clad by physical weld simulations combined with fracture mechanical testing, and numerical weld simulations to assess any residual stresses.

Abstract (Norwegian)

Clad-rør brukes i olje- og gassindustrien til transport av korrosive substanser. Vedlikehold, reparasjoner og tilkobling til eksisterende subsea-strukturer gjøres ved hyperbarisk sveising. Det finnes per i dag ingen reparasjonsprosedyrer for clad-rør, slik at det er nødvendig å etablere en kunnskapsbasis for undervannsreparasjon av rørledninger for å sikre integriteten til rørledningssystemet. Sveising av clad-rør kan føre til dannelse av komplekse mikrostrukturer, grunnet bruken av ulike legeringer. Forskjeller i kjemisk sammensetning og ulike termiske egenskaper vil påvirke integriteten til den sveiste komponenten, og kan føre til en mikrostruktur som er utsatt for sprekkdannelse.

Tidligere arbeid har vist at karbonmigrasjon med påfølgende karbidutfelling i clad, hovedsakelig under produksjon, fører til dannelsen av en hard sone i clad. Denne sonen er utsatt for sprekkdannelse etter sveising. Ved å ha et Ni-belegg mellom clad og rørstål forhindrer man sprekkdannelsen relatert til dannelsen av en hard sone i clad, men sprekker kan også oppstå som følge av hydrogenopplading fra sveising, katodisk beskyttelse eller H_2S under drift. Kaldsprekkingsproblematikken relatert til cladrør er derfor høyst relevant.

Denne masteroppgaven har undersøkt cladrør med og uten Ni-belegg. Grenseflaten mellom clad og rørstål, samt karbider i clad nærliggende grenseflaten er undersøkt ved hjelp av skanning elektron-mikroskop (SEM) og transmisjons elektron-mikroskop (TEM). Området i clad helt inntil grenseflaten inneholdt $Cr_{23}C_6$-karbider. Karbidene ble observert både på korngrenser og inni korn. Grenseflaten viste en ujevn og taggete fordeling av Ni mot clad-siden, samt segregering av Cr til karbider. Grenseflaten viste en nålelignende struktur, men det er ikke påvist martensitt. Dette bør undersøkes nærmere.

Vellykkede bruddmekaniske tester ble utført på miniatyrprøver i luft og under katodisk beskyttelse for å evaluere de bruddmekaniske egenskapene til grenseflaten mellom clad og rørstål. Prøver uten Ni-belegg tested i luft hadde høyest bruddseighet, etterfulgt av prøver med Ni-belegg testet i luft og under katodisk beskyttelse. Prøver uten Ni-belegg tested under katodisk beskyttelse resulterte i lavest bruddseighet. Gjennomsnittlig reduksjon i CTOD for prøver med Ni-belegg var 7 %. Den minimale effekten av hydrogen er i dette tilfellet tilllagt det faktum at sprekken hovedsakelig propagerte i det noe mykere Ni-belegget, som er lite mottakelig for hydrogensprøhet. Prøver uten Ni-belegg viste en gjennomsnittlig reduksjon i CTOD på 77 % når hydrogen var tilstede. Sprekken propagerte her i den dekarburiserte sonen i rørstålet inntil grenseflaten, samt langs grenseflaten. Ingen av prøvene hadde sprekkvekst i clad, som tidligere ble ansett som en sårbar sone. Videre arbeid bør fokusere på å kartlegge mekanismene bak sprekkdannelse i clad ved å foreta fysiske sveisesimuleringer kombinert med bruddmekanisk testing, samt numerisk sveisesimulering for å evaluere eventuelle restspenninger.

List of abbreviations

BCC – Body centered cubic

BCT – Body centered tetragonal

BM – Base metal

BSE – Backscattered electrons

CCT – Continuous cooling transformation

CMOD – Crack-mouth opening displacement

CP – Cathodic protection

CRA – Corrosion resistant alloy

CT – Compact tension

CTE – Coefficient of thermal expansion

CTOD – Crack-tip opening displacement

EDM – Electro-discharge machining

EDS – Energy-dispersive spectroscopy

EMPA – Electron microprobe analysis

EPFM – Elastic plastic fracture mechanics

FCC – Face centered cubic

FIB – Focused ion beam

FPZ – Fracture process zone

HAC – Hydrogen assisted cracking

HAZ – Heat affected zone

HCP – Hexagonal close packed

HE – Hydrogen embrittlement

HEAC – Hydrogen-environment-assisted-cracking

HEDE – Hydrogen-enhanced decohesion

HELP – Hydrogen-enhanced localized plasticity

HISC – Hydrogen induced stress cracking

HSLA – High-strength low-alloy

IHAE – Internal-hydrogen-assisted-cracking

LEFM – Linear elastic fracture mechanics

LOM – Light optical microscope

NTNU – Norwegian University of Science and Technology

PMZ – Partially mixed zone

PWHT – Post-weld heat treatment

QT – Quenched and tempered

ROP – Repair contingency of pipelines

SAD – Selected-area diffraction

SE – Secondary electrons

SEM – Scanning electron microscope

SENB – Single-edge notched bend

SSR – Slow strain rate

STEM – Scanning transmission electron microscope

TEM – Transmission electron microscope

TMCP – Thermo-mechanical controlled process

Table of Contents

1. Introduction

1.1. Background

In 2013 Norway produced 213.7 million Sm^3 of profitable petroleum. As this illustrates, the oil and gas industry is an important source of income for Norway. The pipeline systems are a very important part of the infrastructure for transporting petroleum. The Norwegian oil and gas pipeline system consists of over 8000 km of pipelines, and has a capacity of transporting 120 billion Sm^3 per year.[1]

The transportation of unprocessed oil, gas and condensate at high pressure and temperature may result in a very aggressive environment. Substances such as H_2S, CO_2 and water yield high corrosivity, and may also result in hydrogen induced cracking and sulphide stress corrosion cracking. In addition, cathodic protection (CP) systems may provide an additional source of hydrogen. In order for the pipelines to withstand corrosion and environmental cracking during service life, a corrosion resistant interior is required.[2]

1.2. Challenges and Motivation

Cladding is often used in the oil and gas industry as a means against corrosion and wear, typically for pipelines containing unprocessed hydrocarbons.[3] An alloy is applied to a backing material, and the two components form a metallurgical bond.[4] By depositing a layer of corrosion resistant alloy (CRA) onto carbon steel, the material cost is greatly reduced compared to that of a component made of solid CRA. During girth welding, the bimetallic nature of the clad pipe, in combination with the use of highly alloyed austenitic filler metals, may result in complex metallurgical reactions. Nickel based fillers are often used, adding to the complexity of the situation.

Clad pipes, as shown in Figure 1, make up a large part of the pipeline infrastructure in Norway and Europe, and there is as per today no repair contingency available for these bi-metallic pipes when applied subsea.

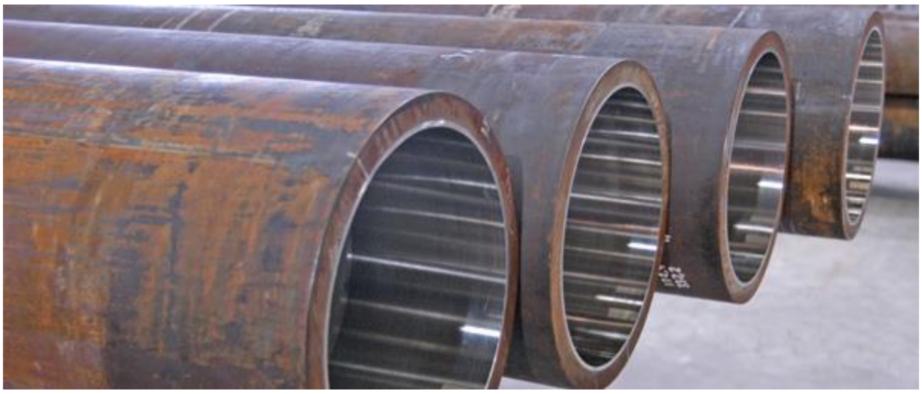

Figure 1 - Clad pipes prior to girth welding.[5]

A fundamental understanding of the effect of welding and the degradation mechanisms of bi-metallic pipes must therefore be established, in order to provide procedures and specifications for subsea repair welding. This work is part of the ROP project (**r**epair c**o**ntingency of **p**ipelines), which is an industrial research program within the Petromaks 2 Programme of the Research Council of Norway. Industrial partners include Statoil Petroleum AS, Gassco AS, Technip Norge AS, Pohang Iron and Steel Company and EDF Induction. SINTEF, The Norwegian University of Science and Technology (NTNU) and Institute for Energy Technology are responsible for the research. [6]

Initially, the focus of this work was directed towards the influence of welding on clad pipes. However, discoveries made in the preceding work, which is summarized below, led the focus towards the properties of the dissimilar interface. Additionally, sample preparation and investigation, especially for transmission electron microscopy (TEM) turned out to be far more complicated and time consuming than expected.

Preceding work has investigated the metallurgical reactions occurring during welding of clad pipes and shown that the formation of a hard and crack susceptible zone in the clad is attributed to carbon diffusion (mainly) during production. The formation of this hard zone, and thus cracking in the clad, is thought to be prevented by depositing a Ni-interlayer between the clad and base metal (BM), which prevents carbon diffusion and accumulation, and subsequently carbide precipitation in the clad. This work aims to characterize the dissimilar interface and the hardened region in the clad, in addition to investigating the fracture mechanical aspects of the clad-BM interface. With respect to fracture toughness, samples with and without a Ni-interlayer are investigated. As these pipes are protected by CP, and additionally contains corrosive substances, such as H_2S, the effect of hydrogen will also be investigated. As stated above, the work of this thesis has been focused more towards the dissimilar interface rather than the aspects related to welding, based on previous findings and complications during investigations. Thus, a thorough characterization of the clad crack appearance and morphology and weld metal carbides and intermetallic phases has not been performed.

1.3. Thesis Structure

The thesis is comprised of 8 main chapters, including this introduction. The theoretical background wishes to introduce and explain the relevant theory and mechanisms regarding the investigated aspects. A chapter regarding previous investigations is included in order to provide a more complete background for this thesis. The experimental procedure presents the materials, instruments and procedures which form the basis for the investigations. The results section presents the findings of this work, which is discussed and interpreted in the discussion chapter. The results are summarized in the conclusion chapter, followed by suggestions for further work.

2. Theoretical Background

The following chapters give an introduction to the challenges regarding the use of clad pipes, both with respect to metallurgy and mechanical properties, in addition to the selected experimental techniques. As this thesis is a continuation of a project work, some parts of the theoretical background is taken directly from said project.

2.1. Clad Pipes

According to DNV-OS-F101 [7] a clad pipe is defined as *"a pipe with internal (corrosion resistant) liner where the bond between (linepipe) backing steel and cladding material is metallurgical"*. Clad pipes combine the superior mechanical properties of the backing steel with the corrosion resistance of the clad material, thus providing the required properties at a reduced cost.[4] The backing steel is usually a high-strength-low-alloy (HSLA) steel, such as X52, X60 and X65. The cladding material is a corrosion resistant alloy (CRA), such as austenitic stainless steel 316L, or nickel alloys Inconel 625 and Inconel 825. The clad layer is relatively thin, around 3 mm, as CRAs are relatively expensive.[8]

Clad pipes are usually made from clad plates produced by hot roll bonding. Depending on the backing steel, the process is either done via a thermo-mechanical controlled process (TMCP) with accelerated cooling, or hot rolling followed by quenching and tempering (QT). The clad plates are typically manufactured by the "sandwich method", in which two plates of CRA are placed between two plates of carbon steel, like a sandwich. The edges of the sandwich package are welded in order to keep the components together. The package is designed to be airtight, even at elevated temperatures, and any oxygen present inside is evacuated in order to prevent the formation of oxides. A ceramic powder is placed between the two CRA plates as a separating compound. Chromium or zirconium oxide is placed between CRA and base metal. The sandwich is heated and hot rolled. The high temperature and deformation result in decomposition of these oxides, allowing the exposed metallic surfaces to bond metallurgically. Thus, oxides may be found evenly distributed close to the bonding interface.[4, 8]

Upon completing the hot roll bonding process, with the corresponding heat treatment, the weld frame is removed, resulting in two clad plates. The clad plates are bent into the shape of a pipe in a press bending process, followed by longitudinal welding. The completed pipe section is approximately 12 m long. Inspection and non-destructive testing is performed as a final step before girth welding.[4, 7, 8]

Microalloyed low-carbon steels have high strength and toughness, in addition to good weldability, and are therefore often used for pipeline applications.[9] The carbon content is typically low, in order to ensure good weldability, and microalloying elements such as Nb, V and Ti are added to improve the mechanical properties. As mentioned above, pipeline steels are typically produced by thermo-mechanical-controlled-processing (TMCP), but can also be produced by quenching and tempering (QT). For TMPC steels, accelerated cooling and deformation without recrystallization result in a fine grained microstructure yielding excellent strength and toughness. For QT steels, the deformation is done above the recrystallization temperature, followed by quenching and tempering.[4, 8, 10]

2.2. Steel Metallurgy

The microstructure of steels is highly dependent on chemical composition and thermo-mechanical procedure. In order to understand more complex alloying systems of steels, a fundamental understanding of the Fe-C system is required. Ferrite (α), austenite (γ) and cementite (Fe_3C) represent the equilibrium phases of steel, provided sufficiently slow cooling, as can be seen in Figure 2. A_1 denotes the temperature at which the eutectoid reaction occurs, and A_3 denotes the temperature of the austenite-ferrite transformation. A_3 will vary with carbon content, as the equilibrium diagram illustrates.[11]

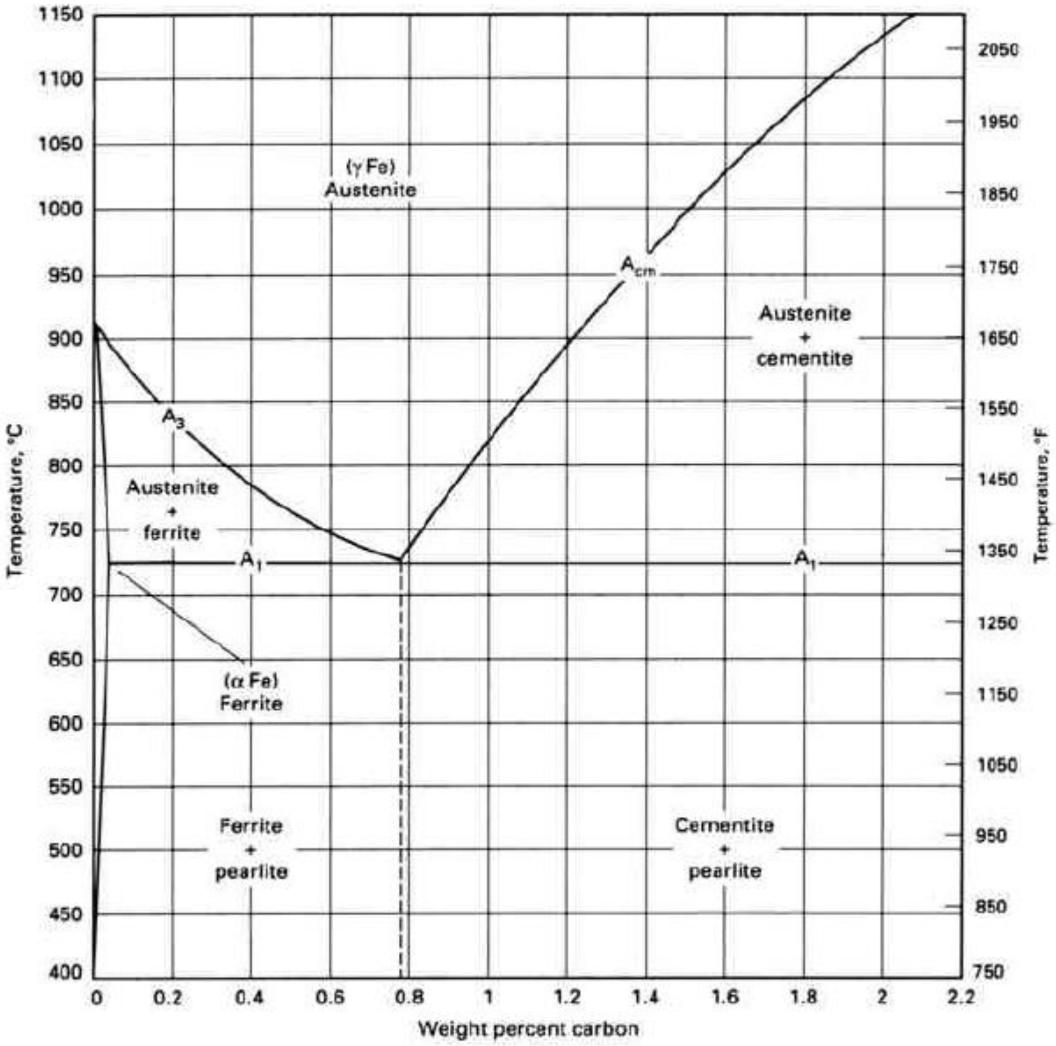

Figure 2 - Fe-C equilibrium diagram for low carbon content.[12]

Under equilibrium conditions, steels containing less than 0.8 wt% C consist mainly of ferrite and pearlite. Upon reaching A_3 during cooling, ferrite starts to form on the austenite grain boundaries. Ferrite has low solubility of carbon, meaning that the residual austenite is enriched in carbon until the eutectic temperature and composition is reached. At this stage, the remaining austenite transforms into pearlite, which has a lamellar structure consisting of ferrite and cementite.[10, 11]

Ferrite has a body centered cubic (BCC) crystal structure, whereas austenite has a face centered cubic (FCC) structure. This influences the solubility of carbon, as can be seen from the equilibrium diagram; austenite has a solubility of carbon almost a hundred times that of ferrite. This is an important aspect during heat treatment of steels.[11]

For steels who are subjected to more rapid cooling rates, the equilibrium diagram is not directly applicable, as it does not include the metastable phases which form at higher degrees of undercooling, such as upper and lower bainite, and martensite.[11] The transformations occurring during continuous cooling from the austenite region are best presented using a CCT-diagram (continuous cooling transformation), as seen in Figure 3.[13]

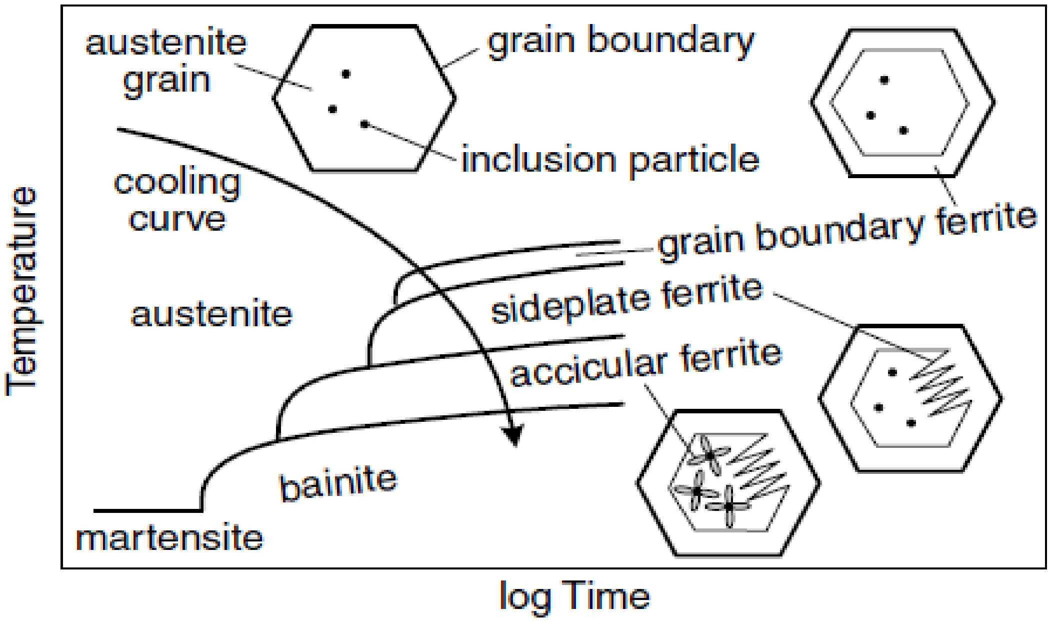

Figure 3 - Continuous-cooling transformation diagram for weld metal of low-carbon steel.[14]

Each transformation product from austenite has a “nose” in the diagram, except martensite, which does not depend on time, as seen in Figure 3. The temperature at which martensite formation starts is known as M_S. It should be noted that deformation may facilitate martensite formation by raising the M_S-temperature. Martensite is an important non-equilibrium microstructure, which will be discussed in more detail in 2.3.3. The curved arrow line represents a certain cooling rate. Different cooling rates will thus result in different combinations of microstructures. The addition of alloying elements has a tendency to shift the transformation curves towards longer times, i.e. to the right, in addition to lowering the temperature at which the transformations occur.[10]

For austenitic stainless steels, chromium and nickel are the main alloying elements. Adding chromium (> 10.5 wt%) provides corrosion protection by the formation of an oxide film. The addition of nickel expands the austenite region, making austenite stable over a wider range of temperatures. Chromium has the opposite effect, so that a balance must be obtained. In Fe-Cr-Ni systems, however, chromium slows down the kinetics of the austenite-ferrite transformation. The correct balance of alloying elements can thus allow for austenite to be stable at room temperature. Austenitic stainless steels have good corrosion resistance and low temperature ductility, but may be subjected to degradation by carbide precipitation during heat treatment.[15]

As this illustrates, the metallurgy of steels is intricate, and exposure to elevated temperatures may result in numerous and complex microstructural changes. For bimetallic components, such as clad pipes, the situation is further complicated due to the presence of materials with dissimilar chemical composition and physical properties.

2.3. Dissimilar Joints at Elevated Temperatures

In the literature, welding of bimetallic components typically addresses dissimilar transition joints, i.e. a ferritic component joined to an austenitic component, or alloys cladded with a CRA via a weld overlay process. This is not directly applicable to clad pipes, as the clad is not in the molten state during the manufacturing process, but is still used as a basis for explaining the metallurgical changes, as a lot of the same mechanisms occur for both systems. However, post-weld heat treatment (PWHT) of dissimilar welds is highly applicable for explaining the metallurgical reactions in clad pipes. An overview of the most common microstructural changes and challenges regarding exposure of ferritic-austenitic dissimilar metals to elevated temperatures follows.

Another important aspect of dissimilar joints and exposure to elevated temperature is the difference in thermal properties. Ni-based filler metals generally have a coefficient of thermal expansion (CTE) between the CTE of austenitic stainless steel and carbon steel, resulting in a better distribution of thermal stresses.[16] This is briefly presented in section 2.3.4.

2.3.1. Diffusion of Alloying Elements

Bimetallic components that are exposed to elevated temperatures may experience a change in chemical composition close to the interface. Austenitic stainless steels and Ni-based alloys generally have a high content of alloying elements such as Ni, Cr and Mo, and a low C content. Ferritic steels are low alloyed, but have higher carbon content. Due to this difference in chemical composition, alloying elements will diffuse across the interface to reduce the concentration gradient.[17]

Migration of alloying elements may occur during welding, post-weld heat treatment (PWHT) or during operation at elevated temperatures, and may alter the microstructure and properties of the component. For clad pipes, this may also occur during the production process, i.e. during the hot-roll bonding of the clad plates. The diffusion of carbon is particularly influential. At elevated temperatures, carbon diffuses from the carbon-rich ferrite to the austenite, given the proper time temperature and carbon content. The result is a softer, carbon depleted zone in the ferrite, and a hard, carbon enriched zone in the austenite. The extent of carbon migration depends on the solubility and diffusion rate of carbon in the respective microstructure. Generally, carbon diffuses more rapidly in ferrite, but ferrite has much lower carbon solubility than austenite. Austenite stabilizing elements such as nickel will influence the solubility of carbon, and generally slow down the migration of carbon from the ferrite.[18]

In the carbon enriched region, Cr-carbides may precipitate at the austenite grain boundaries. This renders the austenite susceptible to intergranular cracking close to the dissimilar interface. Hydrogen, either introduced during welding or during service from CP or H_2S, can diffuse into the weldment. This may result in cold cracking, which often occurs along the austenite grain boundaries.[19] Regarding clad pipes, some clad components have a Ni-plating between the base metal and the clad. This plating gives better bonding properties, prevents carbon migration, thus reducing the risk for high hardness and cold cracking.[20, 21] X65 steel clad with austenitic stainless steel 316L, both with and without a Ni-interlayer, has previously been investigated [22] in the un-welded condition. Without the Ni-interlayer, the average hardness in the clad adjacent to the interface was 350 HV0.025, and with the Ni-interlayer the average hardness was 210 HV2. The sample without the Ni-interlayer also showed severe grain boundary precipitation compared to the sample with the Ni-interlayer.

Cracking or disbonding in ferritic-austenitic dissimilar joints usually occurs near the fusion line. The failure is thought to be attributed to the formation of martensitic bands, either due to diffusion of alloying elements or dilution, carbon diffusion during PWHT, carbide precipitation and hydrogen pick-up. Regarding martensite formation, austenite stabilizers such as Ni will allow austenite to form at lower temperatures, which in turn facilitates martensite formation upon cooling.[23]

2.3.2. Carbide Precipitation in Stainless Steels

Carbides may precipitate in stainless steels as a consequence of exposure to elevated temperatures. Rapid cooling of austenitic stainless steel from the solution annealing temperature (> 1000 ˚C) will allow for the dissolved carbide to remain in solution. However, any subsequent heat treatment at sufficiently high temperatures for sufficiently long periods of time, may result in carbide precipitation, as seen from the Fe-Cr phase diagram in Figure 4.[24]

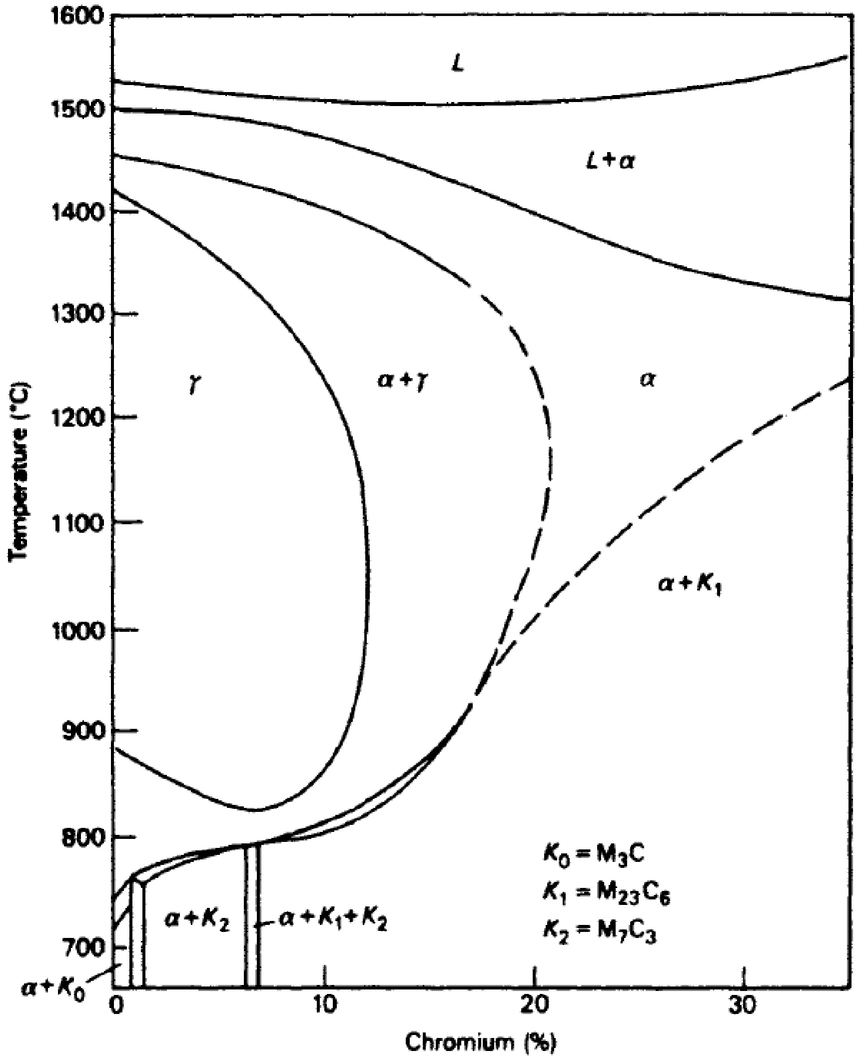

Figure 4 - Phase diagram for the Fe-Cr system (0.05 wt% carbon).[15]

As illustrated in Figure 4, there are several different types of carbides which may precipitate in Fe-Cr alloys. The most common carbide found in unstabilized stainless steels in the 300 series is $M_{23}C_6$, whereas M_7C_3 is typically only found at high carbon levels. Grain boundary precipitation, which is only preceded by precipitation at the austenite-ferrite interfaces, can occur quite rapidly, and has detrimental effects on the toughness, ductility and corrosion resistance of the material. Additionally, $M_{23}C_6$ carbides may precipitate at inclusions and twin boundaries.[24]

Precipitation of $M_{23}C_6$ on grain boundaries tends to occur on dislocations, which may be piled up against grain boundaries, or on ledges on the grain boundary.[24] Investigations [25] performed on quenched and aged AISI 316L stainless steel showed more rapid precipitation of $M_{23}C_6$ in specimens that were deformed before ageing. The $M_{23}C_6$ carbides tend to have a parallel orientation with the matrix.[15, 26]

The $M_{23}C_6$ carbide is most commonly present as $Cr_{23}C_6$, but elements such as Fe and Mo can substitute for Cr. The crystal structure of $Cr_{23}C_6$ is a complex face centered cubic with a lattice parameter a = 10.65 Å, approximately three times that of the FCC lattice. In addition to $M_{23}C_6$, M_6C carbides may also be found in stainless steels containing Mo or Nb. (The stainless steel investigated in this work contains approximately 2-3 wt% Mo.) However, in 316 stainless steel, M_6C is typically only found after long ageing times, forming from the $M_{23}C_6$ carbide.[24] Crystallographic information regarding the clad (austenite), BM (ferrite) and potential carbides is presented in Table 1.

Grain boundary precipitation of $Cr_{23}C_6$ carbides is known as sensitization, and may occur in the temperature range 450-850 °C for stainless steels. The precipitation kinetics of $Cr_{23}C_6$ is illustrated in Figure 5, showing the effect of carbon content. Sensitization is reduced by selecting a low-carbon grade steel (< 0.03 wt% C)[15] and/or adding stabilizing elements, such as V, Ti or Nb. These elements are strong carbide formers, resulting in the formation of MC carbides, which improves the mechanical properties, in preference to $M_{23}C_6$ carbides.[27] Applying the proper heat treatment, i.e. avoiding exposure in the critical temperature range, is also an option.[10]

Shushan et al. [28] investigated diffusion bonded carbon steel – stainless steel, and found that the high temperature bonding process resulted in Cr carbide precipitation at the interface and on grain boundaries in the clad.

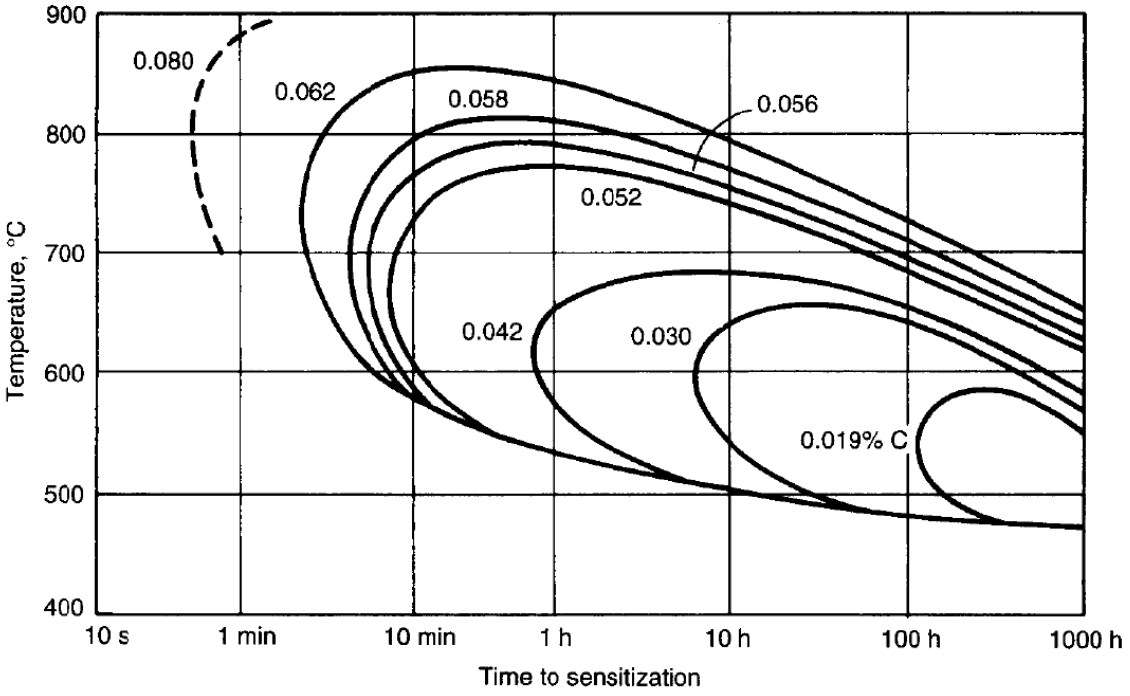

Figure 5 - Precipitation kinetics of $Cr_{23}C_6$ carbide as a function of carbon content.[29]

Table 1 - Crystal structures and composition of phases in austenitic stainless steels. Adapted from [24].

Phase	**Crystal structure**	**Lattice parameters (Å)**	**Composition**
Austenite	FCC	a = 3.598	-
Ferrite	BCC	a = 2.85-2.88	FeCrMo
Carbides:			
M_7C_3	pseudo-hexagonal	a = 6.928-6.963 c = 4.541-4.511	Cr_7C_3; $(FeCr)_7C_3$; $(Fe0.6Cr0.4)_7C_3$
$M_{23}C_6$	FCC (complex)	a = 10.57-10.68	$(Cr_{16}Fe_5Mo_2)C_6$; $(FeCr)_{23}C_6$; $(Cr_{17}Fe_{4-5}Mo_{1-5})C_6$
M_6C	FCC (diamond type)	a = 10.95-11.28	$(CrCoMoNi)_6C$; $(TiNi)_6C$; $(NbNi)_6C$; $(Fe_3Mo_3)C$

2.3.3. Martensite

Rapid quenching from the austenite region to room temperature may result in the formation of the hard phase that is martensite. Martensite is a form of ferrite, but where all the carbon is in solution in the new phase. The austenite phase has a higher solubility of carbon than ferrite, and prior to quenching the carbon is in solid solution in the austenite phase. The rapid cooling does not allow carbon diffusion and carbide precipitation, and the carbon is “locked” in solution in the new phase.

Formation of martensite involves a diffusionless shear transformation, in which the austenite lattice is deformed in a specific and homogeneous manner. As a result of this, martensite is highly crystallographic in character, and has the same chemical composition as the parent austenite. In order to reduce the strains from the constricting surroundings, martensite grows as thin plates or laths. In low carbon steels, martensite has a lath or plate like morphology.[30]

The martensitic transformation is typically an athermal process, i.e. a change in temperature is required to induce the process. The temperature at which the transformation starts is denoted M_s, and the temperature at which 95% of the martensitic transformation is completed is denoted M_f. The austenite which is not transformed to martensite is called retained austenite. The degree of undercooling below M_s determines the fraction transformed, with higher undercooling resulting in a higher fraction transformed. Deformation can have the same effect as temperature, as deformation has a tendency to increase M_s by altering the driving force behind the mechanism.[30] Austenitic stainless steel 316L has a metastable austenitic structure, meaning that martensite transformation may occur during cooling and/or during plastic deformation.[31]

To obtain martensite, the cooling rate from austenite must be sufficiently rapid in order to avoid all other phase transformations. Almost all alloying elements lower the M_s-temperature, meaning that the cooling rate required to form martensite in highly alloyed steels, such as 316L, may be rather slow compared to that of plain carbon steel. The effect of alloying elements on M_s-temperature is illustrated in equation 2.1. All element concentrations are given in wt%. It should be noted that this is an empirical equation and is not applicable to all types of steels. Regardless, it illustrates the principle sufficiently.[30]

$$M_s(^{\circ}C) = 539 - 423C - 30.4Mn - 17.7Ni - 12.1Cr - 7.5Mo \qquad (2.1)$$

Martensite has a body centered cubic (BCC) or body centered tetragonal (BCT) crystal structure; the tetragonality increases with increasing carbon content.[30] For the Fe-C system, martensite has a BCC structure when the carbon content is below 0.6 wt%. At higher carbon contents, the structure is found to be BCT.[32] Deformation induced martensite has a hexagonal closed packed (HCP) structure.[31] Regarding characterization of martensite by electron diffraction patterns, which is explained in section 2.7, distinction between low carbon martensite and ferrite may be difficult. The two phases both have a BCC structure, with very similar lattice parameters. The high dislocation density of martensite, however, can be utilized for distinction.[33]

Joining of dissimilar metals, either by welding or hot roll bonding, may result in the formation of a martensitic band at the interface.[28, 34] For stainless steel fillers, this band can be quite thick, whereas for Ni-based fillers, the martensitic band is typically quite narrow.[16] This is attributed to the variation in the main alloying elements (Fe, Ni, Cr) across the fusion line, resulting in a much steeper compositional gradient in Ni-based welds compared to austenitic stainless steel welds. This results in a variation in M_s-temperature, and thus a variation in martensite band width. An experiment [35] involving Alloy 625 and 309L filler metals deposited onto carbon steel, showed a significantly thicker martensitic band for the austenitic stainless steel weld (30-37 μm) compared to the Ni-based weld (1-3 μm). Again, this was attributed to the steep compositional gradient found in the Ni-carbon steel weldment, which lowered the M_s-temperature below room temperature over a short distance, resulting in a narrow area where martensite could form.

Gittos and Gooch [36] investigated the interface between stainless steel and nickel alloy claddings deposited onto $2^1/_4$Cr-1Mo steel by a weld overlay process, both in the as-welded condition and after post-weld heat treatment (PWHT). At the interface, in the partially mixed zone, a narrow martensitic band with peak hardness of 440 HV was observed after welding. During PWHT, carbon migration from the steel to the cladding occured, resulting in a decarburized region in the steel and carbide precipitation in the stainless steel cladding. The martensitic band at the interface decomposed during PWHT, however, high hardness was still observed in the cladding (500 HV over a distance of 100 µm from the interface), which was attributed to carbide precipitation and the formation of virgin martensite upon cooling from the PWHT-temperature. The formation of virgin martensite was thought to occur as a result of variation in M_s and A_1 temperatures in the diluted zone, and from carbon migration raising the M_s-temperature. The carbides close to the interface were identified to be Cr-rich $M_{23}C_6$ carbides by electron diffraction. After PWHT, feathery virgin martensite was observed on the clad side of the iterface. Microhardness indentations resulted in further martensite formation, as seen in Figure 6, indicating low stability of austenite in this region.

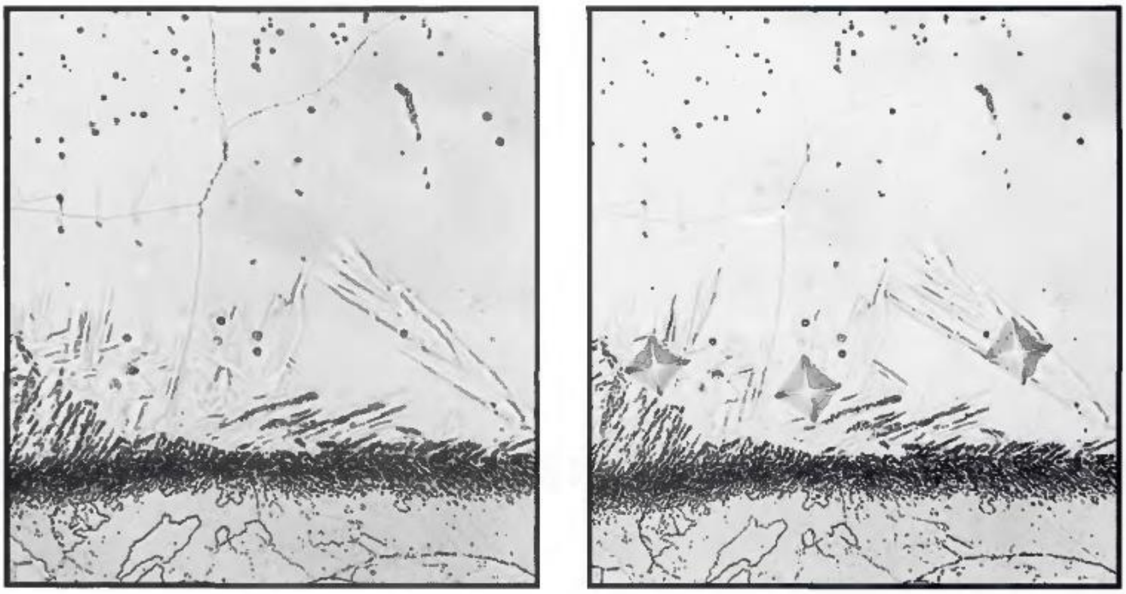

Figure 6 – Interface between 309L/347 stainless steel and 2^1/$_4$Cr-1Mo steel. PWHT 690 ˚C for 30 h. Etched in 2% Nital and electrolytically polished. Notice the formation of additional martensite laths at micorhardness indentations.[36]

2.3.4. Residual Stresses

Stresses that are present in an object in the absence of external loads is defined as residual stresses. Residual stresses can arise from material characteristic, or during manufacturing and service.[37] For dissimilar joints, such as clad pipes, the difference in thermal coefficient of expansion (CTE) between the clad and BM can result in residual stresses at the interface. The difference in CTE is greater for stainless steel – ferritic steel, than for Ni – ferritic steel.[18] Cooling from elevated temperatures can thus lead to tensile and shear stresses at the clad-BM interface.[38] The manufacturing of clad pipes involves several processes which can introduce residual stresses such as hot rolling, bending and welding. This, in combination with the presence of two materials with dissimilar physical properties, makes it complicated to get an overview of the situation.

2.4. Fracture Mechanical Aspects

Fracture occurs when the atomic bonds of a material are broken. This occurs when the applied stresses exceed the cohesive forces between the atoms.[39]

Fracture mechanics is the study of “the behavior of materials containing cracks or other small flaws”[40], and is typically used to estimate a critical flaw size (and geometry) for a given level of stress, in a given material at specific parameters. Flaws may be in the form of small pores, microcracks or inclusions. Most engineering materials contain flaws, to some extent, stressing the need for knowledge about the basic theories of fracture mechanics.[40]

Fracture mechanics can be divided into two categories; linear elastic fracture mechanics (LEFM) and elastic plastic fracture mechanics (EPFM). In LEFM, the material suffers elastic deformation. LEFM is valid as long as the plastic zone ahead of the crack tip is confined to a minute region. In EPFM, the material deforms plastically.[41]

2.4.1. Fracture Behaviour

Three of the most common fracture mechanisms in metals are illustrated in Figure 7 and explained briefly in the following paragraphs.

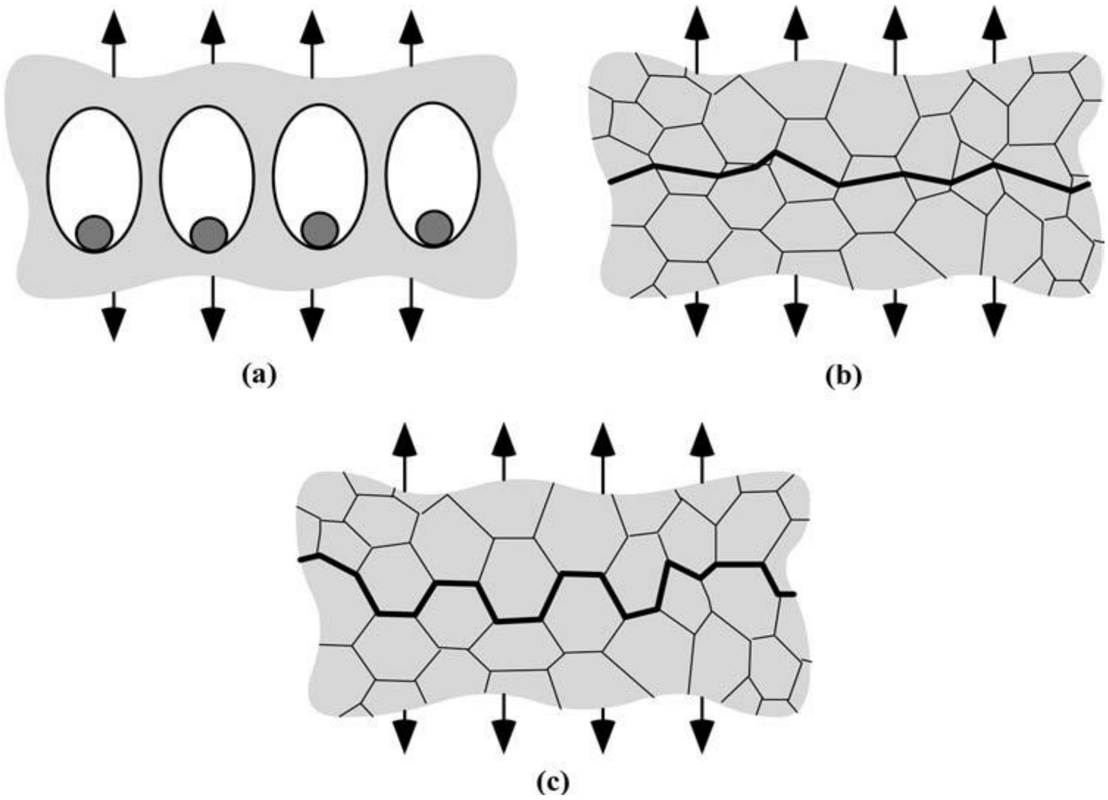

Figure 7 - Fracture mechanisms of metals: (a) ductile fracture, (b) cleavage fracture, (c) intergranular fracture.[42]

Ductile fracture occurs by nucleation, growth and coalescence of microvoids. These microscopic voids nucleate at second-phase particles and inclusions. The microvoids grow and form larger flaws, which eventually results in fracture. A dimpled fracture surface is characteristic of ductile fracture due to the formation of microvoids during the process, as seen in the left image in Figure 8. Materials which have failed by ductile fracture have typically suffered a substantial amount of deformation prior to fracture. The crack propagation is typically stable.[42]

Cleavage fracture involves rapid crack propagation along specific crystallographic planes, with little to no plastic deformation prior to fracture. The fracture path is transgranular, as the crack changes direction each time it encounters a grain boundary, in search of the most favorable cleavage plane. Brittle fracture is characterized as cleavage fracture, although cleavage fracture also can be preceded by ductile tearing. A cleavage fracture surface has a multifaceted appearance, with each facet consisting of a distinct grain. The individual facet may contain river patterns, in which ridges form in a fan-like manner from the origin of the crack.[40, 42] Figure 8 (right image) shows a brittle fracture with a cleavage like morphology.

A fracture surface containing planar facets could also indicate quasi-cleavage fracture, as seen in the right image in Figure 9. Quasi-cleavage is a term used to describe a fracture surface that bears a resemblance to cleavage fracture, but where the fracture has not propagated along specific crystallographic planes.[43] Quasi-cleavage is used in terms of describing fracture surface appearance; it is not defined as a fracture mechanism, such as microvoid coalescence, intergranular and cleavage fracture.[44]

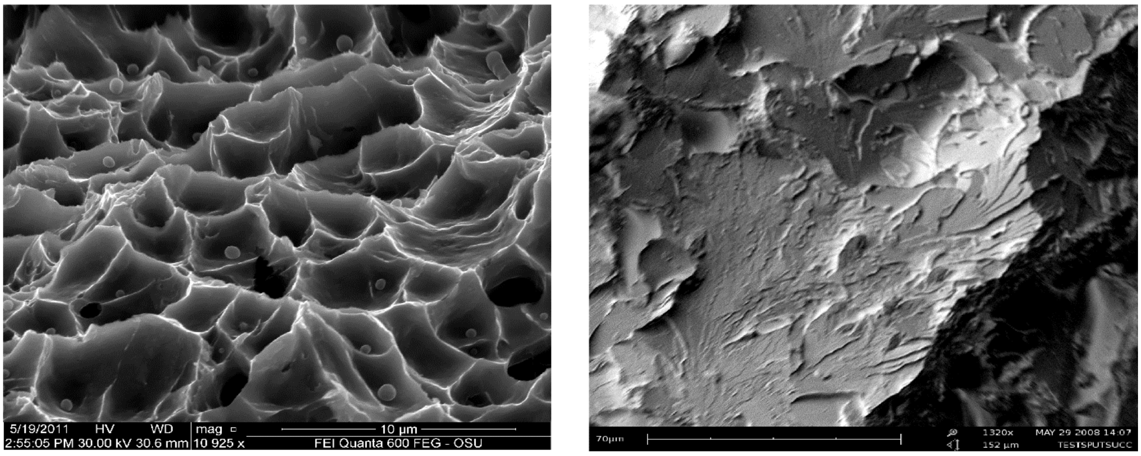

Figure 8 - Left: Ductile fracture showing dimples. Right: Brittle, transgranualar fracture.[45]

Intergranular fracture entails failure along the grain boundaries, and has a “rock candy” appearance, as seen in the left image in Figure 9. There are several mechanisms which may render the grain boundaries to be the preferred crack path, such as intergranular corrosion, environmentally assisted cracking and brittle phase precipitates at the grain boundaries.[42]

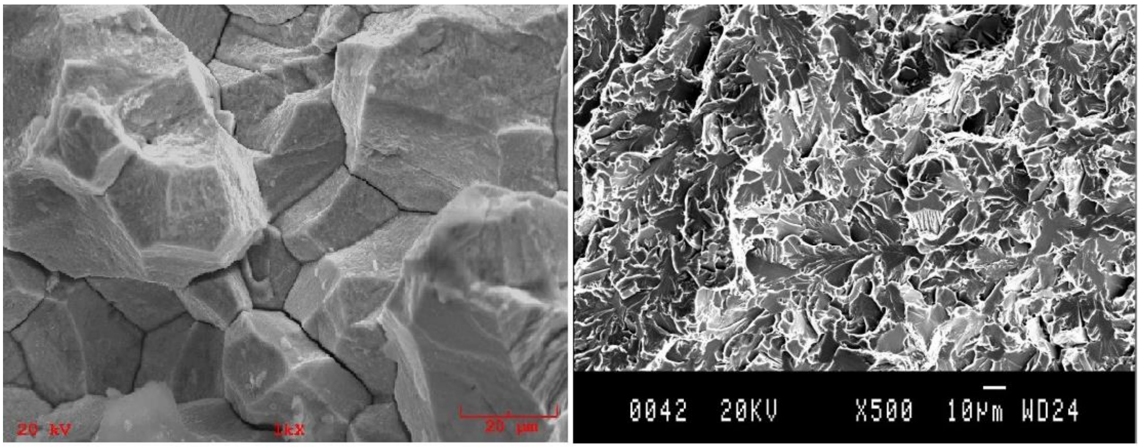

Figure 9 – Left: Intergranular fracture showing a "rock candy" appearance.[46] Right: Quasi-cleavage fracture surface in carbon steel.[47]

2.4.2. Fracture Toughness

Fracture toughness is a measure of a material’s resistance to fracture at a certain applied load in the presence of a flaw. The applied stress will concentrate and intensify at the flaw. The stress intensity factor, which expresses the stress distribution in front of the propagating crack, is given by equation 2.2

$$K = f\sigma\sqrt{\pi a} \tag{2.2}$$

where f is a geometry factor, σ is the applied stress and a is the flaw size. The K value at which fracture occurs is denoted as the critical stress intensity factor, K_c, and is a measure of fracture toughness. The unit for K_c is typically MPa√m. The fracture toughness tends to decrease with increasing sample thickness, until it reaches a constant value called plane strain fracture toughness K_{Ic}.[40] The subscript *I* refers to the type of loading the crack is exposed to. A crack can experience three types of loading, as illustrated in Figure 10. Mode I involves opening of the crack, Mode II involves sliding and Mode III involves tearing.[48]

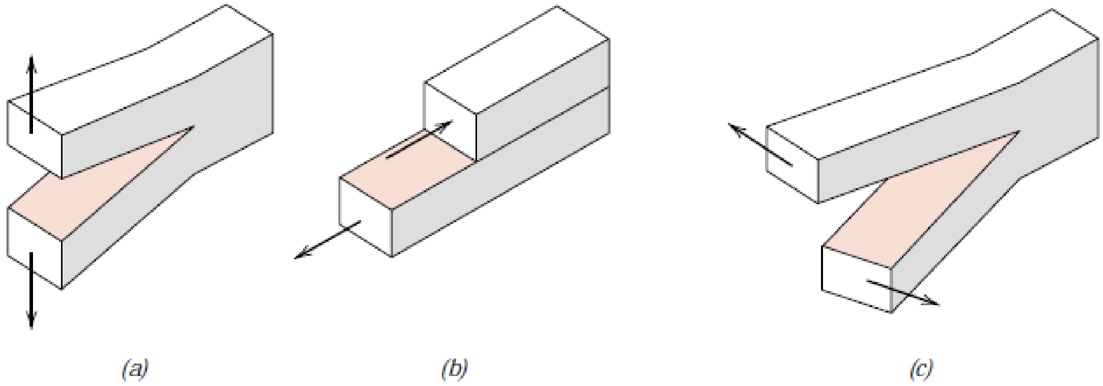

Figure 10 - The three modes of loading which can be applied to a crack: (a) Mode I - opening/tensile, (b) Mode II – sliding, (c) Mode III – tearing.[48]

The stress intensity factor can be made useful by correlating it to external loads and sample geometry. As the sample size decreases, the dimensions of the crack become large relative to the size of the specimen, meaning that the crack-tip conditions are influenced by the sample geometry. To resolve this, a geometric factor f(a_0/W) is introduced. The stress intensity factor for mode I loading is thus given by equation 2.3

$$K_I = \frac{P}{B\sqrt{W}} f\left(\frac{a_0}{W}\right) \tag{2.3}$$

Where P is the applied force (N), B is the specimen thickness (mm), W is the length from the loading point to the end of the specimen and a_0 is the crack length, as illustrated in Figure 11 for a compact tension (CT) specimen. For mode I loading of a CT specimen, the dimensionless geometric factor f(a_0/W) is given by equation 2.4 [41]

$$f\left(\frac{a}{W}\right) = \frac{2+\frac{a_0}{W}}{\left(1-\frac{a_0}{W}\right)^{\frac{3}{2}}}\left[0.886 + 4.64\left(\frac{a_0}{W}\right) - 13.32\left(\frac{a_0}{W}\right)^2 + 14.72\left(\frac{a_0}{W}\right)^3 - 5.60\left(\frac{a_0}{W}\right)^4\right] \tag{2.4}$$

For K_{IC} testing, the size requirement given by equation 2.5, must be fulfilled, in order for the equations given above to be valid.

$$a, B, (W-a) \geq 2.5\left(\frac{K_{IC}}{\sigma_{YS}}\right)^2 \tag{2.5}$$

These requirements ensure that the fracture is K-controlled, i.e. that the plastic zone ahead of the crack tip is sufficiently small. The thickness requirement (B) is selected to ensure plane strain conditions at the crack tip. The requirement for thickness given by equation 2.5 above, is more strict than needed in order to ensure that plain strain is the dominating condition ahead of the crack tip.[39]

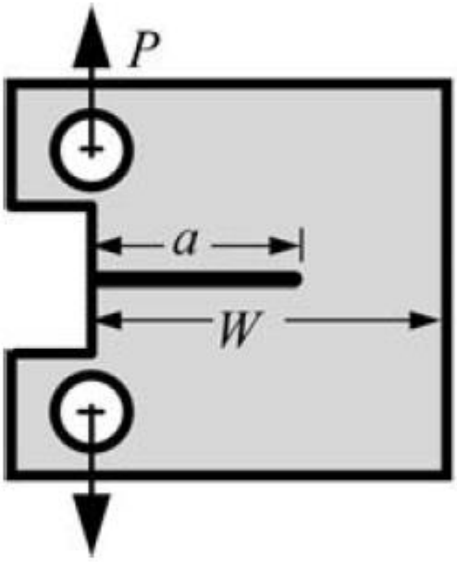

Figure 11 - Compact tension (CT) specimen geometry. P is the applied force (N).[39]

2.4.3. The CTOD Test

For ductile materials, i.e. materials in which plastic deformation is not limited to a small region surrounding the crack tip, LEFM and K_{Ic} cannot be used to characterize the fracture behavior. Here, elastic-plastic fracture mechanics (EPFM) must be applied. The elastic-plastic parameters *J contour integral* and *CTOD* (crack-tip-opening displacement) are therefore applied for materials which undergo plastic deformation.[41] The CTOD parameter is used in this work and is thus described below.

In high toughness materials, plastic deformation will blunt the initially sharp crack, with increased toughness resulting in increased blunting of the crack. This indicates that the crack tip opening displacement (CTOD) can be used as a measure of fracture toughness. Figure 12 illustrates the principle of CTOD, in which the original sharp crack is blunted by plastic deformation. When LEFM is no longer valid, CTOD is deemed a suitable parameter for assessment of fracture toughness.[41]

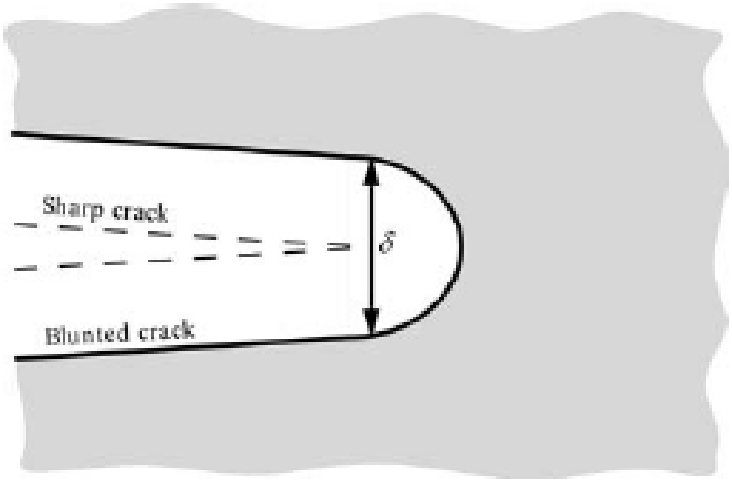

Figure 12 – CTOD definition. An initially sharp crack blunts with plastic deformation, resulting in a finite displacement (δ) at the crack tip.[41]

CTOD testing is typically performed on single-edge-notched bend (SENB) specimens or compact tension (CT) specimens. The samples are fatigue pre-cracked in order to introduce a sharp crack prior to testing, as this is the basis of fracture mechanics and is thus necessary in order to obtain results that represent the true properties of the material. Due to ease of access, the crack-mouth-opening-displacement (CMOD), rather than the CTOD, is measured by clip gages attached to knife edges at the crack mouth. As the crack opens, the beams of the clip gages deflect, resulting in a change in voltage. The correlation between change in voltage and crack mouth displacement is linear, allowing for determination of the CMOD. The CTOD can be found from the CMOD, as will be described shortly.[49]

The CTOD is separated into an elastic and plastic component. The elastic component δ_{el} is related to the elastic K by equation 2.6 for plane strain conditions

$$\delta_{el} = \frac{K^2(1-\nu)^2}{2\sigma_{YS}E} \tag{2.6}$$

Where K is the stress intensity factor, related to the applied force by equation 2.3, ν is the Poisson's ratio, σ_{Ys} is the yield strength and E is the Young's modulus. The plastic component of the CTOD δ_{pl} is given by equation 2.7

$$\delta_{pl} = \frac{r_p(W-a_0)V_p}{r_p(W-a_0)+a_0+z} \tag{2.7}$$

Where r_p is the plastic rotational factor ($r_p = 0.46$ for CT specimens) and V_p is the plastic CMOD. V_p is typically determined graphically. W and a_0 are the geometrical parameters described above. The correlation between the plastic CMOD and CTOD is illustrated for a SENB specimen in Figure 13.[49]

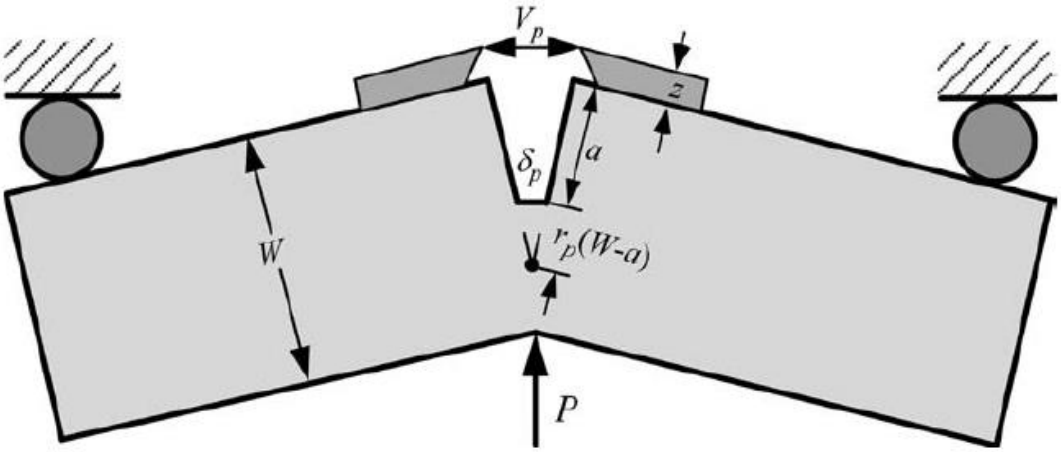

Figure 13 – Plastic displacements in SENB specimen.[49]

2.5. Hydrogen Induced Stress Cracking

The presence of atomic hydrogen may have a deleterious effect on the mechanical properties of metals and alloys. The considerable reduction in toughness and ductility in the presence of atomic hydrogen is known as hydrogen embrittlement (HE). In the oil and gas industry, the term hydrogen induced stress cracking (HISC) is more frequently used.[50] Hydrogen atoms, which are small in size compared to most metallic atoms, diffuse interstitially through the metal lattice, resulting in embrittlement, and potentially failure. Even very low concentrations of hydrogen can result in failure. The majority of hydrogen related cracks are transgranular, but intergranular cracking may also be observed.[51]

In order for HISC to occur, the following parameters must be present simultaneously:

1) A source of hydrogen providing sufficient atomic hydrogen.
2) Sufficient stress to cause sub-critical fracture.
3) A susceptible microstructure.

Generally, the susceptibility to HISC increases with increasing strength.[52] Martensitic stainless steels are deemed the most susceptible, whereas ferritic steels are somewhat less susceptible. Austenitic stainless steels display little susceptibility towards HISC, as will be explained in section 2.5.2.[53]

2.5.1. Mechanisms

Hydrogen may be introduced from an external source, such as cathodic protection (CP) or H_2S. This is called hydrogen-environment-assisted-cracking (HEAC). Hydrogen may also be present as a dissolved species inside the material, either from welding or manufacturing. This is called internal-hydrogen-assisted-cracking (IHAE), and will not be discussed here. For HEAC, hydrogen gas dissociates to its atomic form, and is adsorbed onto the steel surface. The atomic hydrogen will diffuse into the material, and typically concentrate at areas of high hydrostatic stresses, such as the fracture process zone (FPZ) close to the crack tip. At the crack tip, the high stress triaxiality expands the crystal lattice, leading to a local increase in hydrogen solubility, and subsequent embrittlement of the FPZ. This embrittlement in combination with high local stresses, results in microcracking in the FPZ. Crack propagation ensues as the microcracks are linked to the main crack. The process of hydrogen uptake and microcracking then continues the process.[53, 54]

There are several theories trying to explain the mechanisms behind hydrogen induced cracking. The two most agreed upon theories are presented briefly below.

Hydrogen-enhanced decohesion (HEDE): Interstitial hydrogen reduces the cohesive forces between atoms by expanding the crystal lattice, thus facilitating fracture. When these interatomic bonds are weakened, tensile separation of atoms, i.e. decohesion, occurs preferably to slip. The fracture is thought to initiate ahead of the crack tip, in the area with the highest hydrostatic stresses.[53, 55]

Hydrogen-enhanced localized plasticity (HELP): Atomic hydrogen facilitates dislocation motion in certain crystallographic planes at the crack tip, resulting in a localized softened region. The crack will thus grow by microvoid coalescence along these planes, initiating from slip planes at the crack tip. In spite of the localized plasticity at the crack tip, the crack growth appears brittle from a macroscopic point of view. [53, 55]

For the HELP mechanism, experimental observations supporting the theory have been reported. This is discussed in more detail by Olden et al.[55] Regarding HEDE, there is a lack of direct experimental observations, as there is no method for observing what happens at the crack tip on an atomic level. However, high levels of hydrogen have been found at grain boundaries and matrix-particle interfaces. Additionally, quantum mechanical calculations corroborating the theory of hydrogen weakening the atomic bonds resulting in HEDE have been performed.[53]

2.5.2. Hydrogen Diffusion

The crystal structure influences the mobility of hydrogen, in addition to several other parameters, such as temperature, composition, stresses and electrochemical conditions. In steels, hydrogen atoms mainly diffuse between interstitial positions. Hydrogen atoms diffuse more rapidly in BCC structures, than in FCC structures, due to BCC lattice structures being more open. For the exact same reason, the solubility of hydrogen is higher in the more densely packed FCC structures. Martensite, which has a BCC, BCT or HCP lattice structure, has a hydrogen diffusivity and solubility somewhere between austenite and ferrite.[56] Austenitic metals are less susceptible to HISC due to their FCC structure. The brittle fracture associated with HISC can, however, be found in stainless steels under cathodic charging.[57] Regarding clad pipes, the high diffusivity of hydrogen in ferrite and low solubility in austenite can lead to a build-up of hydrogen on the austenitic side of the dissimilar interface, or at the interface region. The result is a reduction in toughness, and potentially failure along the dissimilar interface, or on the austenitic side immediately adjacent to the interface.[58]

Hydrogen may also become trapped in the lattice, thus reducing the amount of diffusible hydrogen, which in turn stalls the movement of hydrogen. Phase boundaries, inclusions, precipitates, grain boundaries, dislocations and vacancies are common trapping sites for hydrogen.[56]

2.5.3. Test Methods and Previous Work

The influence of hydrogen on the mechanical properties of steels is typically assessed by slow strain rate (SSR) tensile testing under hydrogen charging. For hydrogen related SSR tests, strain rates of 1-4 x 10^{-6} s^{-1} is typically applied. [56] In this section, a selection of relevant previous work is presented.

Fenske [59] investigated the dissimilar interface between Fe-Ni butter welds with respect to hydrogen embrittlement on SENB specimens (12x12x200 mm). The specimens were notched using electro-discharge machining (EDM), rather than fatigue pre-cracking, in order to ensure that the notch was centered at the interface. Prior to testing, the samples were pre-charged in artificial seawater under CP (-1100 mV_{SCE}) for a minimum of 48 hours. The samples were subjected to three-point bending at a slow rate in seawater under CP, with the test rate corresponding to a crosshead displacement rate of $5*10^{-6}$ mm/s. Investigations focused mainly on characterizing the fracture morphology of the dissimilar interface, and showed that M_7C_3 carbides are important with regards to HE susceptibility of Fe-Ni butter weldments. Fracture initiates at the interface between the Fe base metal and discontinuous partially mixed zones (PMZs). The M_7C_3 carbides work as hydrogen accumulators, resulting in a low energy fracture path between the PMZs, which in turn results in failure. The fracture morphology was found to alternate between flat (PMZs) and cleavage (carbides).

Dodge [60] also investigated the embrittlement mechanisms of Fe-Ni butter welds. SENB specimens (12.5x12.5x120 mm) were machined from retrieved joints, which had been in subsea service for 9 months. The specimens were notched at the interface by EDM. Prior to testing, the samples were pre-charged in a 3.5 wt% NaCl solution at -1100 mV_{SCE} for one week. Testing was performed using the unloading compliance method with a loading rate of 0.018 mm/h. Pre-charging and testing was performed at various combinations of the temperatures 4 and 80 ˚C. The results showed that hydrogen lowers the fracture toughness. The resistance to HE was found to increase with increasing temperature, independent of pre-charging temperature.

Milititsky et al.[58] performed fracture toughness testing of the dissimilar interface between AISI 863M substrate and IN625 weld metal. SENB specimens (B = 12 mm) were tested in air and under simulated CP (3.5 wt% NaCl,-1100 mV_{SCE}) at 4 ˚C. Testing was performed using the unloading compliance method with a loading rate of 0.018 mm/h. Both EDM notched and fatigue pre-cracked specimens were tested. Prior to CP-testing, the specimens were pre-charged for 48 hours (3.5 wt% NaCl,-1100 mV_{SCE}). The fracture toughness was found to be influenced by the environment, as the specimens tested under CP conditions showed significantly lower fracture toughness than those tested in air. Additionally, the fracture toughness was influenced by notch geometry, especially for CP conditions. The fatigue pre-cracked specimens generally resulted in lower fracture toughness than the EDM notched specimen. In air, the effect of notch geometry was less distinct.

2.6. Scanning Electron Microscopy

A scanning electron microscope (SEM) uses electrons rather than light to form an image. This yields high resolution and good depth of field.[61] In a SEM, an electron beam is emitted, accelerated and focused towards the sample in a vacuum chamber. The area to be investigated is scanned by the electron beam. The focused electron beam interacts with the sample surface, resulting in several different signals, such as secondary electrons (SE), backscattered electrons (BSE) and characteristic x-rays. These signals can be detected and used to provide information about the sample topography, crystallography and chemical composition. SEM samples must be electrically conducting, and should be clean prior to investigations.[62]

Backscattered electrons (BSE) are primary electrons which exit the sample after impact. The fraction of BSE increases with increasing atomic number, giving rise to atomic contrast (Z-contrast), in which heavier elements appear brighter than lighter elements.[62]

Secondary electrons (SE) are generated when an incoming electron impacts and interacts with an electron in the specimen, kicking the bound electron out if its shell. If the energy of the incoming electron is sufficiently high, and the bound electron is close to the specimen surface, the SE may exit the sample and be detected. SE can also be generated from BSE exiting the sample. SE yield information about sample topography.[62]

When performing investigations of fracture surfaces, the depth of field, given by equation 2.8, is an important parameter. The depth of field is defined as the maximum height difference in which the image is in focus.

$$D = \left[\frac{\delta}{M} - d_p\right] * \frac{1}{\alpha} \tag{2.8}$$

D is the depth of field, δ is the resolution of the human eye (0.1 mm), M is the magnification, d_p is the resolution and α is the beam divergence. As this illustrates, a compromise between resolution and depth of field must be made.[62]

2.7. Transmission Electron Microscopy

A transmission electron microscope (TEM) is similar to a SEM in setup, but yields a significantly higher resolution and magnification. The specimens must be sufficiently thin, in order to be permeable for electrons, as that is the basis for all TEM analysis. Higher acceleration voltages allows for thicker specimens to be penetrated by electrons. Thin, electron transparent regions may be obtained from electropolishing, ion thinning, or a combination of the two.[63]

The TEM has a column-like setup, much like the SEM, as illustrated in Figure 14. The electron gun is located at the top, and emits electrons by either thermionic, Schottky or field emission. The electrons are accelerated towards the sample by the acceleration voltage. The condenser system focuses the electron beam onto the specimen, and determines how much of the specimen is illuminated. The objective lens forms the first intermediate image of the specimen, which is located directly above the objective lens. The image is then magnified by the intermediate lenses, and finally projected onto a fluorescent screen by the projector lens.[63, 64]

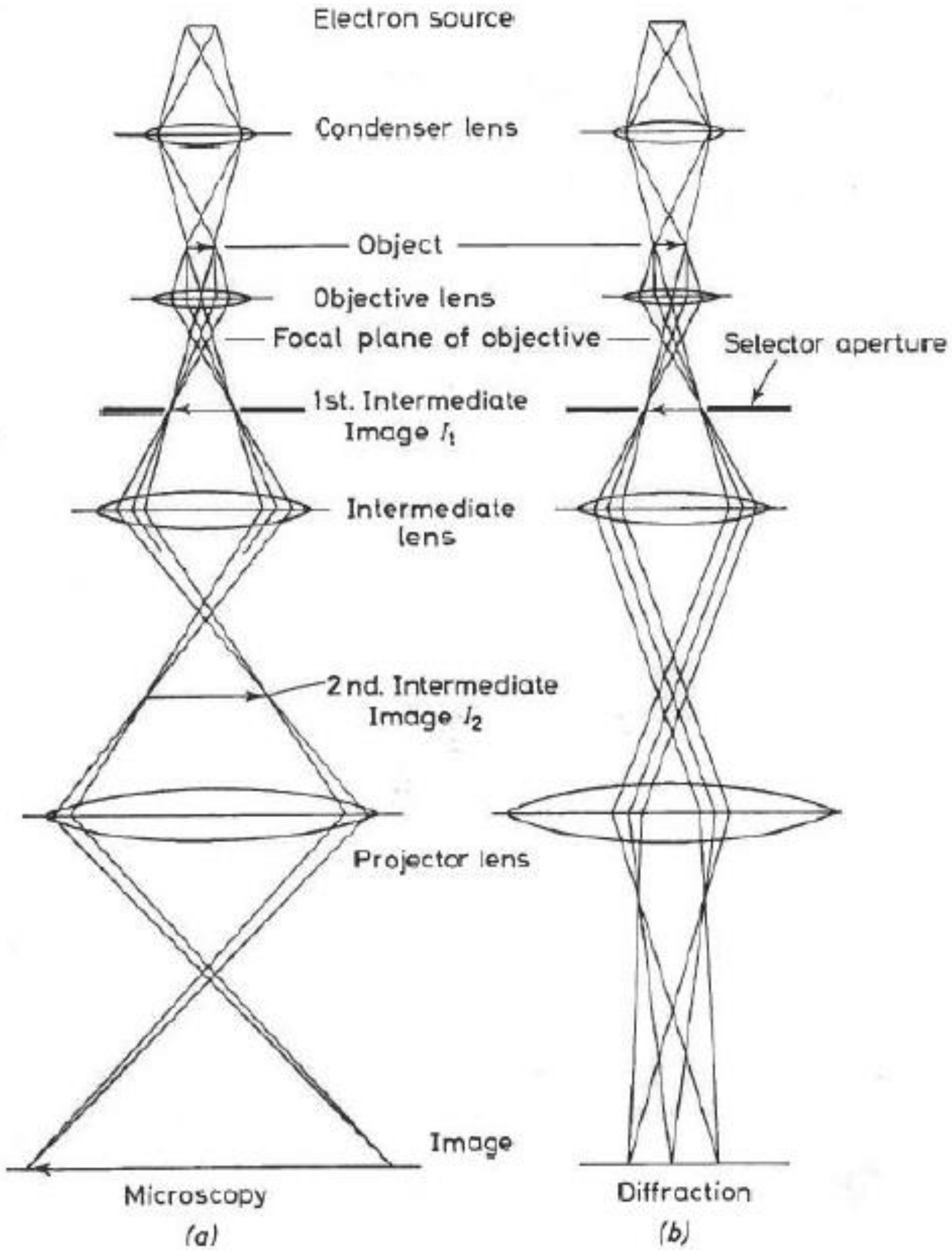

Figure 14 – Electron beam pathway through the TEM in : (a) microscopy mode and (b) diffraction mode.[63]

2.7.1. Diffraction and Imaging

The incoming electrons are scattered elastically and inelastically as they interact with the specimen. Only the elastic scattering is treated here, as the inelastic scattering only generates background noise in the diffraction images. Each atom in the crystal lattice will scatter the incoming electron beam in all directions. Due to the highly systematic nature of the crystal lattice, the scattered electrons will interfere destructively and constructively in specific directions. According to Bragg's law, which is a simplification of the scattering process, constructive interference will occur in a direction where n is an integer, see equation 2.9.

$$2dsin\theta = n\lambda \tag{2.9}$$

where d is the interplanar spacing, i.e. the distance between two neighboring crystal planes which have the same Miller indices, θ is the incident angle, λ is the wavelength and n is the order of reflection.[63, 64]

The TEM can operate in several different modes. Microscopy mode and diffraction mode, schematically illustrated in Figure 14, are the most common and will thus be explained here. In diffraction mode, a magnified image of the diffraction pattern is depicted onto the fluorescent screen. As illustrated in Figure 15 a), the diffraction which satisfies Bragg's law yield parallel beams, which are focused in the rear focal plane by the objective lens, resulting in a diffraction pattern. Each direction of constructive interference results in a spot in the diffraction pattern. In microscopy mode, the strength of the intermediate lens is changed, so that all of the radiation leaving the same point in the specimen is focused to a point in the image plane of the objective lens, as seen in Figure 15 b). The image is then magnified and projected onto the fluorescent screen.[63]

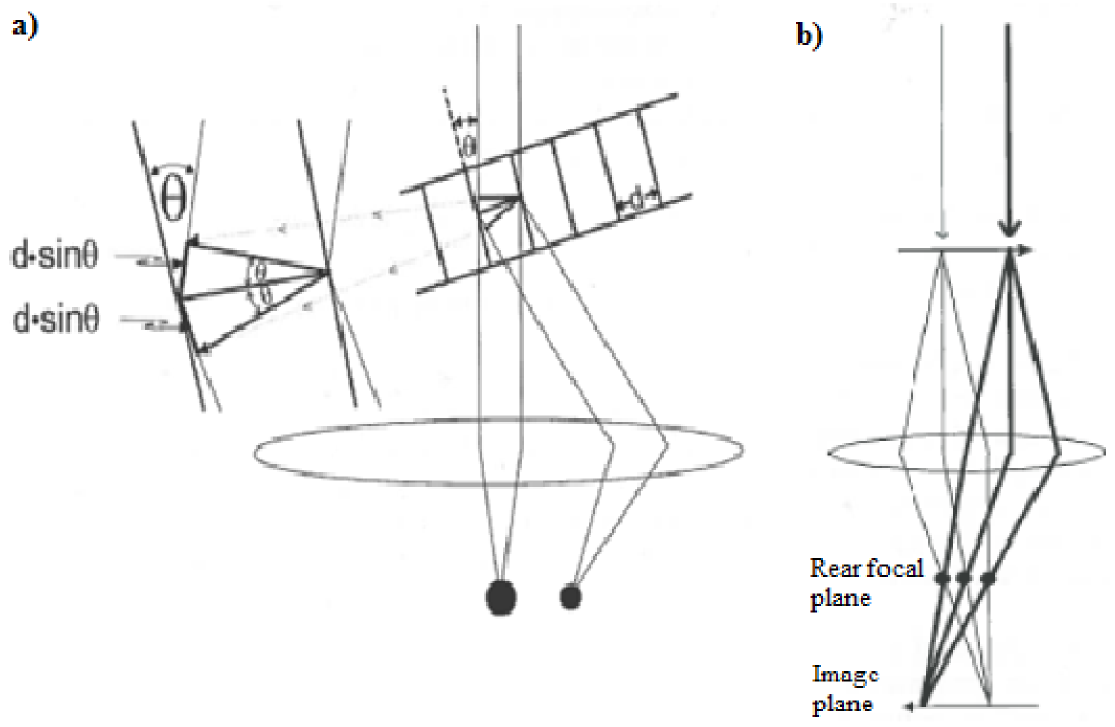

Figure 15 – a) Illustration of Bragg's law. b) Diffraction and imaging in the rear focal plane and image plane, respectively. [63]

The electron beam is scattered at a very small angle in the electron microscope (< 1°), so that only planes that are almost parallel to the incoming beam will give Bragg reflection of lower order, i.e. constructive interference. All other sets of planes will give destructive interference. Theoretically, Bragg's law can only be fulfilled for one order of reflection at a time, yet reflections from several orders of n from the same set of lattice planes may be observed in the diffraction pattern. This is attributed to the following:

- The incoming electron beams are not entirely parallel.
- The sample will always be slightly bent in the electron transparent areas.
- The sample is quite thin, which could give rise to deviations Bragg's law.[63]

As this explains, a set of lattice planes will yield several reflexes, present in the diffraction pattern as a row of reflexes. If several sets of planes are approximately parallel to the incoming electron beam, the diffraction pattern will consist of several reflexes, as seen for an FCC crystal in Figure 16. The central spot represents the electrons which have passed directly through the sample without scattering and is indexed (000). In diffraction pattern images this spot is typically brighter than the surrounding reflexes.[63]

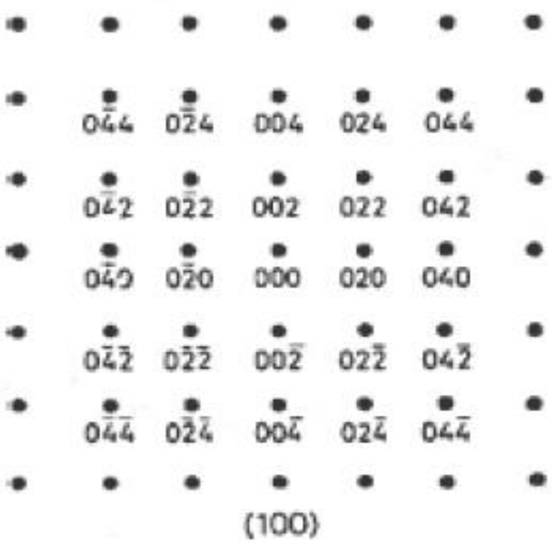

Figure 16 - Indexed diffraction pattern from FCC crystal. Zone axis: (100).[63]

The zone axis corresponds to the direction of the incoming electron beam [61], i.e. for the diffraction pattern in Figure 16, the incoming electron beam is parallel to the (100) planes. This means that it is the (100) planes giving rise to this particular diffraction pattern. The number under each diffraction spot denotes the Miller indices (h, k, l) for the diffracting plane.

The interplanar spacing in the specimen is related to the spacing between the reflexes in the diffraction pattern by equation 2.10

$$d_{hkl} = \frac{L\lambda}{R_{hkl}} \tag{2.10}$$

where R is the measured distance from the direct beam to the reflection (g), d is the interplanar spacing, λ is the wavelength of the incoming electrons and L is the distance between the specimen and the fluorescent screen (camera length), as illustrated in Figure 17. As the diffraction pattern is in the reciprocal space, the distance R is given in reciprocal length (nm^{-1}). This means that the large distances in the diffraction pattern will represent small distances in the specimen, and vice versa.[63]

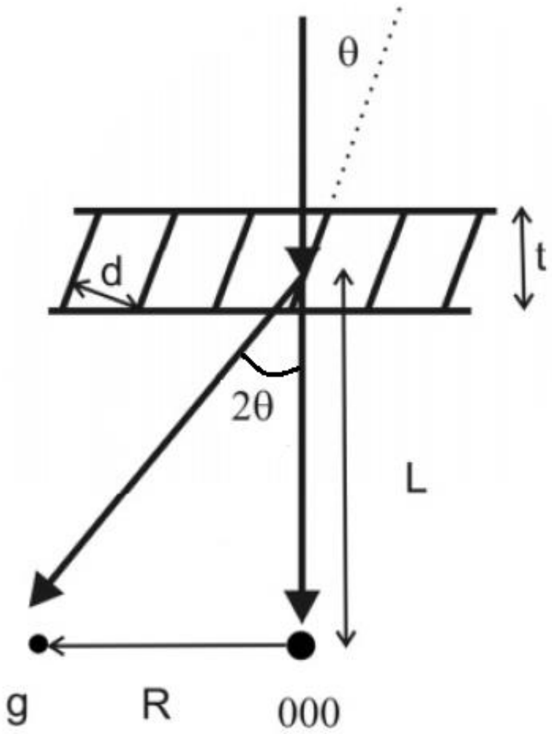

Figure 17 – Sketch showing the correlation between interplanar spacing (d), cameralength (L), the distance between the direct beam and reflection g (R) and the Bragg angle (θ) in a specimen with a thickness t. Adapted from [65].

The Miller indices can be determined from the interplanar spacing using equation 2.11 for cubic symmetries.

$$d_{hkl} = \frac{a}{\sqrt{h^2+k^2+l^2}} \tag{2.11}$$

where d_{hkl} is the interplanar spacing, a is the lattice parameter and h,k and l are the Miller indices of the plane. As this equation only applies to cubic symmetries, and the lattice parameter varies depending on the material system, it is beneficial to have an overview of the crystal structure and composition of the constituents being investigated. Additionally, certain crystal structures have allowed and forbidden reflexes, as seen for FCC and BCC structures in Table 2. For instance, the diffraction pattern from an FCC structure will not contain any reflexes from (100) and (110) planes, as these are forbidden reflexes.[63]

Table 2 - Allowed and forbidden reflexes for FCC and BCC crystal structures.[63]

	Allowed reflexes	**Forbidden reflexes**
FCC	hkl: all odd or even numbers	hkl: mix of odd and even numbers
BCC	hkl: sum is an even number	hkl: sum is an odd number

In order to obtain a good diffraction pattern, it is beneficial to reduce the illuminated area of the specimen, as the specimen often will be bent, and the high intensity of the direct beam may damage the fluorescent screen. This is done by inserting an aperture into the image plane of the objective lens, and is called selected-area diffraction (SAD).[61]

2.7.2. Microscopy

2.7.2.1. Bright Field and Dark Field Imaging

As mentioned in section 2.7.1, all radiation leaving the same point in the specimen is focused to a point in the image plane of the objective lens. The image is then magnified and projected onto the fluorescent screen. In order to improve the contrast of the image, an aperture is inserted into the focal plane of the objective lens. This objective aperture provides bright field and dark field imaging.

In bright field imaging, only the direct beam is allowed to pass through the objective aperture, as illustrated in Figure 18. Scattered electrons do not pass through the aperture, resulting in lower image intensity in the areas where Bragg's law is fulfilled. As the sample always will be somewhat bent, the majority of the area will not satisfy Bragg's law, resulting in a high intensity background. In dark field imaging, the objective aperture only allows the Bragg scattered electrons to pass through, whereas the direct beam and other scattered electrons are stopped, as illustrated in Figure 18. The areas giving rise to Bragg scattering in the sample will thus be observed as bright areas in a dark background on the image.[63]

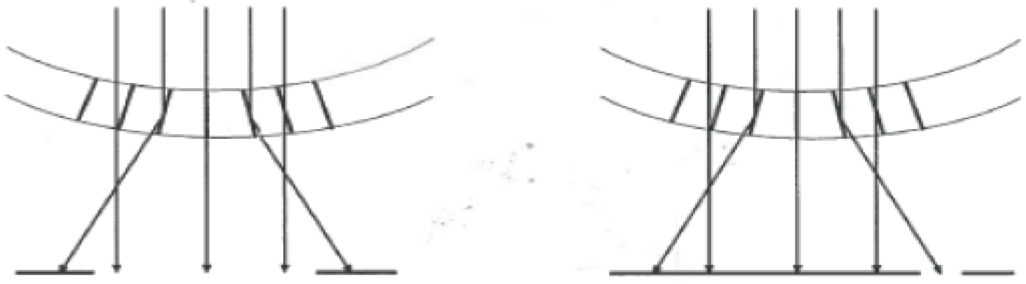

Figure 18 - Left: Bright field imaging. Right: Dark field imaging.[63]

2.7.2.2. Contrast from Particles

If the sample contains incoherent particles, the difference in crystal structure and orientation between the particle and matrix, will give rise to a contrast, facilitating the distinction between the two phases. For coherent particles, Bragg's law will be simultaneously fulfilled for matrix and particle, so that no distinction can be made. Even though the particles are coherent, there will be a small difference in interplanar spacing between the particle and matrix. This results in a stress field at the matrix-particle interface. By tilting the specimen so that only the stress fields fulfill Bragg's law, the coherent particles can be observed.[63]

2.7.3. Other Modes of Operation

The TEM can also be used in scanning mode, denoted scanning transmission electron microscopy (STEM). This combines the principle of TEM and SEM, in which the electron beam scan across the sample in a raster-like manner. In STEM mode, the transmitted electrons are selected by detectors, rather than apertures.[66] The detectors summarize the intensity of the transmitted electrons with respect to probe position to create an image with high spatial resolution. SE detectors and energy-dispersive spectrometers can also be utilized in STEM mode, but the transmitted electrons offer the highest spatial resolution.[67]

Energy-dispersive X-ray analysis can be utilized for qualitative analysis, and can be used in SEM, TEM and STEM. When a bound electron is excited from the sample by an incoming electron, resulting in a hole, which in turn is filled by a higher energy electron, energy in the form of X-rays is released. The energy of the X-rays is characteristic of atomic number, allowing for identification of elements. An energy dispersive spectrometer measures the X-rays emitted from the specimen, with the energy of x-rays producing a pulse, and the number of pulses determines the intensity of the peak.[67]

2.7.4. Final Thinning Techniques

In order for TEM specimens to be electron transparent, the sample must be sufficiently thin. Electropolishing or ion thinning is commonly used as a final thinning step after water grinding and polishing. Both of these techniques require that that the specimen has a thickness below 0.1 mm, and are punched in the form of 3 mm discs.

Electropolishing can only be performed on electrically conducting samples. The sample is set up as the anode inside a closed system. There is a cathode on each side of the specimen. The appropriate electrolyte, depending on material, is constantly pumped through the system. The sample is polished by anodic dissolution, which is obtained by adjusting the voltage of the system. The process is stopped when a hole is obtained. Electropolishing is a fairly quick thinning method, but offers little in terms of selecting the accurate location of the hole.[63]

Ion thinning can be used for thinning of both electrically conducting and non-conducting materials. The process is quite slow, so that the sample should be as thin as possible before starting the thinning. This can be obtained by grinding the sample disc with a dimpler. Ion thinning utilizes high energy ions in order to remove material. The sample is rotated and bombarded with an ionized gas, both from above and below. The high energy ions sputter away atoms in the specimen surface, thus thinning the sample one atomic layer at a time. Ion thinning provides higher accuracy with regards to investigations of interfaces, as both the sample and ion beams can be adjusted.[63]

3. Previous Work

This master's thesis is a continuation of a project thesis written in the fall of 2014. The project thesis was written at NTNU in collaboration with SINTEF, and was also a part of the SINTEF ROP project.[68]

The main objective of the project thesis was to characterize the metallurgical reactions in welded clad X60/X65 pipelines, as the dissimilar nature of clad pipes can result in complex microstructures when exposed to elevated temperatures. The project entailed a literature study on the aspects of dissimilar welding and exposure of bi-metallic components to elevated temperatures, and investigations of welded clad pipes. Pipes with and without a Ni-interlayer between the clad and base metal (BM) was investigated. Investigations included microstructure characterization of the clad, BM and WM, analysis of the clad-base metal interface with respect to compositional gradients and hardness profiles, and mapping of chemical gradients in the root and hotpass of the weld.

The main results of the project thesis, i.e. the ones deemed relevant for this master's thesis, is presented in the following chapters. Sample 1 and sample 2 showed similar results, so that only the results of sample 1 is included here. The theoretical aspects of the literature study are not included here, but rather incorporated into Chapter 2, in order to give a more unified theoretical background.

3.1. Microstructure Characterization

The BM, clad and heat affected zone (HAZ) microstructures were investigated in light optical microscope. The BM HAZ appeared to consist of mainly bainite, in addition to some ferrite, for all three samples. The samples without a Ni-interlayer both contained cracks in the austenitic clad, close to the triple point, as seen for sample 1 in Figure 19. The cracks appeared to propagate along austenite grain boundaries. For the sample with the Ni-interlayer, no cracking was observed, see Figure 21. Etching of the clad, revealed more pronounced grain boundaries in the clad for the samples without the Ni-interlayer, as seen by comparing Figure 20 and Figure 21. The grain boundaries were pronounced both close to the triple point and further away, as seen in Figure 20, and were observed approximately 200-250 µm into the clad. A brownish tinted band was also observed in the samples without a Ni-interlayer, along the length of the clad-BM interface.

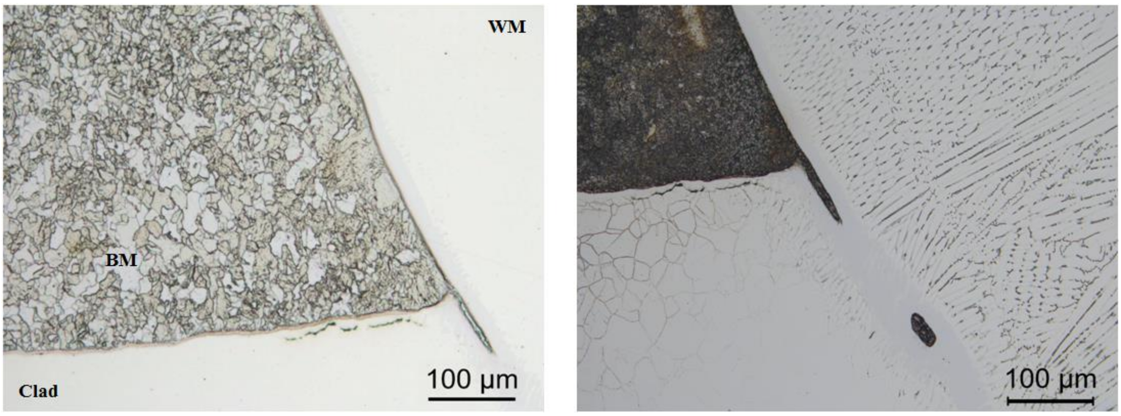

Figure 19 - Sample 1. Left: BM microstructure. Right: BM and clad microstructure. Etched in oxalic acid.

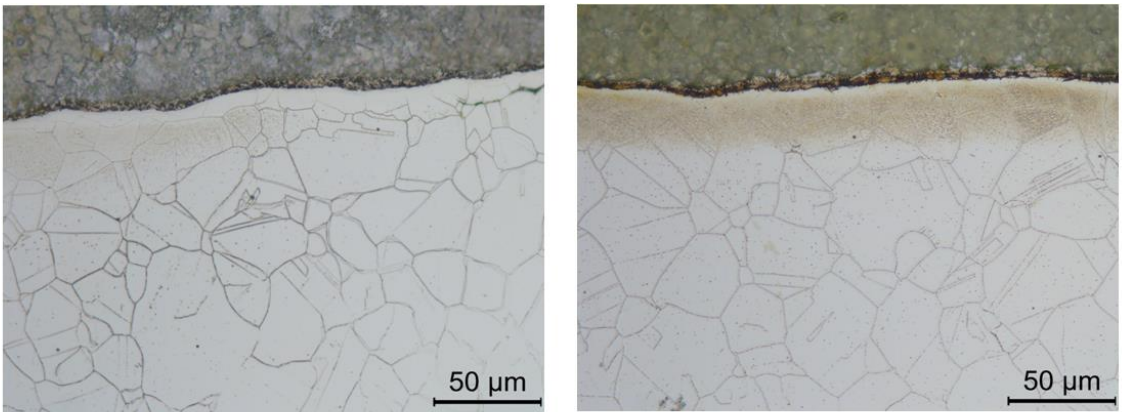

Figure 20 - Sample 2. Left: Clad microstructure at end of crack. Right: Clad microstructure 8 mm from triple point.

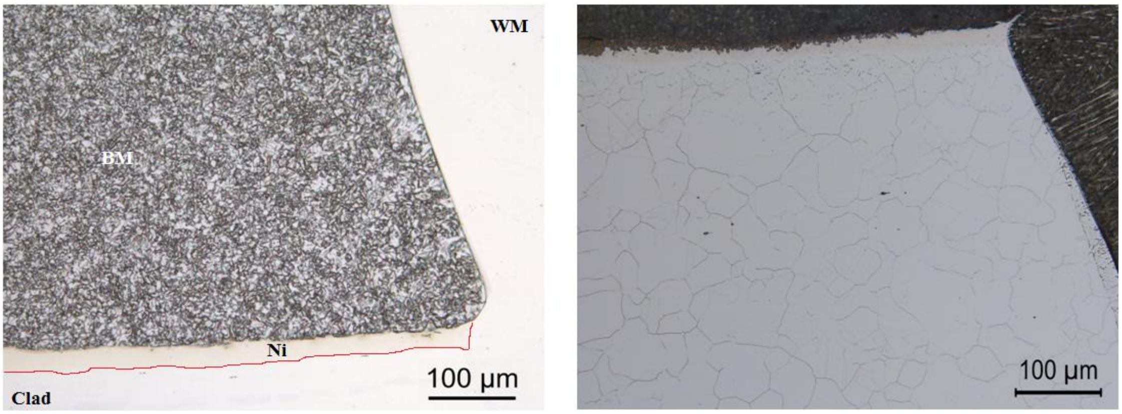

Figure 21 - Sample 3. Left: BM microstructure. Ni-interlayer outlined in red. Right: Clad microstructure. Etched in oxalic acid.

Migration of carbon during exposure to elevated temperatures, from the carbon rich BM to the clad, may result in a softer, carbon depleted zone in the BM, and a hard, carbon enriched region in the clad.[18] In the carbon enriched region, Cr-carbides may precipitate at austenite grain boundaries, rendering the clad susceptible to intergranular cracking close to the dissimilar interface.

3.2. Electron Microprobe Analysis

Carbon line scans across the clad-BM interface using electron microprobe analysis (EMPA) revealed a carbon accumulation on the clad side of the interface for the samples without the Ni-interlayer, see Figure 22. For the sample with the Ni-interlayer, however, there was no apparent carbon accumulation, see Figure 23. This indicates that the Ni-interlayer works to provide much more sluggish diffusion of carbon into the clad. The carbon accumulation was present both close to the triple point and further away, indicating that the majority of carbon diffusion occurs during the production process. However, the carbon appears to be more distributed in the scans close to the triple point and thus the weld metal (line 1 and 2), compared to the reference scan further away (line 3), indicating that some carbon diffusion also occurs during welding.

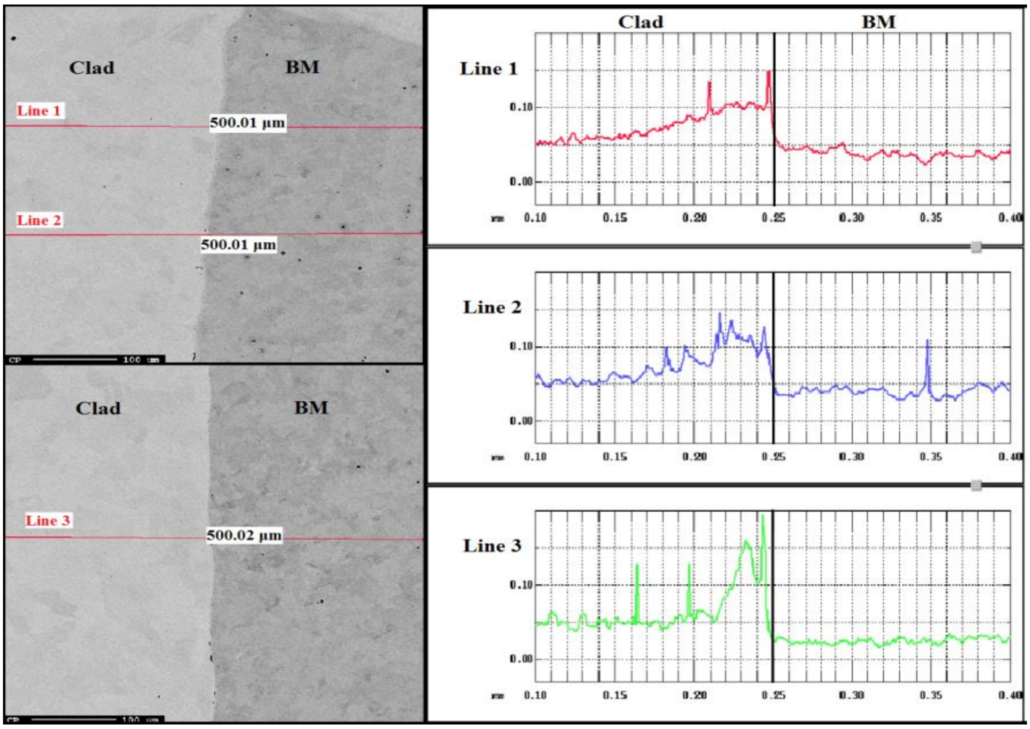

Figure 22 - Sample 1: Variation of carbon (wt%) across clad-BM interface over a distance of 500 µm. Line 3 is approximately 3700 µm away from the triple point (seen in the upper left image).

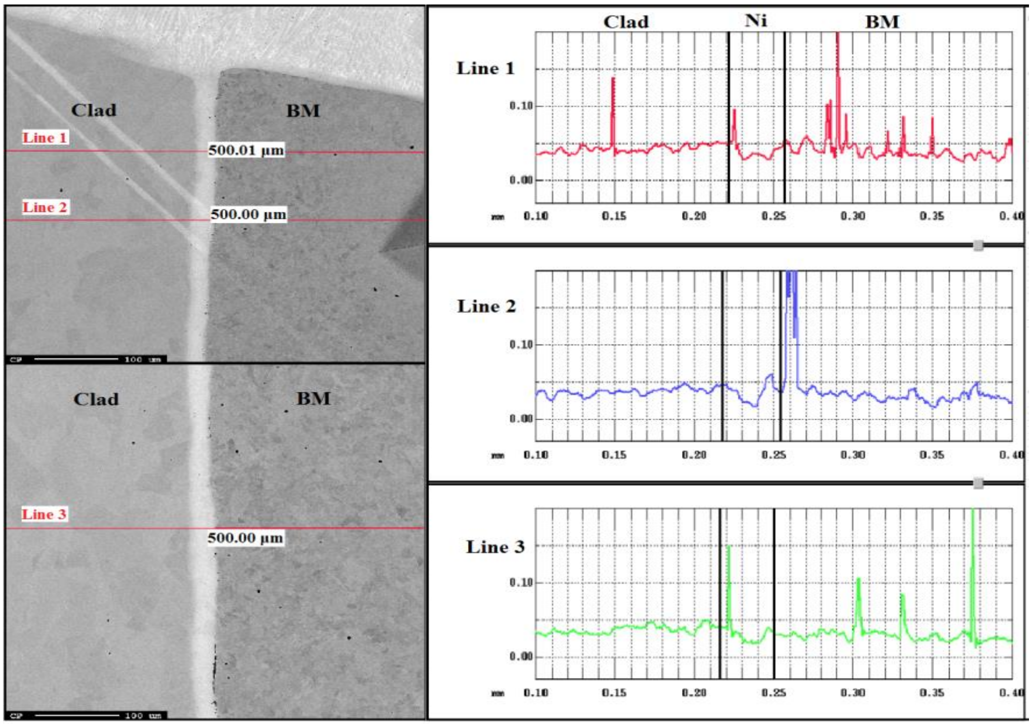

Figure 23 - Sample 3: Variation of carbon (wt%) across clad-BM interface over a distance of 500 µm. Line 3 is approximately 3600 µm away from the triple point (seen in the upper left image). The Ni-interlayer is indicated by the black lines.

EMPA element maps were also obtained. No grain boundary precipitates were observed in the clad, as can be seen for the sample without the Ni-interlayer in Figure 24. Additionally, element line scans and element maps of the BM and clad were also obtained, however, these did not show anything significant, and are thus not included here.

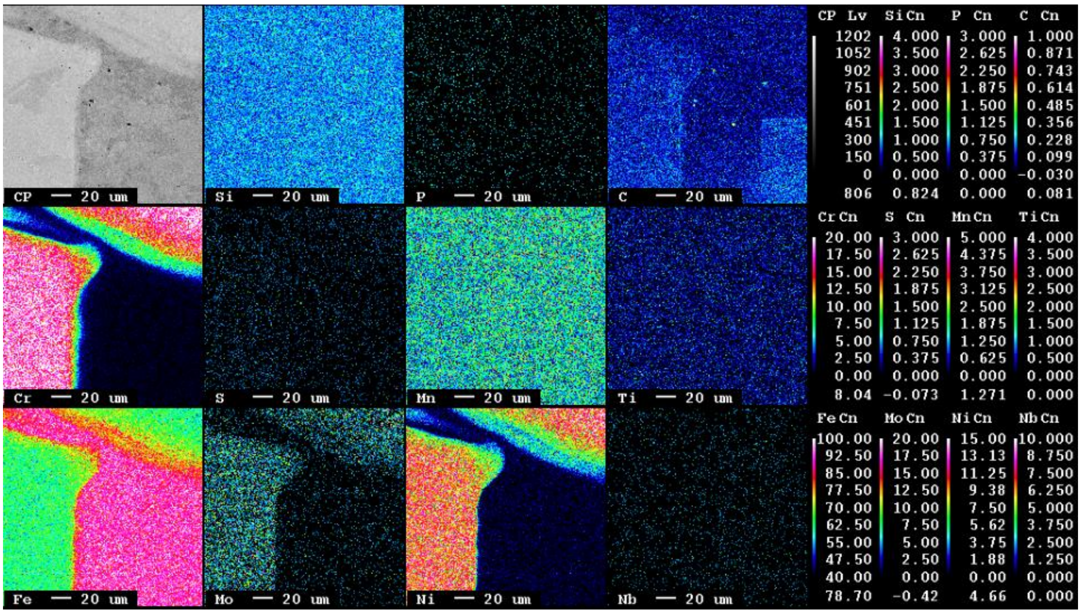

Figure 24 - Sample 1: Element map of triple point.

3.3. Microhardness

Microhardness measurements showed that the average hardness (HV 0.025) in the clad (approximately 5 µm into the clad) was significantly higher in the samples without a Ni-interlayer, see Table 3. Microhardness values of 392 HV and 362 HV were reported for sample 1 and 2, respectively, whereas sample 3 (Ni-interlayer) showed and average clad hardness of 204 HV.

Table 3 - Average hardness in clad (HV0.025), approximately 350-800 µm from triple point.

Sample	Average clad HV0.025	Distance from interface (µm)
1 (WPT-DJ)	392	5 µm into clad
2 (WP-24)	362	5 µm into clad
3 (1W kl.9)	204	30* µm into clad

*Corresponds to approximately 5 µm into the clad, as the interface referred to is the BM-Ni interface.

Hardness profiles across the clad-BM interface revealed a peak in hardness in the clad immediately adjacent to the interface, and a slight dip in hardness on the BM side, for the samples without a Ni-interlayer, see Figure 25. For the sample with the Ni-interlayer, however, no hardness peak was observed, only a slight dip in hardness on the BM side of the interface, see Figure 26.

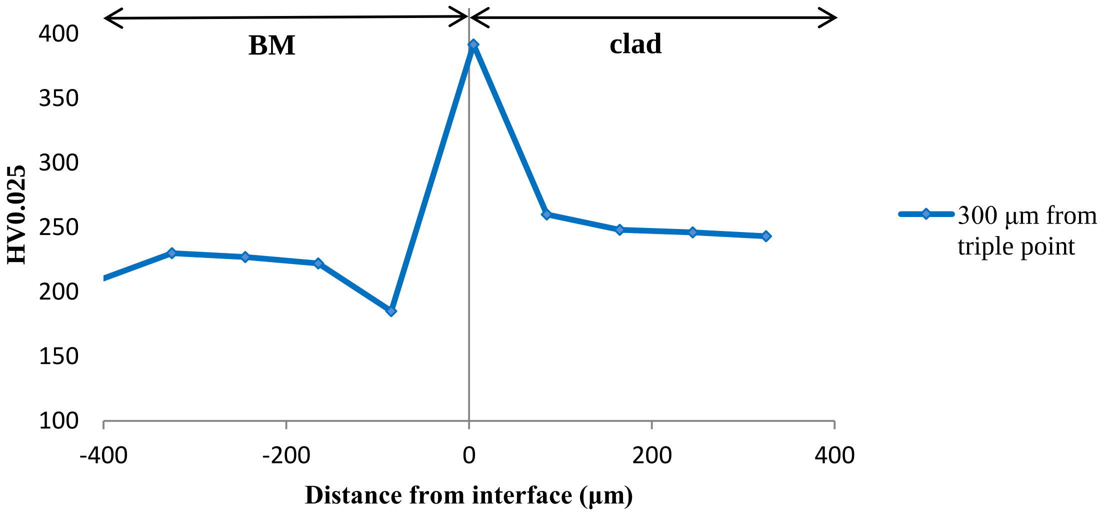

Figure 25 - Sample 1: Hardness profile across BM-clad interface. The dashed line shows the profile based on the average clad hardness value from Table 3.

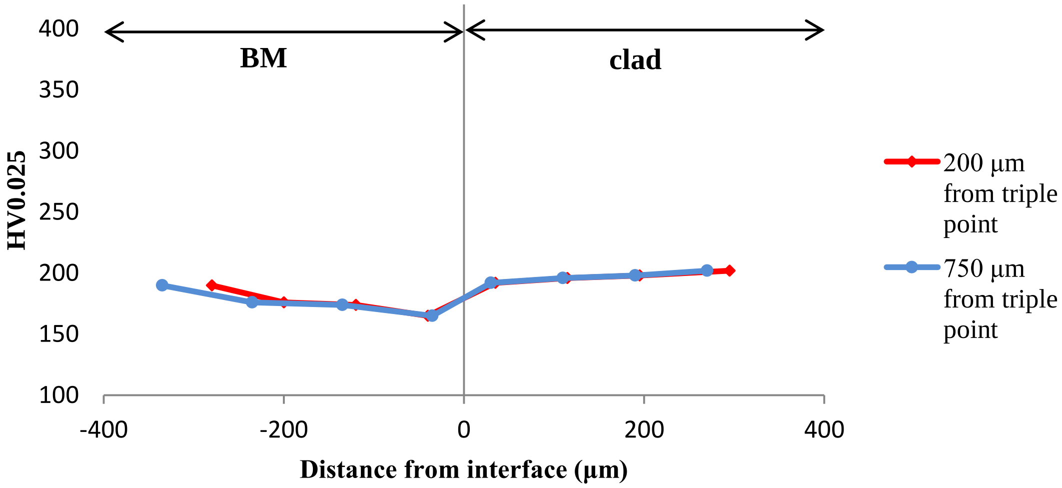

Figure 26 - Sample 3: Hardness profile across BM-clad interface.

3.4. Conclusions

In the absence of a Ni-interlayer, carbon will diffuse from the BM to the clad, mainly during production, but also to a smaller extent during welding. The result of carbon diffusion is a carbon accumulation on the clad side, which might facilitate the formation of grain boundary precipitates. The carbon enriched zone also showed high local hardness values, which could be attributed to carbide precipitation. The cracking in the clad is attributed to the formation of a hard microstructure, with potential grain boundary precipitates determining the crack path. The diffusion of allying elements could possibly facilitate martensite at the interface, which will result in residual stresses near the interface, which in turn could facilitate cracking. The Ni-interlayer complicates carbon diffusion and carbon accumulation in the clad, and thus prevents the formation of hard, crack susceptible zones. Very little grain boundary precipitates were observed for the sample with the Ni-interlayer, most likely due to lack of excessive amounts of carbon.

4. Experimental

4.1. Specimens

In the work preceding this thesis [68], discussed in section 3, three different samples were investigated; sample 1 (no Ni-interlayer), sample 2 (no Ni-interlayer) and sample 3 (Ni-interlayer). Sample 1 and 2 were from the same supplier and only differed in weld metal. As neither the fusion zone nor the heat affected zone is investigated in this thesis, sample 1 and 2 are essentially the same, and is denoted as sample B in this work. The sample with the Ni-interlayer is denoted sample A.

Two different samples, sample A and sample B, were investigated in this work. The material combination is as listed below, and the approximate chemical composition is given in Table 4.

- **Sample A:** 316L clad, X65 BM, Ni interlayer between clad and BM
- **Sample B:** 316L clad, X60 BM

Table 4 - Chemical composition according to material specifications.

Element	**wt %**		
	316L	**X60**	**X65**
C	0.035	0.16	0.16
Cr	16.0-18.0	≤ 0.50	≤ 0.50
Ni	10.0-14.0	≤ 0.50	≤ 0.50
Mo	2.00-3.00	≤ 0.50	≤ 0.50
Si	1.00	0.45	0.45
Mn	2.00	1.65	1.65
P	0.045	0.020	0.020
S	0.030	0.010	0.010
V	-	0.08	0.09
Nb	-	0.05	0.05
Ti	-	0.04	0.06
Other		$V + Nb + Ti \leq 0.15$ $Cu \leq 0.50$	$V + Nb + Ti \leq 0.15$ $Cu \leq 0.50$
Ref.	[69]	[7]	[7]

The samples were extracted from the pipeline by the supplier, as illustrated in Figure 27.

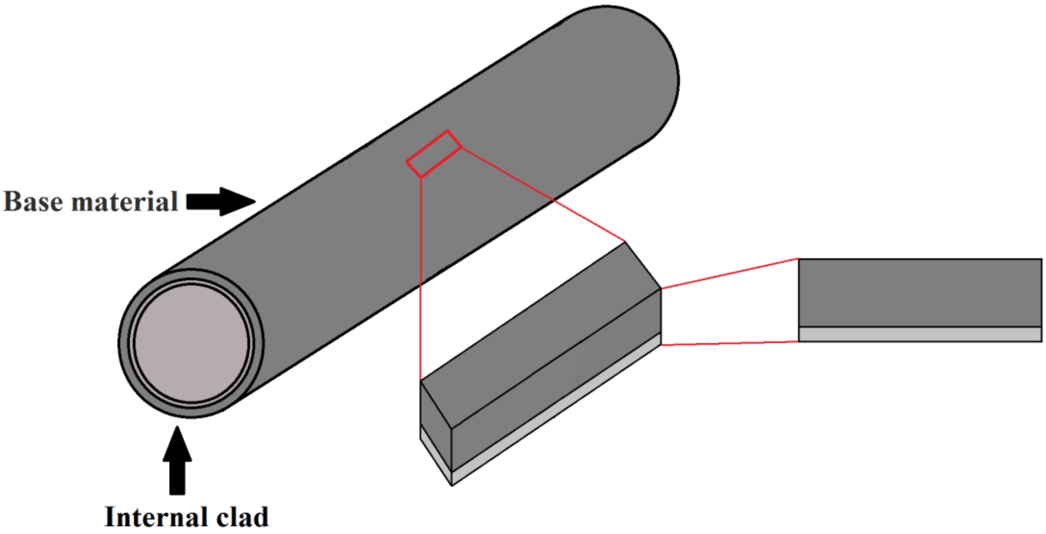

Figure 27 - Overview of sample and area of investigation with regards to pipeline.

The pipes, which are delivered by different suppliers, are both Quenched and Tempered (QT), and thus subsequently heat treated post rolling. Only information regarding the heat treatment of sample B has been obtained, as seen in Table 5.

Table 5 - Heat treatment for sample A and B. NA = not available.

	Sample A (Ni-interlayer)	**Sample B (no Ni-interlayer)**
Quenching	950-980 ˚C, 0 hr. 55 min Water cooled	NA
Tempering	560-590 ˚C, 1 hr. 25 min Air cooled	NA

Due to sample availability and time limitations, the TEM specimens were extracted from the welded samples investigated in previous work. In previous work, the areas close to the **triple point**, i.e. the area where the clad, BM and WM meet, have been the main focus of examination. In this work, investigations have primarily focused on the clad and BM interface region. For TEM specimens, the interface region investigated is located some distance (1.2-2.2 mm) from the triple point. This location is selected in order to prevent the cracks in the clad close to the triple point from complicating the sample preparation process, as the TEM specimens are quite fragile. Additionally, the brown band at the interface and potential grain boundary precipitates, have previously been observed [68] both close to the triple point and further away, in both welded and un-welded specimens. Based on this, the selected areas should be appropriate for characterization of the clad-BM interface and potential grain boundary precipitates.

For fracture toughness testing, miniature compact tension (CT) specimens were machined from pipes in the unwelded condition, as the main objective was to investigate the fracture mechanical properties of the interface region.

4.2. SEM Sample Preparation and Investigation

The macro specimens were wet ground with SiC grinding paper (80, 120, 320, 500, 800, 1200, 2400), followed by diamond polishing using MD Mol (3 µm) and MD Nap (1 µm) cloths with the corresponding diamond suspension (3 µm and 1 µm respectively). Between grinding and polishing, and between the polishing steps, the specimens were washed with soap and water, rinsed in ethyl alcohol and dried rapidly with a blow dryer. The samples were then etched in 2% Nital for approximately 25 seconds to reveal the dissimilar interface microstructure. Prior to SEM investigations, the specimens were rinsed in acetone in an ultrasonic bath for 5 minutes. The samples were removed from the bath, rinsed in acetone and dried using a blow dryer.

SEM investigations were performed using Zeiss SUPRA 55VP LVFESEM (low-vacuum field emission SEM). For investigations of the dissimilar interface, images were obtained in secondary electron (SE) mode, using an aperture of 120 µm, 15 kV acceleration voltage, approximately 10 mm working distance and in high current mode.

4.3. TEM Sample Preparation and Investigation

Only the specimen without the Ni-interlayer, sample B, was prepared for TEM investigations. The carbon migration and subsequent carbide precipitation, in addition to a hardened zone in the clad observed in previous work[68], was the main objectives for the investigations.

A part of the sample containing the clad-BM interface was sectioned out using Struers Discotom-2. Thin slices, i.e. as thin as possible (approximately 0.5-0.8 mm), were then cut from this section, using Struers Accutom-50. The cutting speed was adjusted according to the sample size, ranging from 0.05-0.115 mm/s. The clad-BM interface was located at the center of the specimen, as seen in Figure 28.

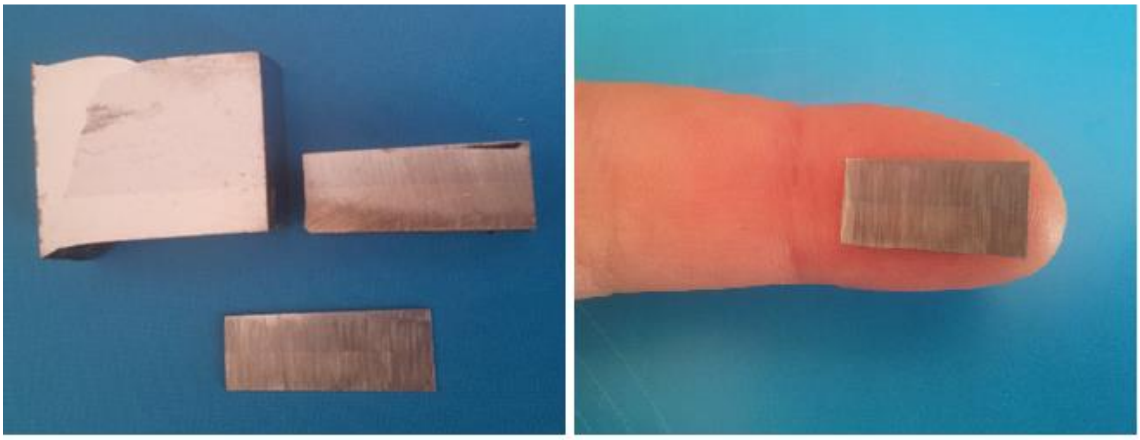

Figure 28 - Sample 2: Left: Macro specimen and sectioned TEM specimens. Right: TEM specimen placed on finger for grinding (tape is missing).

The slices, measuring approximately 8 x 13 mm in size, were wet ground with SiC grinding paper (120, 320, 500, 800, 1200, 2400) to reach the desired thickness of 100 μm or lower. The first side was ground by attaching the sample to a double-sided taped index finger, as illustrated in Figure 28. The second side was ground by attaching the specimen to a plexiglass block by using double sided tape. When the edges of the samples could no longer be felt upon sliding a finger across the plexiglass, the sample was deemed sufficiently thin, and grinding was stopped. The plexiglass was placed in liquid nitrogen for a couple of minutes to remove the sample without introducing significant strains. The sample was rinsed in acetone and dried on filter paper. Then, 3 mm discs were punched from the slice, aiming to center the clad-BM interface.

For the final thinning and electron transparency, three different approaches were made:

- Ion thinning
- Dimpling and ion thinning
- Electropolishing and ion thinning.

Investigating dissimilar interfaces in TEM can be quite challenging.[70] Firstly, different materials tend to have different thinning rates. Additionally, it can be challenging centering the interface when punching the disks and during dimpling. Fenske [59] performed TEM investigations on samples containing a forging steel (F22) and Ni-alloy (IN625), and found dimpling and ion thinning to give the highest quality TEM specimens. However, due to difficulty obtaining electron transparency at the specific region of interest, a focused ion beam (FIB) technique was used to prepare TEM specimens of the dissimilar interface. For this work, however, the allotted time and resources deemed FIB ineligible. The different sample preparation methods applied here is described in detail below.

Ion thinning was performed using Gatan PIPS (precision ion polishing system). Two ion beams were used, one below and above the sample, with a 4 degree incline. The sample rotated 360 degrees at a rate of 1 rpm. The electron gun energy was the only variable parameter, varying between 4.5-1.5 keV. The lower beam energies were utilized in the final thinning stages.

Dimpling was done using Agar Dimpler Model 2000 from E.A. Fischione. The first stages of the dimpling were performed using 6 μm diamond paste and distilled water as lubricant, whereas 1 μm diamond paste and distilled water was used for the final dimpling stage.

Electropolishing was done using Struers TenuPol-5. Struers method A8 for stainless steel was selected. The voltage was set to 50 V, the temperature was ambient (20 °C), and the current varied between 26-28 mA and 32-34 mA, depending on whether the clad or BM was being dissolved. The etchant consisted of 50 ml perchloric acid, 950 ml ethylene glycol and monobutyl ether. Electropolishing of one 3 mm disk took between 1-4.5

minutes, depending on specimen thickness. Immediately after the process was finished, the specimen and container was removed from the electrolyte and rinsed in methanol. The specimen was then removed from the container, and again rinsed in methanol, followed by rinsing in ethanol, and left to air dry on filter paper. 9 samples were electropolished, but only a 3 were eligible for further work, i.e. had holes in the clad close to the interface.

An overview of the TEM specimens' surface after electropolishing and dimpling and ion thinning is presented in Figure 29.

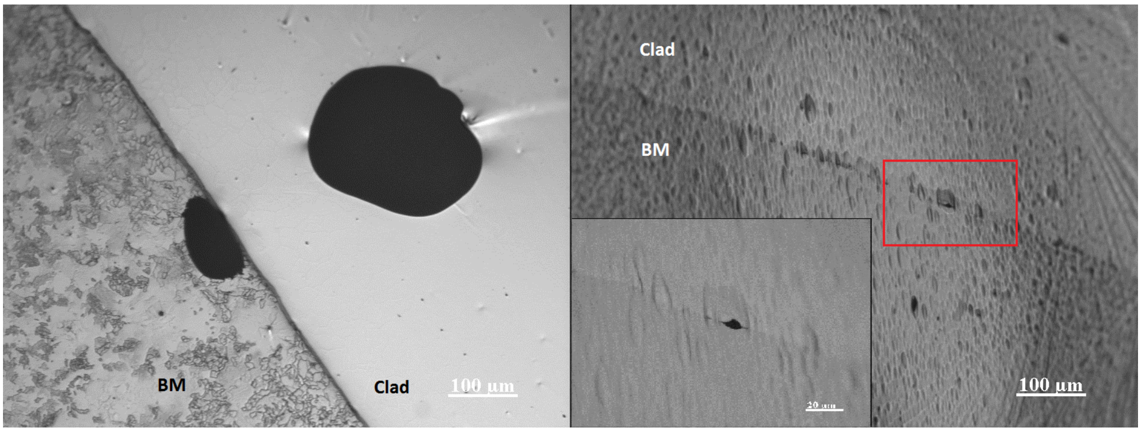

Figure 29 - Specimen surface after final ion thinning. Left: Electropolished. Right: Dimpled and ion thinned. The inserted image shows the hole at the interface at a higher magnification (red rectangle).

Both electropolishing and ion thinning resulted in a hole at the interface, and a thinned region adjacent to the hole. However, thinning of the actual interface proved difficult. The areas surrounding the interface thinned, whereas the interface remained fairly thick, and with a wedge-like shape, thus limiting the areas which could be investigated. Additionally, the BM appeared to thin more rapidly than the clad. Various ion thinning parameters were tested during this phase. A TEM specimen containing the dissimilar interface was obtained by adjusting the ion beams to only thin from the clad side, as this material thinned more slowly than the BM side. However, the specimen was still fairly thick, so that the sample could only be investigated in STEM mode.

Investigations were performed using JEOL JEM-2100F FEG 200 kV (field emission gun) TEM. Due to time limitations, the TEM was operated by an experienced user, not the author. The TEM was operated in microscopy mode (dark field and bright field), diffraction mode, STEM mode. Additionally, energy-dispersive spectroscopy (EDS) analysis was performed in STEM mode on selected areas.

TEM images and diffraction patterns were analyzed using Gatan's Digital Micrograph®, and analysis of EDS data was obtained using AZtec®. Diffraction patterns were indexed by measuring the distances between the reflexes in reciprocal space and converting them into distances in real space. In cases some cases, there was no reciprocal scale bar in the diffraction pattern. Here, the relationship between the number of pixels and reciprocal distance was found from a known diffraction pattern with the same camera length, and used to calculate the distance between reflexes. MacTempasX was used to obtain theoretical diffraction patterns for various zone axes corresponding to the crystal structure being investigated. The interplanar spacing *d* from the theoretical diffraction pattern was then compared with the interplanar spacing from the experimental diffraction pattern, in order to confirm the two corresponded.

4.4. Fracture Toughness Testing

4.4.1. Specimens

Compact tension (CT) specimens were machined from pipes in the unwelded condition by Nomek AS using electro-discharge machining (EDM). Prior to machining, the specimens were lightly etched in 2% Nital to better reveal the dissimilar interface. The specimen dimensions, given in Figure 30, were measured according to BS 7448[71] prior to testing, see Appendix A.

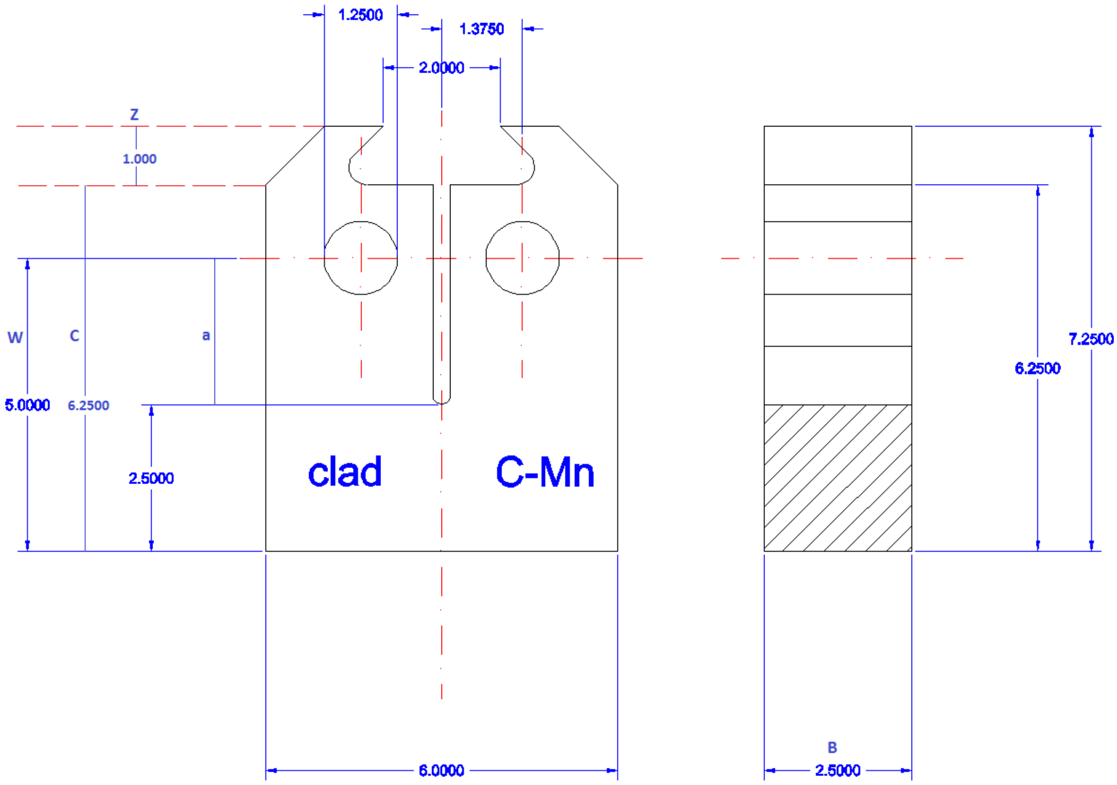

Figure 30 - Compact tension specimen geometry, W = 5 mm, B = 2.5 mm, a = 2.5 mm, C = 6.25 mm, z = 1.0 mm.[72]

New specimen holders and pins were also machined to fit the dimensions of the specimens. The sample was notched using EDM, rather than fatigue pre-cracking, as it was deemed impossible to produce a fatigue crack which propagated exactly along the dissimilar interface. The notch was machined to an initial crack length to width ratio a_0/W of 0.5. The notch tip was positioned on the dissimilar interface. As discussed in section 2.4.3, a sharp crack is required in order to obtain result that represent the true fracture toughness of the material. However, as the goal of these tests was to compare the properties of the different material combinations and the effect of hydrogen, the absence of a fatigue pre-crack should not render the tests invalid for this.

4.4.2. Testing

Slow strain rate tests were done in accordance with BS 7448-1[71] where possible. Testing was performed using a Cormet Slow Strain Rate Test rig, as seen in Figure 31, with the pertaining software.

Testing was first performed in air, using machined clip gages to measure the CMOD, as seen in Figure 31. The machine displacement and load was also measured. For testing under CP, the use of clip-gages was not possible, so that only the load and machine displacement was measured. A correlation between load, CMOD and displacement for testing in air was established in order to determine the CMOD for testing under CP. This is described in section 4.4.3. For all testing, data was logged every 10 seconds, and the software input parameters were as follows: P = 0.05, I = 0, H = 1.0.

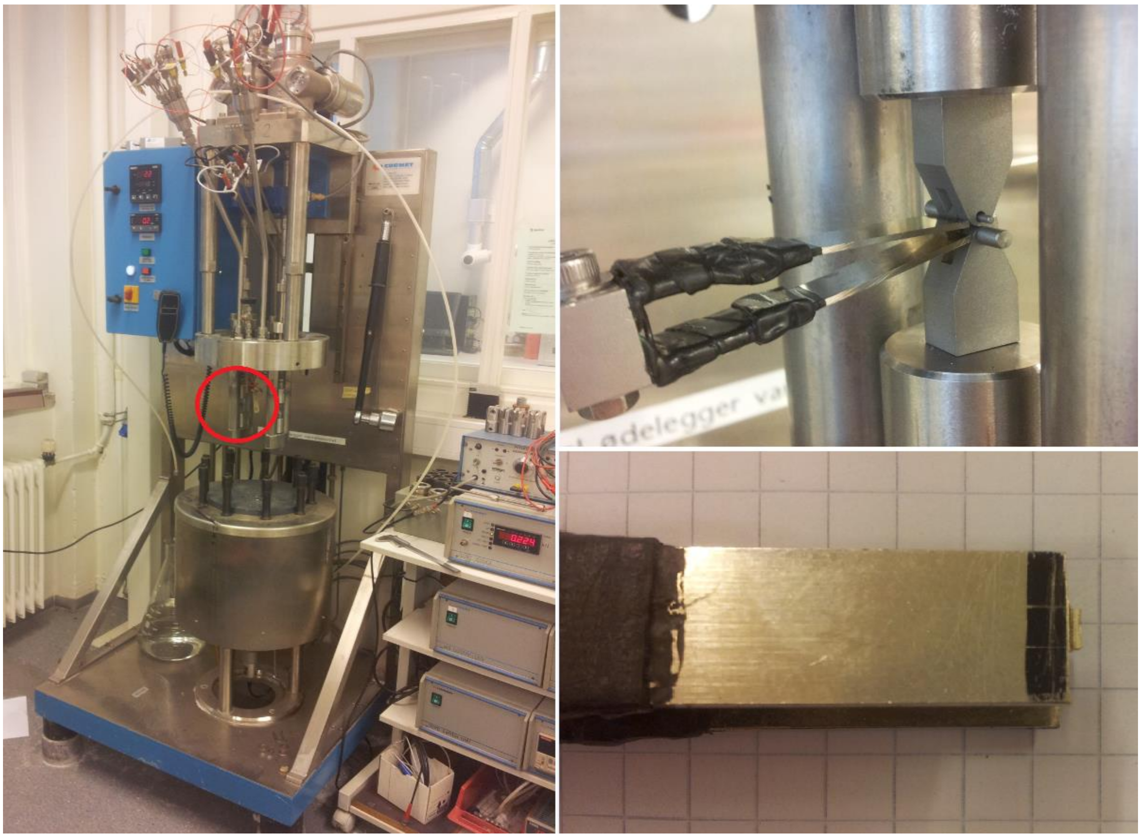

Figure 31 - Cormet test rig showing the loading unit (red circle), specimen setup and machined clip gage.

Initial testing was performed in air using a loading rate of 10 N/min, corresponding to the stress intensity rate given in equation 4.1. The stress intensity factor, K, was calculated according to equation 2.3 and 2.4.

$$\frac{dK}{dt} = 9{,}2 * 10^{-3} MPa\sqrt{m} s^{-1} \tag{4.1}$$

In order to investigate hydrogen assisted cracking (HAC), the loading rate must be sufficiently slow, in order to allow hydrogen adequate time to diffuse to the fracture process zone (FPZ). For this reason, a loading rate of 0.74 N/min was used for final testing, corresponding to the stress intensity rate given in equation 4.2.

$$\frac{dK}{dt} = 6.8 * 10^{-4} MPa\sqrt{m} s^{-1} \tag{4.2}$$

This is in accordance with work done by Lee & Gangloff [73], regarding investigations of HAC in an ultra-high strength martensitic steel. The loading rate (0.74 N/min) was calculated based on the results of the initial testing (10 N/min), see Appendix B.

For HISC testing, the specimens were immersed in a 3.5 wt% NaCl solution at room temperature (22 ˚C) with an applied potential of -1050 mV_{SCE}, corresponding to CP in seawater[74], for 24 hours prior to testing. The setup is shown in Figure 32. A polymer composite transition was used to isolate the specimens from the machine. Based on the diffusion coefficient for X70 pipeline steel, determined by [75] to $2.50*10^{-6}$ cm^2/s or 0.9 mm^2/h, a hydrogen concentration of 1.27 ppm is expected 1.25 mm from the surface after 24 hours of pre-charging, deeming a pre-charging time of 24 hours suitable.

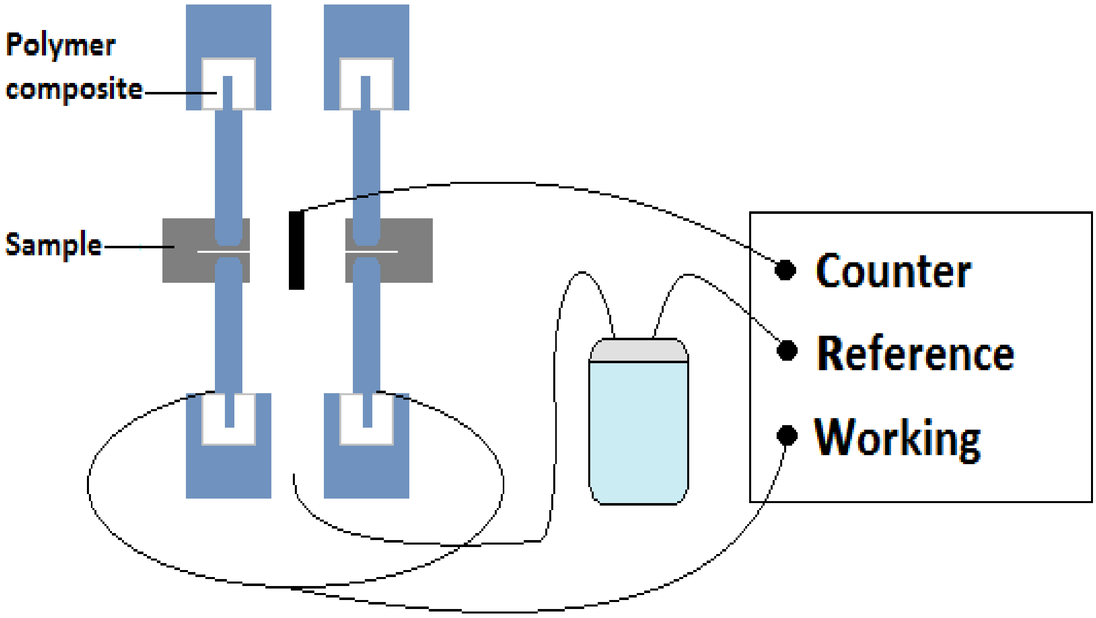

Figure 32 - Cathodic protection test setup. Counter, reference and worknig denotes the three electrodes.

A load of approximately 20-30 N was applied in order to ensure sufficient electrical contact during the pre-charging period.

4.4.3. Analysis of Test Data

After testing, the specimens were cracked open using liquid nitrogen. The crack length (a_0) was measured according to ISO 12135[76], but due to the small geometry of the specimen, 5 measurements were made, as opposed to the required 9. The measurements were made at equally spaced points across the sample, and the corresponding a_0 was calculated according to equation 4.3, which is modified from the aforementioned standard.

$$a_0 = \frac{1}{4}\left(\frac{a_1+a_5}{2} + \sum_{i=2}^{i=4} a_i\right) \tag{4.3}$$

Where a_1 and a_5 represent the two outer measurements. Additionally, the ratio between a_0 and W was calculated, see Appendix A, as this is required to be within the range given in equation 4.4.

$$0.45 < \frac{a_0}{W} < 0.55 \tag{4.4}$$

The method for obtaining the load-CMOD correlation is presented in detail in Appendix C, so that only a brief description is given here. The slope of the linear part of the load-displacement and load-CMOD curve was corrected to fit through x-y origin of the graph for all tests. For the load-displacement curves, the slope was set to fit the steepest part of the curve, as the initial part of the displacement curve was not linear. This is due to the small size of the specimens relative to the loading unit, which influences the initial displacement measurements as the various components of the system settle in. The slopes obtained were used to graph a corrected load-displacement and load-CMOD curve, showing only the plastic displacement and plastic CMOD, i.e. the V_p. The relationship between V_p and the corrected displacement, both plastic, was obtained for specimens in air, and found to be a factor of 1.66 for sample A and 1.59 for sample B. This factor was used to determine the plastic CMOD for specimens tested under CP. In other words, V_p for CP specimens was obtained by multiplying the measured displacement with the corresponding factor. The CTOD at maximum load was calculated from equation 2.6 and 2.7, given in section 2.4.3.

4.4.4. Fracture Surface and Crack Path Investigations

The CT specimens were rinsed in an ultrasonic bath with acetone before the fracture surface was investigated in SEM. The investigations focused on the areas close to the EDM notch. Images were obtained in secondary electron (SE) mode, using an aperture of 120 µm, 15 kV acceleration voltage, approximately 20-30 mm working distance and in high current mode.

The CT specimens were embedded in 40 mm diameter molds for cross sectional investigations of the fracture path. For all samples, the right side of the clad and left side of the BM side was placed facing down, thus corresponding to the area of investigation. The samples were cold embedded using Struers EpoFix® resin and EpoFix® hardener. The mixing ratio was 25 parts resin and 3 parts hardener. Curing time was 8 hours.

The samples were wet grinded by automated Struers TegraForce-5, with SiC grinding paper (220, 320, 500, 1000, 2400), followed by diamond polishing using MD Mol (3 µm) and MD Nap (1 µm) cloths with the corresponding diamond suspension. Between grinding and polishing, and between the polishing steps, the specimens were washed with soap and water, rinsed in ethyl alcohol and dried rapidly with a blow dryer. The samples were etched in 2% Nital for 20 seconds to reveal the BM. The clad was not etched, as the crack had not propagated into this region.

For samples 1-3 (air), approximately 2 mm of material was removed, as the material was eliminated at a higher rate than expected. For samples 4-5 (tested under CP), approximately 1 mm was removed, facilitating cross sectional investigations near the center of the specimen.

As will be shown in the results section, the crack propagated on the BM-side for samples without a Ni-interlayer, and at the BM-Ni interface and slightly into the Ni interlayer for samples with a Ni-interlayer. Additionally, the Ni-interlayer is not easily distinguished from the clad in the etched condition. For this reason it was not deemed necessary to etch the clad and Ni part of the specimen.

Light optical microscopy (LOM) investigations were performed using Leica DMI500 M.

5. Results

5.1. Microstructure Characterization

SEM investigations were performed on sample B (no Ni-interlayer) and sample A (Ni-interlayer) in the etched condition, and the results are presented in Figure 33 and Figure 34. For all images, the BM is located in the upper part of the image.

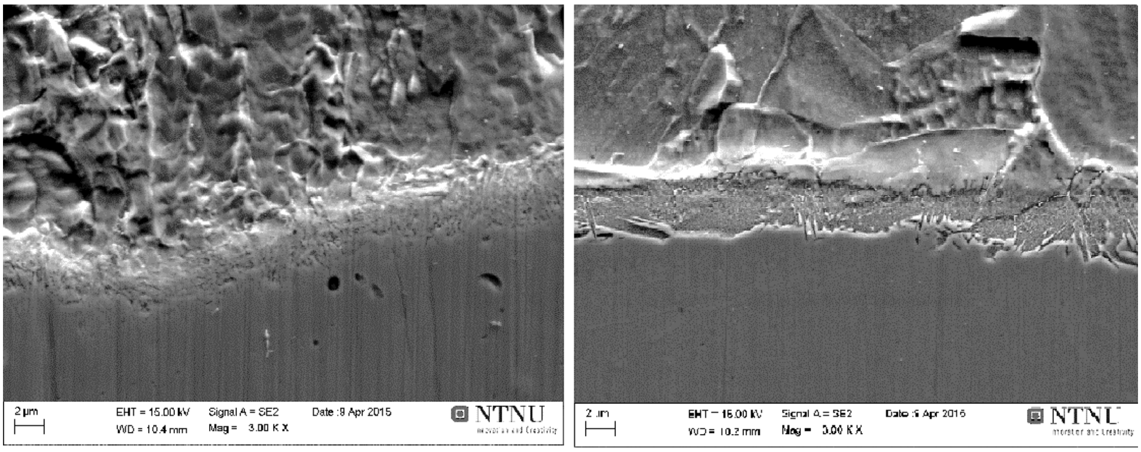

Figure 33 – Sample B: SEM image (SE) of clad-BM interface. Left: 0.091 mm from triple point. Right: 11.34 mm from triple point. Etched in 2% Nital.

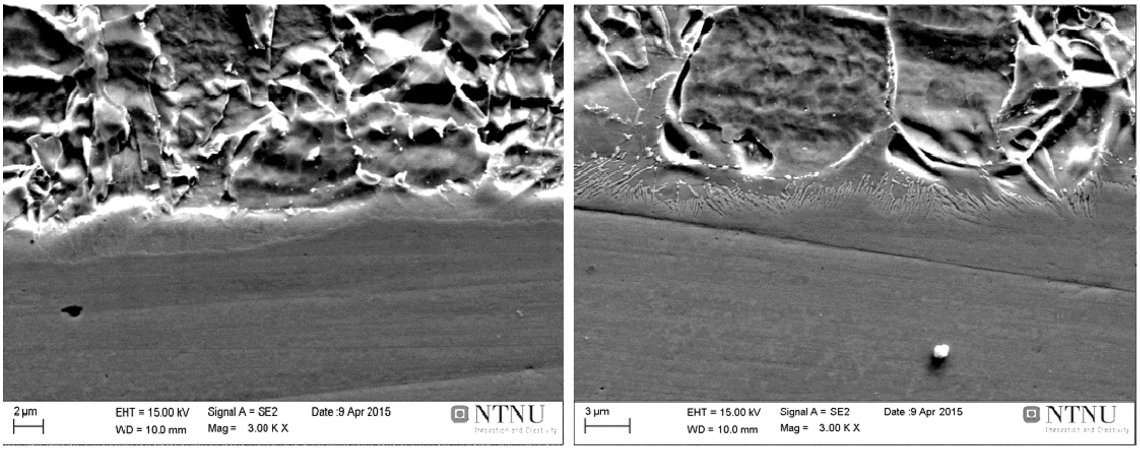

Figure 34 - Sample A: SEM image (SE) of clad-Ni-BM interface. Left: 0.125 mm from triple point. Right: 11.50 mm from triple point. Etched in 2% Nital.

For both samples there is a pronounced difference in appearance of the interface, when comparing the area close to the triple point with the area further away. In both cases, a needle like structure can be observed near the clad side of the interface, in the area far away from the triple point. Sample B (no Ni-interlayer) appears to contain a band of approximately 2.5 µm in connection to the needle-like structure. In sample A (Ni-interlayer), the needle-like structure is present over a much narrower area, and does not appear to be as continuous as in sample B.

Closer to the triple point, i.e. in the heat affected zone (HAZ), the pronounced needle-like structure cannot be observed in either of the samples. For sample B, the interface appears more washed out, although slight traces of what appears to be the aforementioned needle-like structure can be observed in the left image in Figure 33.

A close up of the needle-like structure of the dissimilar interface in sample B is shown in Figure 35. The image is taken some distance (> 10 mm) from the triple point. This region is further investigated in TEM, and the results are presented in section 5.2.

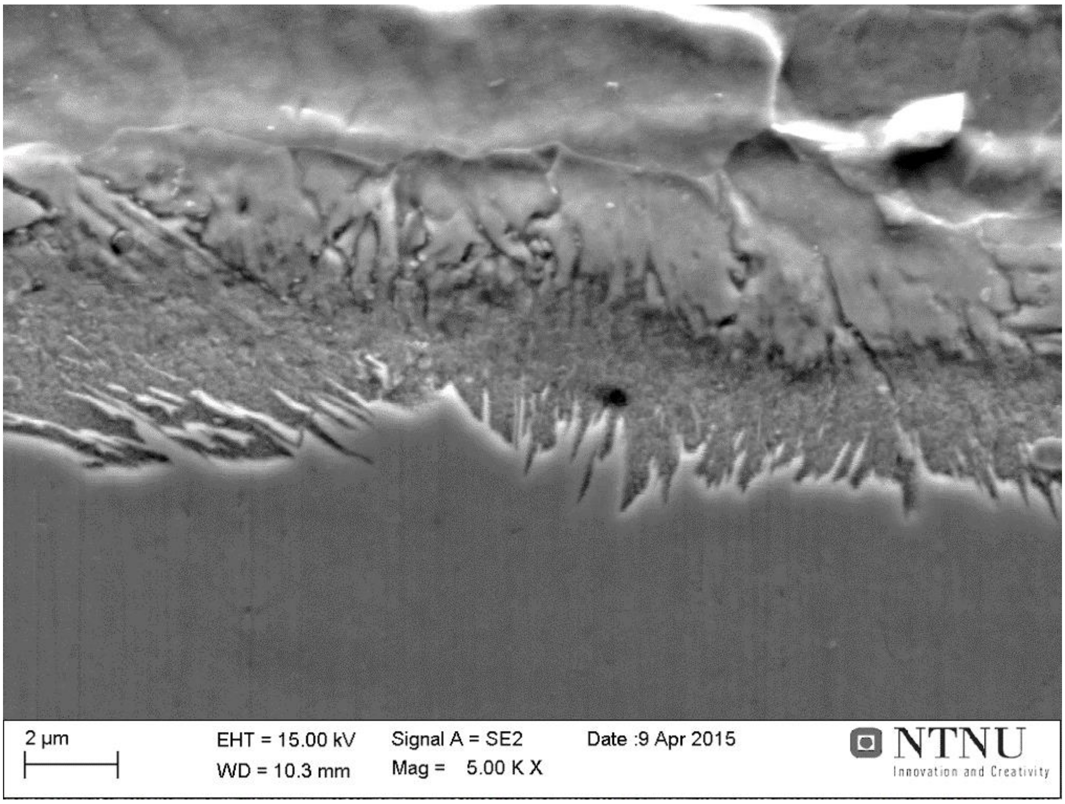

Figure 35 - Sample B: SEM image (SE) of clad-Ni-BM interface, 11.70 mm from triple point.

5.2. TEM Investigations

The interface region and carbide precipitation in the clad was the main focus of the TEM investigations. The results are presented below.

The clad immediately adjacent to the interface showed diffraction patterns with super reflexes, in addition to reflexes from the austenitic matrix, as seen for two different orientations in Figure 36a and Figure 37a. Both the matrix and the precipitates showed a cubic crystal structure. The diffraction patterns are obtained with a (110) and (111) zone axis, showing an interplanar spacing of 1.79 and 2.07 Å for the austenite matrix. The super reflexes had a periodicity of three times the matrix reflexes, indicating a lattice parameter *a* three times that of the austenite matrix, corresponding to the $M_{23}C_6$ carbide.[24] The diffraction pattern from the BM side immediately adjacent to the interface, seen in Figure 37b, corresponds to a BCC crystal structure, and is obtained with a (111) zone axis, showing an interplanar spacing of 2.03 Å.

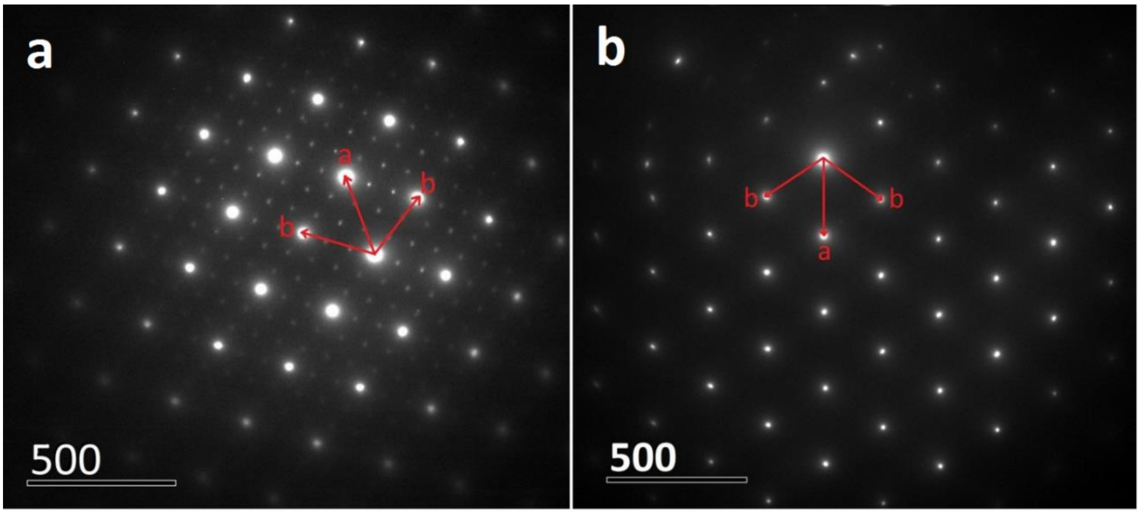

Figure 36 – Electron diffraction pattern showing: a) Clad immediately adjacent to interface with carbide precipitation. The intense reflexes are from the matrix (γ), the faint super reflexes from the carbides. b) Clad approximately 130 µm from interface showing no carbide precipitation. a: $(110)_\gamma$: d = 1.79 Å, b: $(110)_\gamma$: d = 2.07 Å.

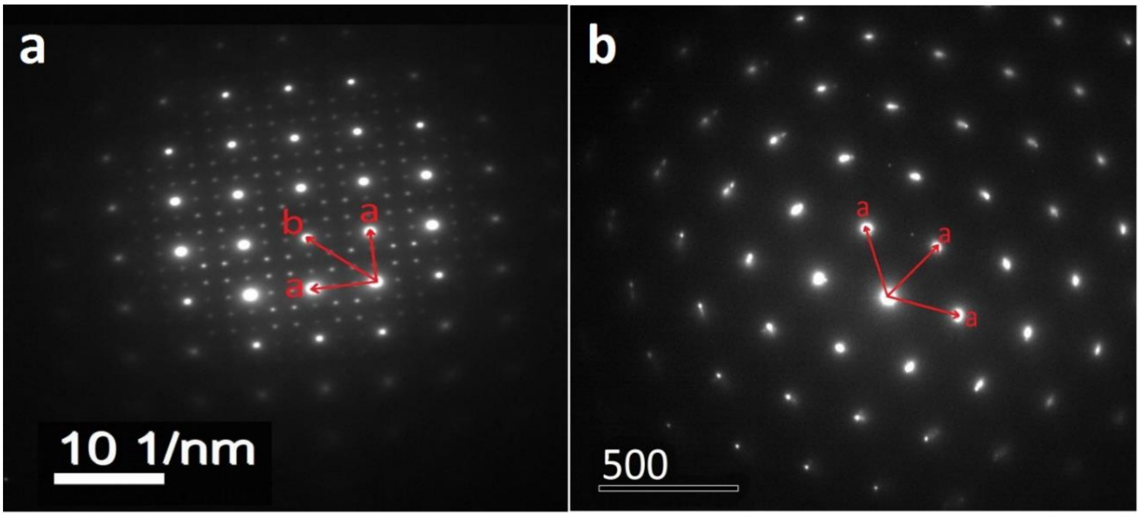

Figure 37 - Electron diffraction pattern showing: a) Clad immediately adjacent to interface with carbide precipitation. The intense reflexes are from the matrix (γ), the faint super reflexes from the carbides. a: $(100)_\gamma$: d = 1.79 Å, b: $(100)_\gamma$: d = 1.27 Å. b) BM immediately adjacent to interface showing a BCC crystal structure. a: $(111)_\alpha$: d = 2.03 Å.

Micrographs of the carbides in the clad interface region, which are responsible for the super reflexes observed in the figures above, can be seen in Figure 38. In the bright field image, dislocations can be observed near the carbides. The dark field image clearly shows the size and morphology of the carbides. The small and finely dispersed carbides were present all along the clad interface.

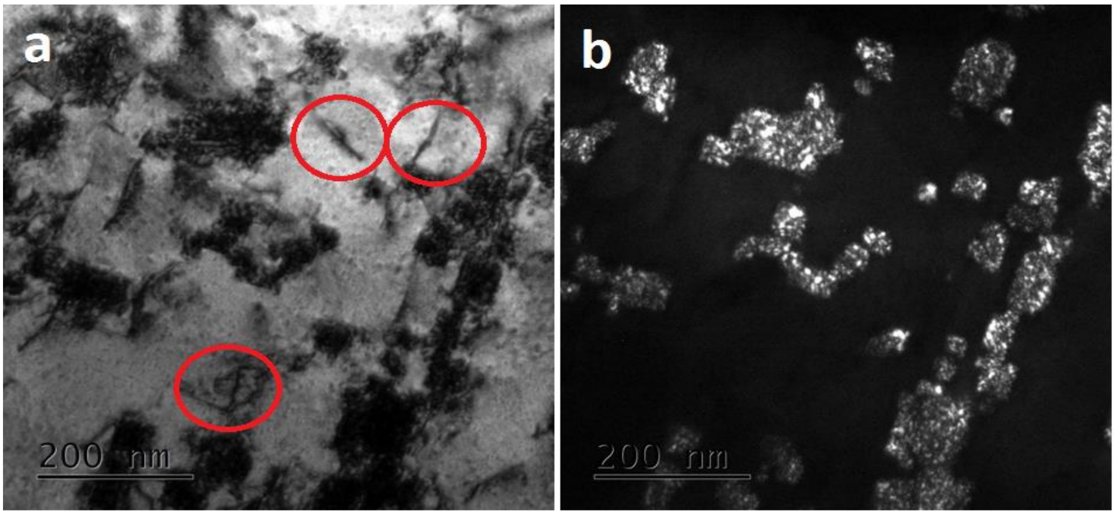

Figure 38- Carbides in the clad interface region. Bright field (a) and dark field (b) imaging. The red circles show dislocations.

EDS mapping of the clad immediately adjacent to the interface revealed an accumulation of Cr, and slight depletion of Fe at grain boundaries, and within grains, as can be seen in Figure 39 and Figure 40. The Cr-enrichment and Fe-depletion corresponds to the fine, bright features seen in Figure 39. No apparent carbon accumulation was observed.

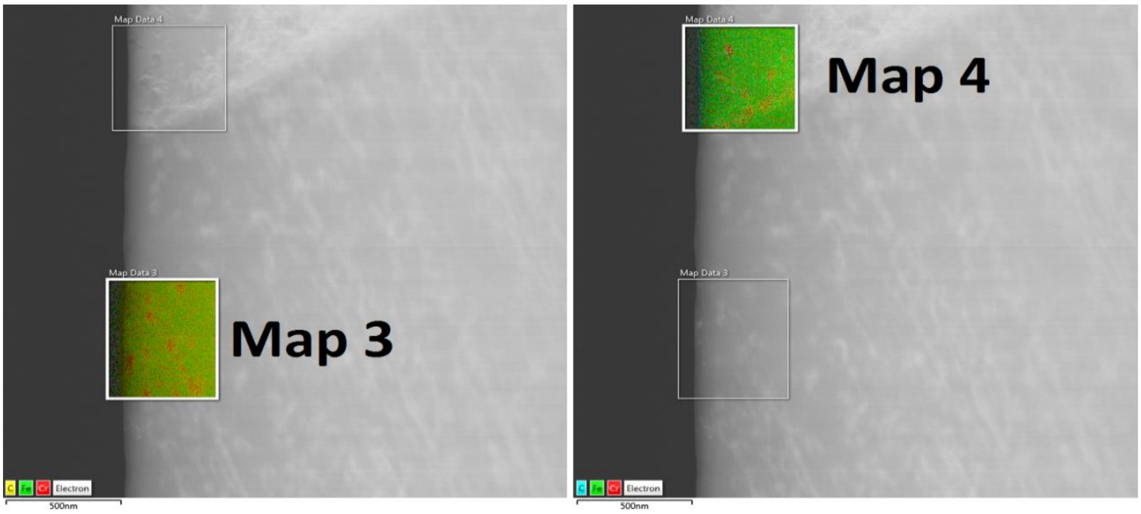

Figure 39 - EDS map of clad immediately adjacent to interface. A grain boundary can be seen in the upper left corner. The detailed maps are presented in Figure 40.

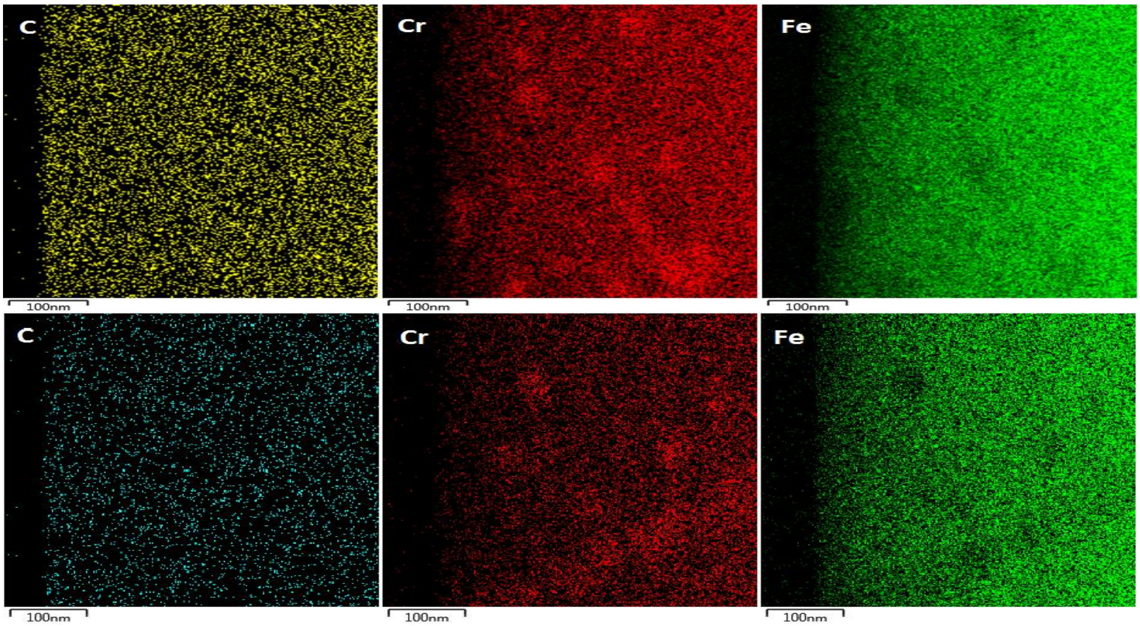

Figure 40 – EDS maps of area 3 (top) and area 4 (bottom) shown in Figure 39.

A lath-like morphology was observed on the clad side immediately adjacent to the interface, as seen in Figure 41. This feature was only visible in STEM mode. The laths appeared to have a parallel orientation, showing variation in mainly Ni and Mn in between laths. Diffraction patterns obtained in this region showed an austenitic structure with super reflexes, such as those presented in Figure 36 and Figure 37.

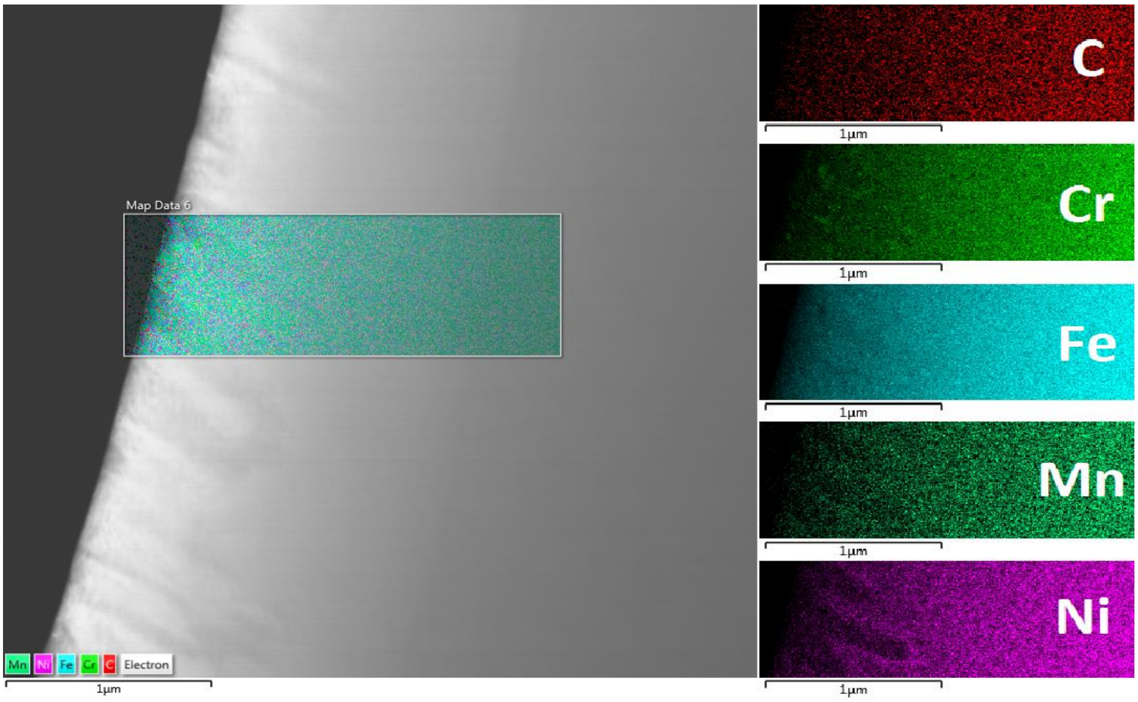

Figure 41 - EDS map of clad adjacent to interface. Note the lath like morphology of the area close to the hole.

The interface region was not easily distinguished from the surrounding clad and BM, as can be seen in the STEM images in Figure 43. No distinction was possible in standard TEM mode due to the thickness of the interface region. A lath-morphology can be observed at the interface region.

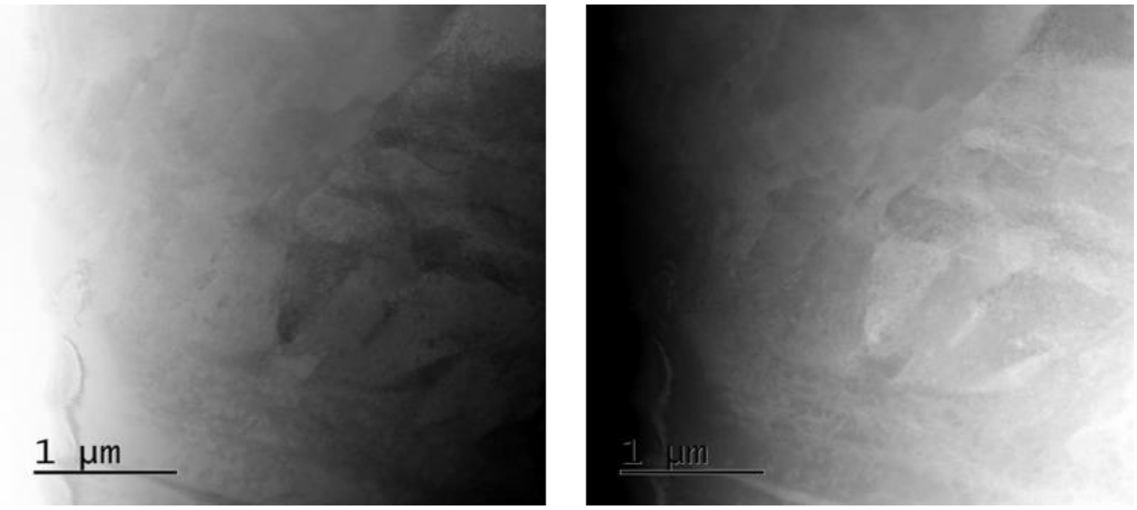

Figure 42 - STEM bright field (left) and dark field (right) images of the interface region. The BM is located at the top, the clad at the bottom. See Figure 43.

EDS mapping of the interface region, see Figure 43, showed segregation of Cr to carbides. Fe depletion can be observed at the larger carbides. The distribution of Ni and Cr shows the transition from the BM at the top to the clad at the bottom. The interface appears roughly horizontal from these EDS maps. The distribution of Ni at the interface region, towards the clad side, is somewhat jagged.

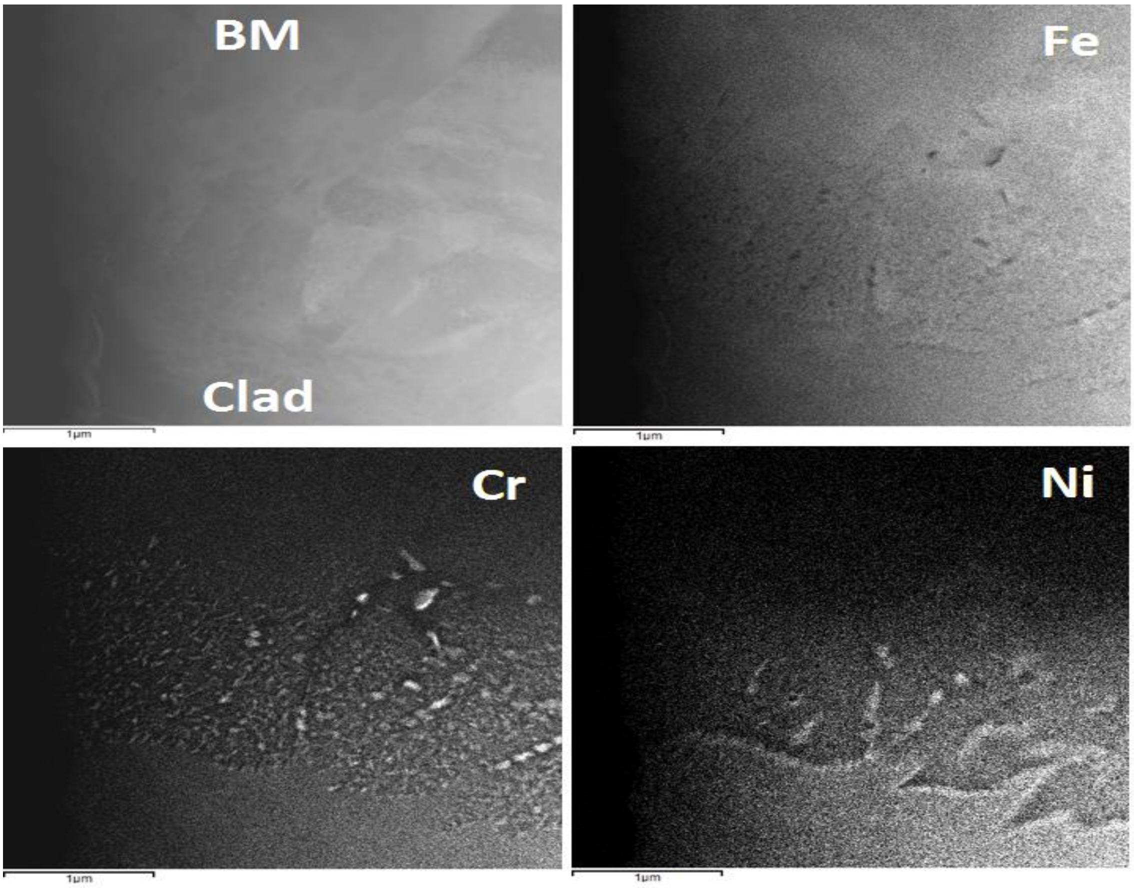

Figure 43 - Clad-BM interface region. STEM image (upper right) and EDS maps.

5.3. Fracture Toughness

For sample A, the load-time plots, seen in Figure 44, appeared almost identical for both testing in air and CP[1], although a slightly higher maximum load was obtained for one of the CP specimens (A4), and a slightly lower maximum load for the other (A5). For sample B, the maximum load during CP testing was somewhat lower than the maximum load obtained in air, see Figure 45, illustrating that the presence of hydrogen has reduced the time to failure, and thus reduced the critical load. The time-load curves for the initial test, performed at 10 N/min, was almost identical to the ones performed at the lower loading rate of 0.74 N/min, and is thus not included here.

For the specimens tested in air, the load-CMOD plots, seen in Figure 46, are almost identical for both loading rates. The two materials, however, differ somewhat. Sample A (Ni-interlayer) experienced failure at a lower CMOD value than sample B, which shows more ductility. It should be noted that this curve presents the total CMOD, i.e. both the plastic and elastic component.

1) The initial load value is above zero for the CP specimens for sample A, ref. Figure 44. This is attributed to the applied load necessary to obtain proper electrical contact during pre-charging.

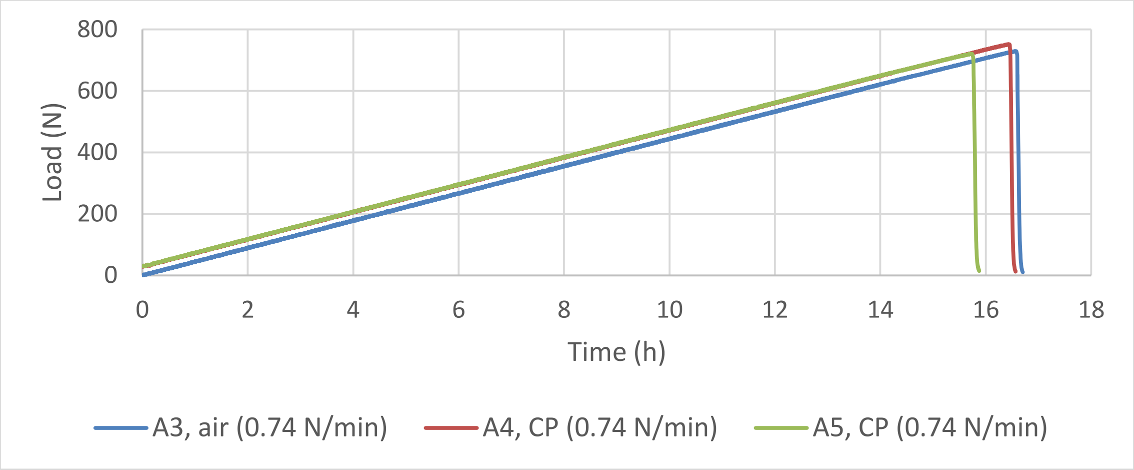

Figure 44 - Sample A. Load-time plot.

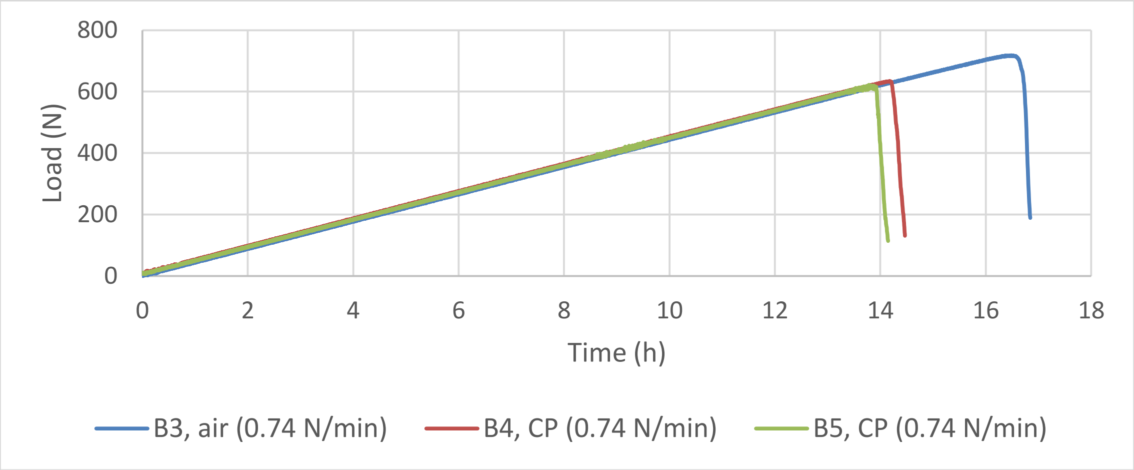

Figure 45 - Sample B. Load-time plot.

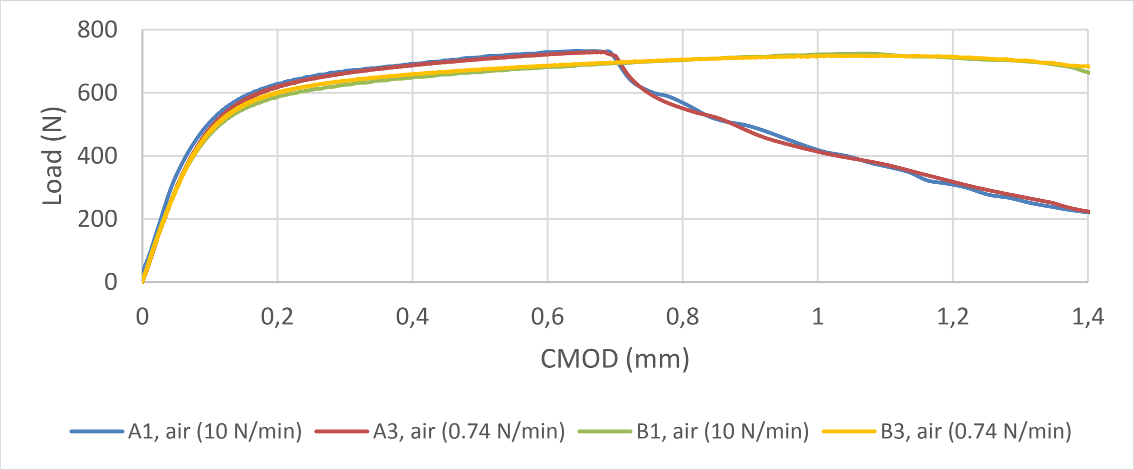

Figure 46 - Load-CMOD plot for specimens tested in air.

The correlation used to obtain the load-V_p curves, as described in section 4.4.3, is presented in Appendix C. The load-V_p curves is presented in Figure 47 and Figure 48 for sample A and B, respectively. See Appendix D for the individual load-V_p curves.

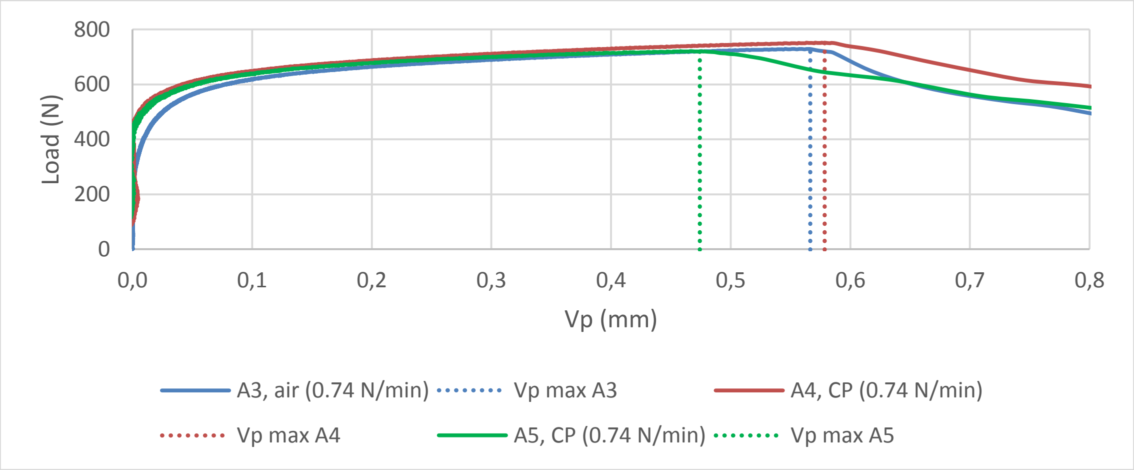

Figure 47 - Load-Vp plot for sample A (test 1 and test 5).

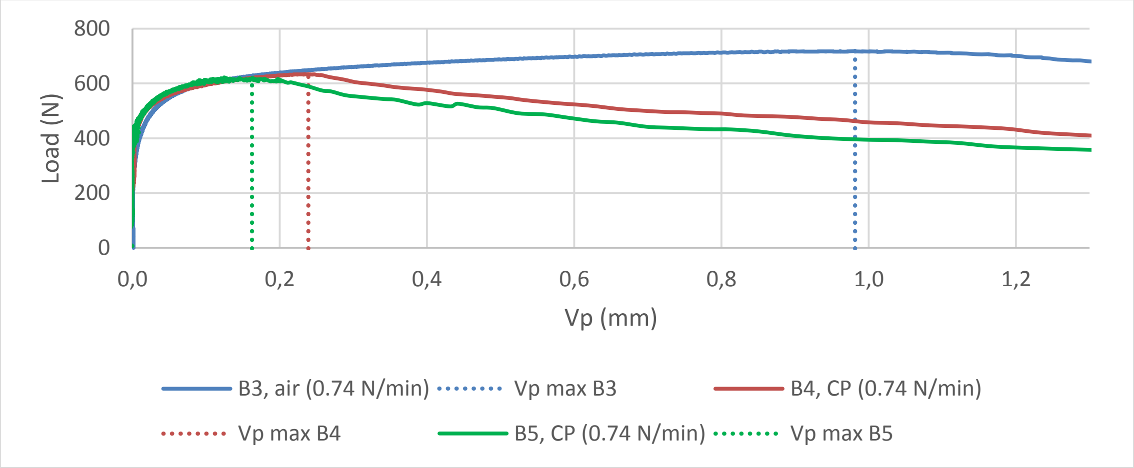

Figure 48 - Load-Vp plot for sample B (test 1 and test 5).

For sample A, the load-V_p curves were fairly similar for testing in both environments, showing a slight reduction in maximum load and CMOD for test 5, and a very slight increase for test 4, indicating little to no effect of hydrogen. For sample B, the load-V_p curves shows a significant reduction in maximum load and CMOD for samples tested under CP indicating hydrogen has influenced the failure.

The maximum obtained load and corresponding plastic CMOD (V_p) and total CTOD (δ) is presented in Table 6 for specimens tested in air. The determination of V_p is performed graphically, and is described in detail in Appendix C, and δ is calculated from equation 2.6 and 2.7, given in section 2.4.3. Generally, sample A showed a slightly higher maximum load than sample B for all environments. The CTOD for specimen A was fairly constant for both environments, showing an average reduction of 7 %, indicating no mentionable influence of hydrogen. Sample B showed more plastic deformation than sample A, resulting in larger CMOD and CTOD values. The CTOD values for specimen B was significantly lower for the tests performed under CP, showing an average reduction of 77 %, indicating that hydrogen has influenced the failure mechanism, and thus lowered the fracture toughness.

Table 6 - Overview of maximum load, and V_p and δ_{pl} at maximum load.

Environment	**Sample**	**Max load [N]**	**V_p [mm]**	**δ [mm]**
Air, 10 N/min	A1	733	0.536	0.110
Air, 0.74 N/min	A3	729	0.566	0.116
CP, 0.74 N/min	A4	752	0.578	0.119
CP, 0.74 N/min	A5	721	0.474	0.096
Air, 10 N/min	B1	725	0.954	0.192
Air, 0.74 N/min	B3	718	0.981	0.195
CP, 0.74 N/min	B4	634	0.239	0.052
CP, 0.74 N/min	B5	620	0.162	0.037

5.4. Fractography

The fracture surface of the CT specimens were investigated using SEM, and the results are presented below. A selection of the most relevant results are presented here, as several parallel tests were performed, resulting in very similar results with respect to fracture surface appearance. See Appendix E for a more complete overview. All fractographs are taken from the specimens tested at a loading rate corresponding to 0.74 N/min. For all images showing both the EDM notch and the fracture surface, the fracture surface is in the upper part of the image. The two areas are distinguished by a yellow line. In order to better compare the effect of material and environment, the selected fractographs are presented together. Some images have been slightly edited (brightness and contrast) in order to render the areas of interest more visible when printed.

The fracture surface of sample A (Ni-interlayer) tested in air had a dimpled appearance, corresponding to ductile fracture by microvoid coalescence, as seen in Figure 49. The initial part of the fracture surface is flat. For testing under CP, the initial part of the fracture surface has a quasi-cleavage appearance, showing cleavage facets with some ductile regions, as seen in Figure 49, indicative of transgranular cleavage fracture. Approximately 100 µm into the length of the crack, see Figure 50, the fracture surface is dimpled, corresponding to ductile fracture. The initial part of the fracture, i.e. the area displaying cleavage fracture, appears to have propagated in the BM, as an elevated ridge can be seen on the clad fracture surface, and a corresponding small crevasse on the BM fracture surface, see Figure 50. It should be noted that when referring to the clad or BM in terms of fracture surface, it is the corresponding section of the specimen it is referred to. The actual crack path is addressed in the next section.

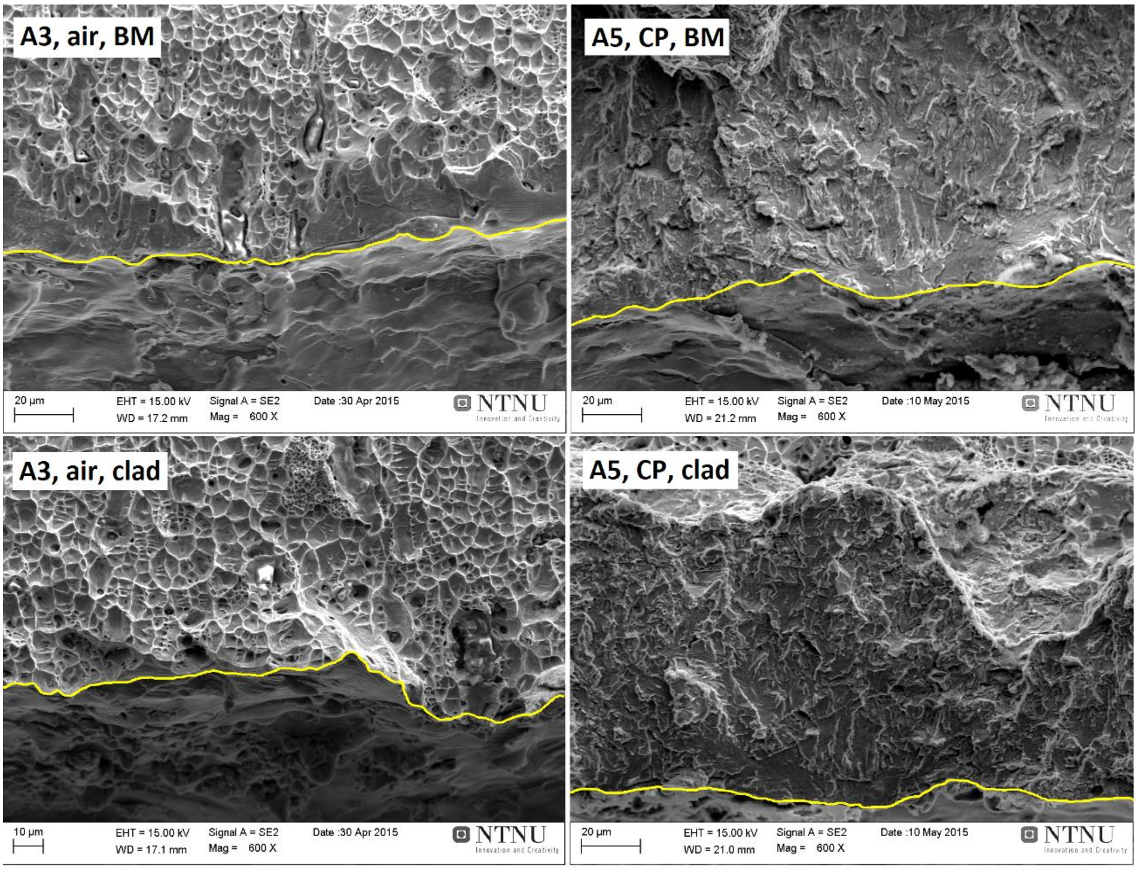

Figure 49 – Fracture surfaces for sample A. The term "clad" and "BM" denotes which section of the specimen the image is taken at. The image is taken at the center region. The fracture surface is above the yellow line.

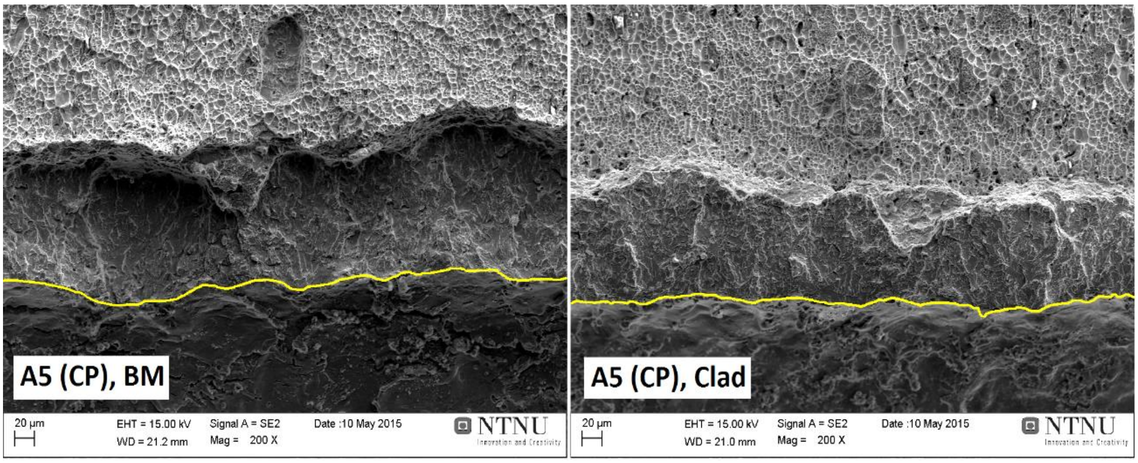

Figure 50 - Fracture surface of BM side and clad section of specimen for A5 (CP).

The fracture surface of sample B (no Ni-interlayer) tested in air, exhibited an initial flat fracture morphology, with some cleavage facets, followed by dimples further into the crack path on the clad section of the specimen, as seen in Figure 51 and Figure 52. The BM section of the specimen showed a dimpled fracture surface, as seen in Figure 51 and Figure 52. For sample B tested under CP, the initial part of the fracture surface showed a multifaceted appearance, indicative of cleavage fracture, followed by what appears to be a quasi-cleavage fracture surface, containing cleavage facets and some dimples, as seen in Figure 51-Figure 53. The fracture surfaces for testing under CP appears less ductile than for those tested in air, as seen in Figure 52 and Figure 53.

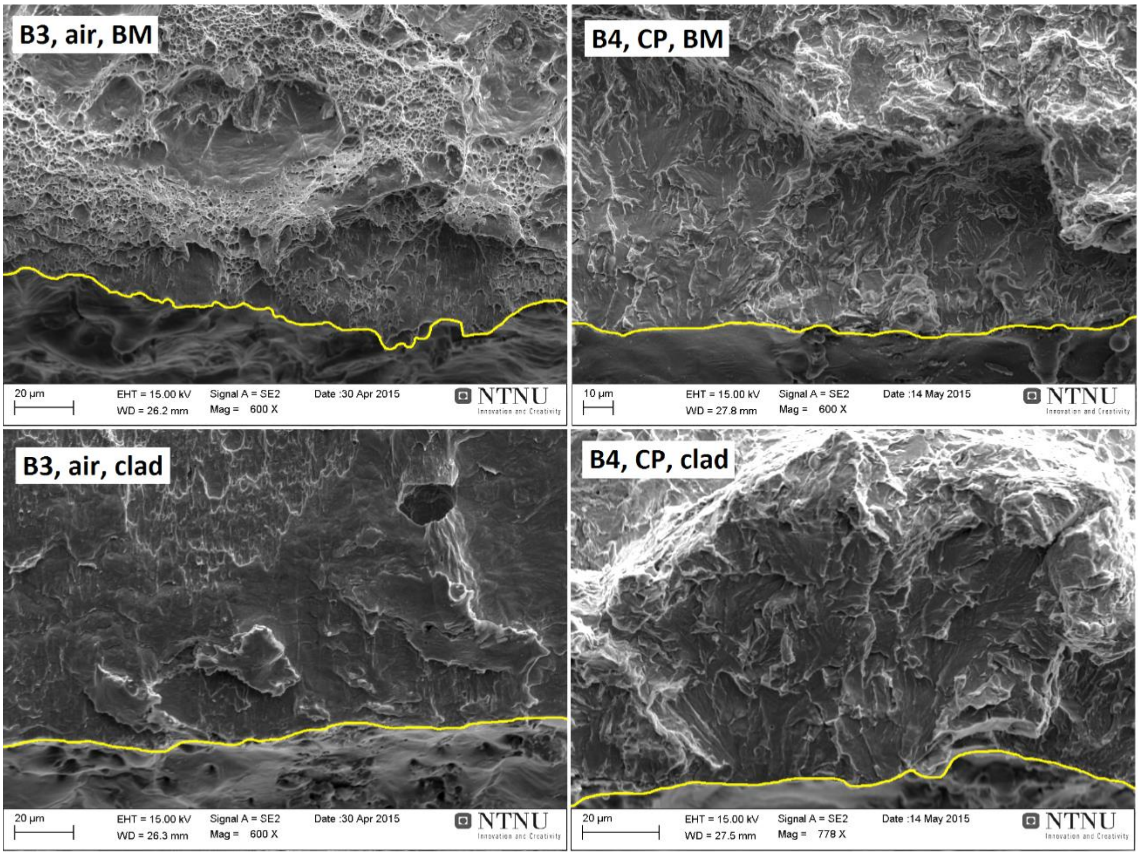

Figure 51 - Comparison of fracture surfaces for the clad section of specimen. The image is taken at the center region. The fracture surface is above the yellow line.

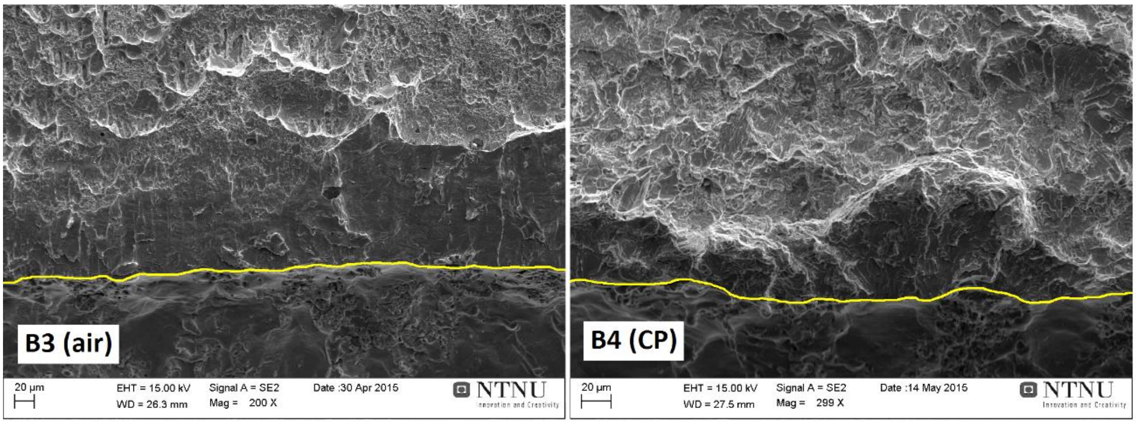

Figure 52 - Comparison of fracture surface for clad section of specimen. The image is taken at the center region. The fracture surface is above the yellow line. Note the difference in magnification.

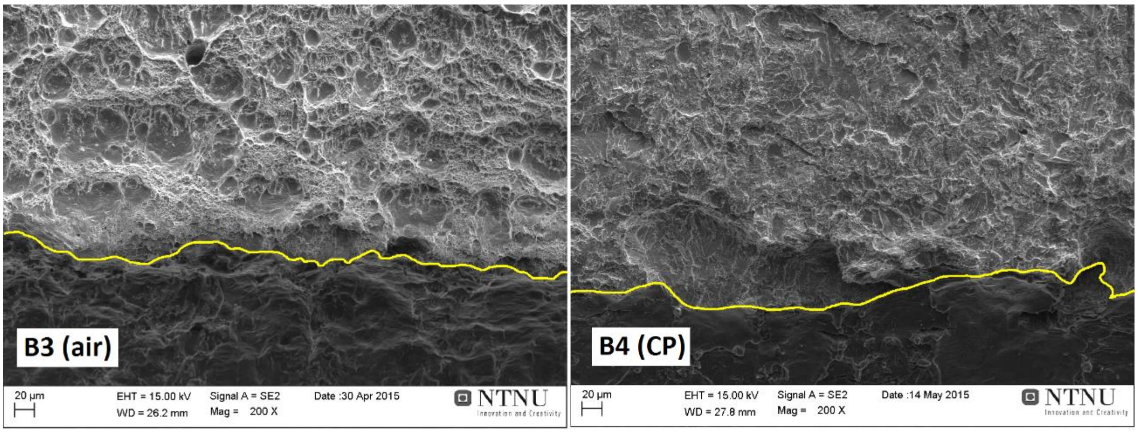

Figure 53 - Comparison of fracture surface for BM section of specimen. The image is taken at the center region. The fracture surface is above the yellow line.

5.5. Crack Path

The crack path was investigated in light optical microscope (LOM), and the results are presented briefly below. Only a selection of the most relevant micrographs are included.

For sample A (Ni-interlayer), the crack mainly propagated at the BM-Ni interface, slightly in to the Ni-interlayer for samples tested in air. For samples tested under CP, the crack initiated in the BM, followed by propagation along the BM-Ni interface, slightly into the Ni-interlayer as seen in Figure 54 and Figure 55. The Ni-interlayer can be seen as the pale, off-white, featureless band located slightly above the BM microstructure in Figure 54. In Figure 55, the Ni-interlayer cannot easily be distinguished from the clad. Previous work [68] has shown that the thickness of the Ni-interlayer is approximately 30-35 µm.

For sample B, the crack propagated in the BM immediately adjacent to the interface, and at the dissimilar interface, but on the BM side, as seen in Figure 56 and Figure 57. These observations were similar for testing in both environments, but for the samples tested in air, the crack propagated slightly more into the BM. For testing under CP, the crack mainly propagated at the dissimilar interface, but on the BM side.

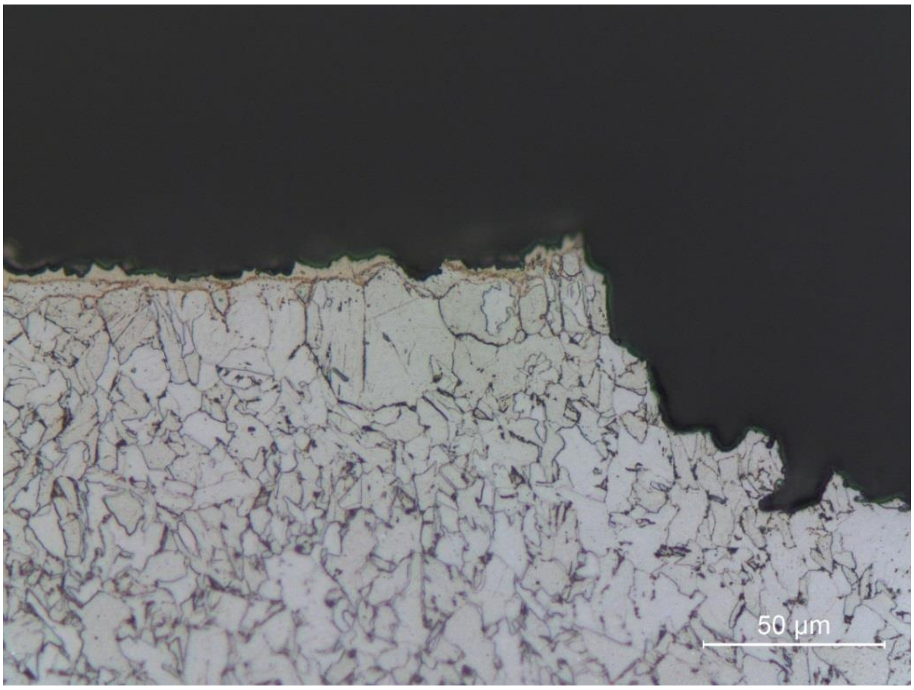

Figure 54 - Cross section micrograph of A5 BM, tested under CP.

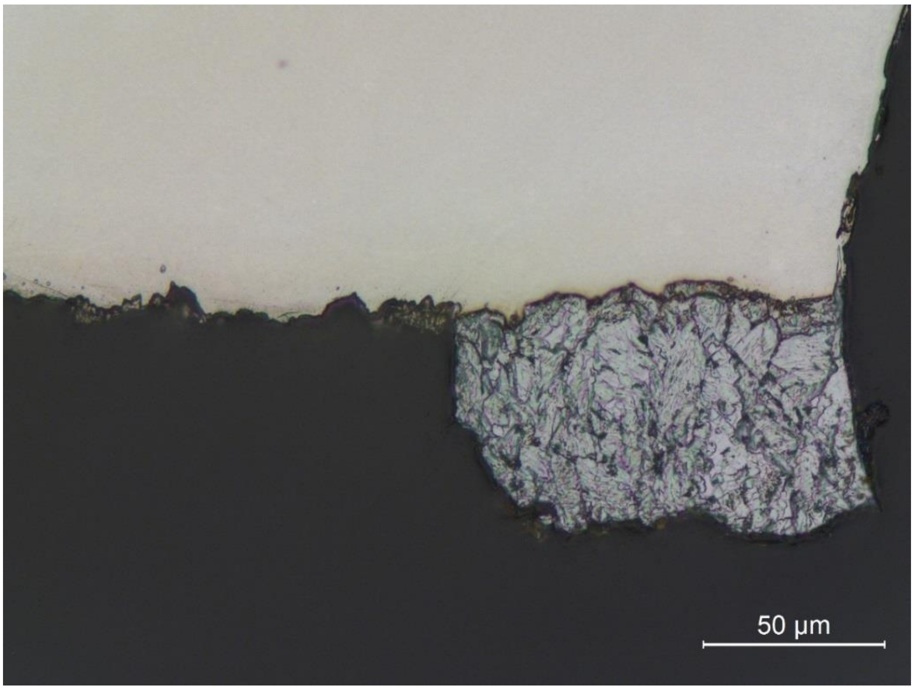

Figure 55 – Cross section micrograph of A5 clad, tested under CP.

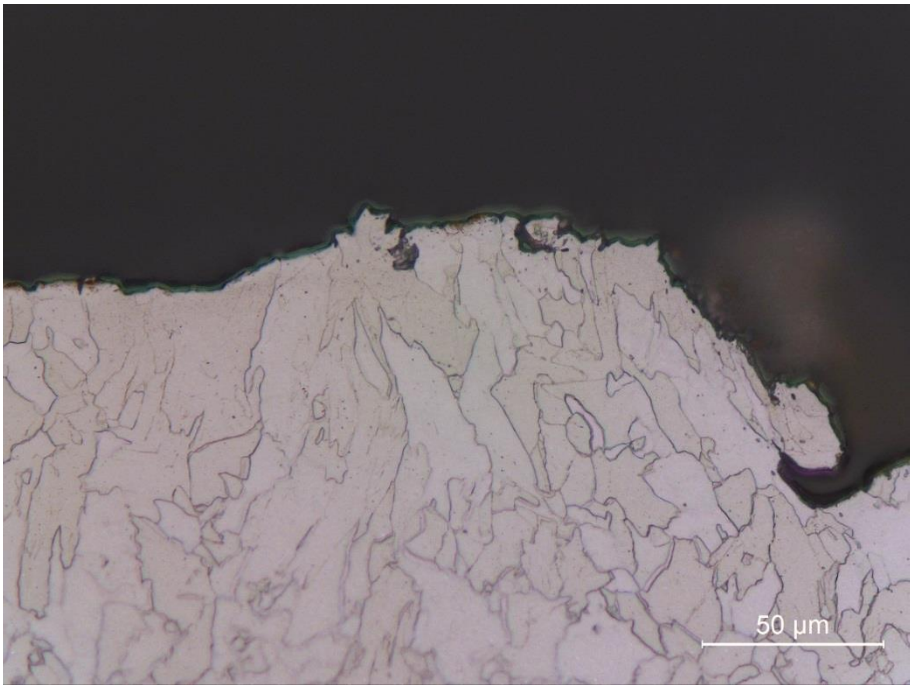

Figure 56 - Cross section micrograph of B4, BM, tested under CP.

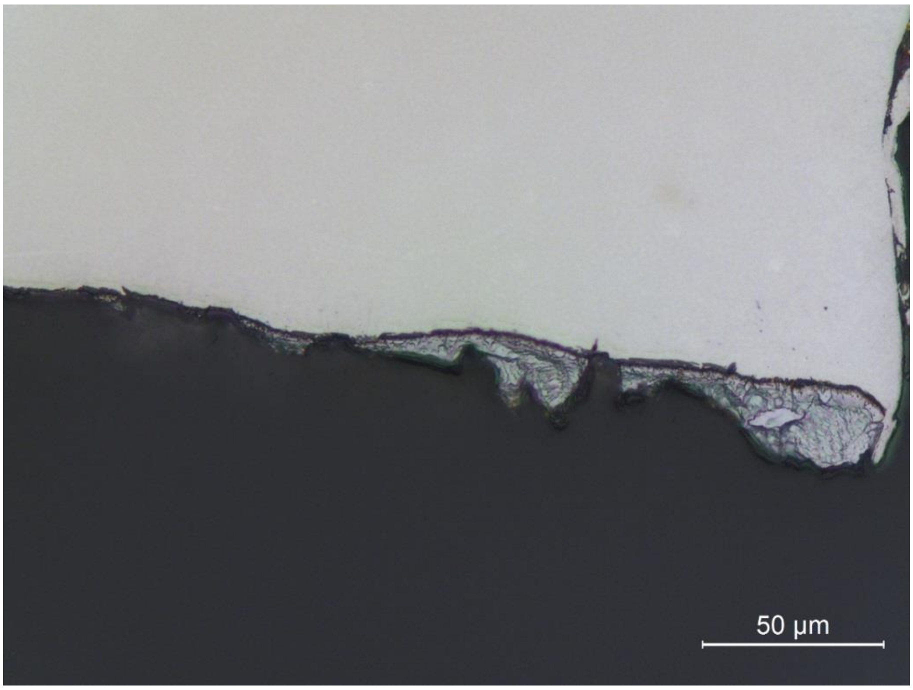

Figure 57 - Cross section micrograph of B4, clad, tested under CP.

6. Discussion

This chapter contains discussion and interpretation of the results presented in chapter 5, and is divided into three main sections. The TEM section addresses the features of the interface and clad region, i.e. the metallurgical aspects, whereas the fracture toughness section addresses the mechanical aspects. Finally, a third section is included to summarize and give an overview of the two preceding sections. The investigations performed in this thesis is correlated to the previous work presented in Chapter 3, so that where it is deemed relevant to the findings of this thesis, the results of the previous work is also discussed. This is referenced in the text.

6.1. TEM

6.1.1. Dissimilar Interface Characterization

For TEM investigations, proper sample preparation is the key to getting good results. Characterization of the dissimilar interface proved difficult, as proper thinning of the interface was hard to obtain. The different tinning rates of the clad and BM naturally complicated the thinning process. This is, however, solved by adjusting the sample preparation parameters, i.e. perform preferential dimpling on the side that thins slowly, or by adjusting the ion thinning parameters. Several ion thinning procedures were tested, but the interface region remained fairly thick, and sometimes wedge shaped, making TEM investigations difficult and limited to a very small region. The dissimilar interface could barely be distinguished in STEM mode, showing a jagged distribution of Ni at the interface region towards the clad side, and segregation of Cr to carbides. The BM immediately adjacent to the interface showed a BCC structure, indicating no presence of deformation induced martensite, which has a HCP crystal structure. The presence of thermally induced martensite, i.e. BCC or low tetragonality BCT martensite could not be determined. This is discussed in more detail later on.

As mentioned above, the interface showed no distinguishable contrast in TEM microscopy mode, making it difficult to be certain of which area was being investigated. For this reason, EDS mapping was continuously performed during TEM investigations, in order to assess the presence of the interface with respect to changes in the main alloying elements. EDS mapping confirmed the presence of the interface, but with little visible contrast. Fenske [59] investigated dissimilar interfaces in TEM, and found that ion thinned samples provided the highest quality specimens for TEM, but due to difficulties in selecting the desired area of investigation, a focused ion beam (FIB) technique was used in order to extract the samples. This, in addition to conversations with experienced TEM users, formed the basis for the selected sample preparation techniques used during the experimental stage. However, as discussed above, the samples were not sufficiently thin for proper TEM investigations. It should be noted that the samples investigated by

Fenske consisted of an interface between a base metal and a weld metal, i.e. where bonding was obtained by melting and solidification. In this thesis, the bond between the clad and base metal was obtained by hot rolling, resulting in a potentially more complex interface region due to deformation introduced during rolling, in addition to migration of alloying elements. If the interface is to be investigated further, a different approach to TEM sample preparation should be made.

Regarding the suspected presence of martensite at the dissimilar interface, the distinction between low carbon martensite with a BCC/BCT structure and BCC ferrite by electron diffraction patterns alone is near impossible. At low carbon contents, the martensite has low tetragonality, if any, meaning that the two phases will not easily be distinguished. Originally, the plan was to use electron diffraction patterns in combination with microscope images, in which the potential different phases would be distinguished by difference in contrast. Additionally, the high dislocation density of martensite relative to the matrix was also thought to be utilized. Unfortunately, as the interface was difficult to thin properly, the contrast obtained was poor, making it difficult to distinguish the interface from the adjacent bulk material.

No martensite could be observed in this work. This could be attributed to the thick, and sometimes wedge shaped, morphology of the interface, as the only distinguishable contrast was visible in STEM mode. The SEM images showed a lath-like structure, much like that of martensite, towards what appeared to be the clad side of the interface. It should be noted that the interface region is highly complex, making it difficult to accurately distinguish the clad side from the BM side, so that the exact location of this lath-like morphology cannot be determined. Previous work [68] has shown that there exists a transition zone between the clad and BM in samples without a Ni-interlayer, due to migration of alloying elements. This may result in a high-alloy, high C-steel region, in which martensite may form. Another possibility is of course, that the interface does not contain any martensite, which is addressed below. However, the thick, and sometimes wedge shaped, interface could indicate that there is a different phase present here. This would have to be further investigated.

The presence of martensite is highly dependent on chemistry. The low alloyed BM will facilitate martensite formation at a significantly higher temperatures than the more highly alloyed clad. The migration of alloying elements across the interface results in a compositional gradient across the interface, in which the martensite start temperature, M_s, will vary across. Additionally, carbon migration complicates the situation, as the presence of carbon will suppress the M_s-temperature. However, excessive amounts of carbon will lead to carbide precipitation, in this case Cr-rich carbides. This precipitation depletes the surrounding matrix of chromium, which in turn raises the M_s-temperature, and thus facilitating martensite formation upon cooling. As this indicates, the chemistry and microstructure of the interface region is highly complex, making it difficult to predict which constituents will be present. Shushan et al. [28] investigated diffusion bonded carbon steel – stainless steel joints, and found that diffusion of Cr and Ni from the stainless steel to the carbon steel resulted in a thin layer of martensite at the interface, towards the carbon steel side. The thickness of the martensite layer decreased with decreasing carbon content of the steel.

It is possible that the specimens investigated here does not contain regions in which the chemistry facilitates martensite formation. However, numerous studies have reported martensite at steel – stainless steel dissimilar interfaces. Regarding dissimilar interfaces between austenitic stainless steel and carbon steel, martensite is often observed at the interface [16, 35, 36], mainly for welded joints and materials with higher carbon contents. During fusion welding, melting and solidification may result in significant dilution of the BM, rendering martensite formation possible. However, martensite formation at the dissimilar interface is also observed for hot rolled clad components [28, 34], though typically in samples with higher carbon content. Additionally, investigations [23, 59, 60] performed on steel – Ni-alloy dissimilar weldments also reveal martensite formation and carbide precipitation at the interface. It should be noted that Ni claddings are often preferred to austenitic stainless steels due to less martensite formation. Although this represents a different material system, a lot of the metallurgical mechanisms are similar for Ni - steel and austenitic stainless steel - steel systems, so that it is deemed relevant to this discussion.

From this work, there is no clear evidence of martensite at the dissimilar interface. However, a martensite-like structure was observed at the interface in SEM. Whether this is actually the case would have to be further investigated, as the difficulties in obtaining proper TEM samples limited the investigation. Nevertheless, the material combination and heat treatment of the investigated samples, in addition to the abovementioned literature, strongly indicates that BCC martensite could be present at the dissimilar interface.

6.1.2. Carbide Precipitation

Electron diffraction patterns and EDS mapping showed the presence of $Cr_{23}C_6$ at grain boundaries and inside grains close to the interface. Dislocations were also observed near the carbides, which correlates with the fact that carbides tend to precipitate on dislocations.[24] As seen in EDS mapping of the carbides, no accumulation of carbon was observed for either of the maps, see Figure 40. It should therefore be noted that carbon is a very light element, making it difficult to obtain an accurate analysis. The diffraction patterns, however, confirm the presence of $M_{23}C_6$ carbides, as the lattice parameter of the carbides were three times that of the austenite lattice.[24] In combination with the EDS maps, showing Cr accumulation and Fe depletion at the location of the carbides, it can safely be concluded that the precipitates observed are in fact $Cr_{23}C_6$ carbides.

Further into the clad (~130 μm), no carbides were observed. From LOM investigations performed in previous work, grain boundary carbide precipitation was observed approximately 200-250 μm into the clad region, see Figure 19 and Figure 20. The fact that no carbides were observed in the TEM specimens at a distance 130 μm from the interface could be attributed to the fact that the areas investigated did not contain any grain boundaries, as the areas investigated in TEM are quite small, and the austenite grains large. It is also a possibility that what appeared to be grain boundary carbides in the LOM images were in fact not carbides, but rather an effect of the etching process. This is however unlikely, as heat treatment of clad products is known to result in carbide precipitation in the clad in the absence of a Ni-interlayer.[21, 28] Carbides are typically observed near the interface on the stainless steel side, and on grain boundaries further into the bulk material.[36, 77] The hot rolling process and subsequent quenching and tempering, resulting in a carbon accumulation in the clad, also points to there being grain boundary carbides further into the clad as well. This is commented on below.

The clad stainless steel does not stabilizing elements such as Ti or Nb, which would imply that carbide precipitation is theoretically possible. On the other hand, the carbon content is quite low (< 0.03 wt%), which in turn indicated that there is low risk of carbide precipitation. However, the increased carbon content in the clad immediately adjacent to the interface, presented in Chapter 3.2, could render carbide precipitation possible if the exposure to elevated temperatures is sufficiently long. As the pipes are quenched and tempered, it is highly likely that carbide precipitation has occurred during the tempering stage.

The carbides observed in this work as small and finely dispersed throughout the clad region immediately adjacent to the interface, and appeared to be a genuine feature of the interface region. It is possible that this corresponds to the brown tinted region observed in optical micrographs performed in previous work, see Figure 20.

6.2. Fracture Toughness

6.2.1. Effect of Material and Environment

Sample A (Ni interlayer) showed fairly consistent values of maximum load and CTOD for testing in both environments, although there were some variations. An increase in maximum load and thus an increase in CTOD was observed for sample A4. However, this increase was quite small (3 % increase in maximum load and CTOD). The other specimen tested under CP, A5, showed a slight decrease in maximum load (1 %), but a significantly larger reduction in CTOD (17 %) compared to sample A4. This could be attributed to variations in specimen geometry measurements, but could also reveal potential shortcomings of the correlations used to obtain the CMOD/CTOD values from the measured displacement. Most importantly, in this ductile region, small changes in load may result in large variations in CMOD values, which could explain the variations in CTOD relative to the change in load. Nevertheless, as the use of clip gages was impossible for testing under CP, the use of load-CMOD-displacement correlations was deemed the most viable option. It should also be noted that the main goal of the investigations was to compare the different material and environment combinations, rather than determine the actual fracture toughness.

From the micrographs of the crack path, it is evident that the crack has propagated along the BM-Ni interface region, slightly into the Ni-interlayer, for both test environments. This would explain why the maximum load and CTOD values showed relatively little variation with respect to environment, as nickel has an austenitic structure with high solubility of hydrogen and thus low susceptibility to HISC. The fractographs showed a dimpled appearance for testing in air, indicating ductile fracture. For testing under CP, the initial part of the crack propagates into the BM, where a cleavage-like appearance was observed, indicating that hydrogen has had an effect on the BM. Further into the crack path, the fracture surface is dimpled, indicating ductile fracture in the Ni-interlayer, which is confirmed by the light optical micrographs. Overall, the fracture surface appearance and fracture toughness values obtained indicate that the effect of hydrogen is minimal for sample A. Had the crack propagated consistently in the ferritic BM, a more significant reduction in maximum load and CTOD would be expected.

Sample B showed a significant decrease in maximum load and CTOD for testing under CP compared to testing in air. An average reduction in maximum load of 12-13 % and 77 % for CTOD values, indicates a strong influence of hydrogen. The crack propagated mainly along the BM-clad dissimilar interface, and partly into the BM region. This corresponds well with the decrease in maximum load and fracture toughness, as the pre-charging and test conditions only would allow for a ferritic BCC material to be influenced, due to the low solubility of hydrogen and high diffusivity compared to the FCC clad. One could ask why the crack alternates between propagating in the BM and along the interface. This could be attributed to the BM being embrittled and the interface representing a vulnerable region due to complex microstructures and carbide precipitation, so that the two vulnerable zones “compete” with respect to crack propagation. This would have to be further investigated. The fracture surfaces in air was initially flat, followed by dimples, indicating ductile fracture. The flat fracture surface could be indicative of fracture along an interface, however, the light optical micrographs show that the initial part of the crack propagates in the BM. This is most likely ductile tearing from the initial blunting of the crack tip. For samples tested under CP, the fracture surface indicated initial failure by cleavage followed by a quasi-cleavage appearance, again indicating an effect of hydrogen. There is little difference in the crack path for testing in air and under CP; the crack propagated along the interface and slightly into the BM for both environments.

Regarding the fracture surface appearance, the two samples differed somewhat. Sample A showed a highly dimpled morphology when tested in air, whereas sample B showed less distinct dimple formation. This could be attributed to the crack propagating in the Ni-interlayer for sample A, and in the BM for sample B. For both samples tested under CP, the crack initiated in the BM. The appearance of these fracture surfaces are similar for both samples, strongly indicating that the remainder of the crack has propagated in the

Ni-interlayer for sample A and in the BM for sample B, which is confirmed by the light optical micrographs.

Regarding the two different material and environment combinations, it appears as though they can be categorized into three populations from the load-V_p curves. The populations are ranked according to fracture resistance in the following manner:

Sample B *(air)* > ***Sample A*** *(air, CP)* > ***Sample B*** *(CP)*

Specimens with no Ni-interlayer tested in air, sample B, showed the highest CTOD values, followed by specimens with a Ni-interlayer, sample A, tested in air and under CP. The lowest CTOD values were obtained from the samples without the Ni-interlayer, sample B, tested under CP. These somewhat surprising differences could be attributed to variation in mechanical properties between the different materials, since the crack propagated mainly in the BM for sample B, and in the Ni-interlayer for sample A.

Accurate information regarding the mechanical properties and chemistry of the Ni-interlayer has not been obtained, but electroplated nickel is typically quite pure (> 99 wt%) [78], and steels and stainless steels generally have higher strength than nickel, which will yield at lower loads. This could explain why sample B (no Ni-interlayer) tested in air results in higher maximum load and fracture toughness than sample A (Ni-interlayer). For testing under CP, however, the ferritic BM appears to suffer embrittlement by hydrogen, resulting in a reduction in maximum load and fracture toughness for samples without a Ni-interlayer. For samples with a Ni-interlayer, the fracture initiated in the BM, which showed a brittle fracture surface indicating embrittlement by hydrogen, followed by propagation in the austenitic Ni-interlayer, which showed a dimpled fracture surface, indicating ductile failure. No significant reduction of maximum load or fracture toughness was observed for testing under CP for the samples with the Ni-interlayer, due to the high solubility of hydrogen in the FCC lattice.

It should also be noted that the two samples consisted of two different BM steels (X65 for sample A, X60 for sample B), so that there is a slight difference in tensile and yield strength. This could explain why sample A, which has the highest tensile strength, shows a slightly higher maximum load than sample B. Additionally, the pipes are delivered by two different suppliers, which may have influenced the microstructure and properties. The presence of the Ni-interlayer will also influence the chemistry and microstructure across the interface region, as seen in previous work.[68] For samples without a Ni-interlayer, there will be a transition zone, as some of the main alloying elements (Cr, Ni) may migrate from the clad to the BM, mainly during production, which may influence the mechanical properties of the interface region.

As mentioned above, the crack propagated in either the Ni-interlayer, or on the BM side, immediately adjacent to the interface. For all cases, there was no cracking on the clad side of the interface, so that the previously assumed crack susceptible microstructure in the clad immediately adjacent to the interface, was not so crack susceptible after all, at least under this type of loading and conditions. This is addressed in the following section.

6.2.2. Correlations with Previous Work

As this thesis is a continuation of a project work, it is natural to discuss the correlation between the two. In the preceding work, cracks were observed in the clad immediately adjacent to the interface, propagating along austenite grain boundaries. This region showed high hardness values, carbon accumulation and carbide precipitation, both in the welded and un-welded condition. The cracks were only observed in welded specimens close to the weld metal, indicating that thermal stresses from the welding procedure has influenced the cracking. In this thesis, investigations were performed on pipes in the unwelded condition, and showed that cracking occurred on the BM side of the interface, i.e. the opposite of what was observed in the preceding work. Although the specimens investigated here are not welded, and it is likely that thermal stresses from welding has influenced the cracking in the clad, this region is nevertheless deemed vulnerable due to carbon accumulation, carbide precipitation and high local hardness. It is therefore interesting that the crack propagation in the fracture mechanical tests occurred on the BM side of the interface, rather than in the embrittled clad region. However, it should be noted that the welded samples have experienced a double tempering from production and the welding process, as opposed to the unwelded specimens. This could influence carbon diffusion and carbide precipitation, in addition to introducing residual stresses.

After exposure to elevated temperatures, i.e. hot rolling and welding, residual stresses resulting from the difference in coefficient of thermal expansion (CTE) between the clad and BM can result in tensile stresses at the dissimilar interface, as the clad will expand more than the BM, and thus experience constraint from the BM upon cooling. Additionally, shear stresses may also be present at the dissimilar interface, again attributed to the difference in CTE. In samples with a Ni-interlayer, no cracks were observed in the welded specimens. This is mainly attributed to the fact that the Ni-interlayer results in much more sluggish diffusion of carbon into the clad, thus eliminating carbon accumulation, excessive carbide precipitation and high local hardness levels. Additionally, the difference in CTE between ferritic steel and austenitic stainless steel is greater than the difference between ferritic steel and Ni-based alloys, meaning that the Ni-interlayer could work as a transition region between the clad and BM with respect to CTE, resulting in a lower level of residual stresses. This would have to be further investigated.

As mentioned above, the fracture did not propagate into the clad region for either of the samples tested in this work, although this was what was expected from the results of the preceding work. In this work, the samples are subjected to tensile loading, and additionally does not contain a heat affected zone (HAZ), as opposed to the previously investigated welded samples. This raises the question of whether shear stresses due to difference in CTE is the driving force behind crack propagation in the hardened region in the clad in the previously investigated welded specimens. It could also appear that Ni is beneficial under shear, stress, but not so much under direct tensile loading, where the crack propagates slightly into the Ni-interlayer. Also, due to the different mechanical properties between the Ni-interlayer and surrounding clad and BM, the Ni-region will represent a soft zone, preferable for crack propagation. This could also explain why the samples with the Ni-interlayer showed lower CTOD values than the samples without the Ni-interlayer when tested in air.

For the samples without a Ni-interlayer, in which fracture occurred along the interface and slightly into the BM, it should be noted that the BM region is decarburized, which could explain why the fracture occurred here. In fact, in the work preceding this thesis [68], a dip in hardness was observed at the BM immediately adjacent to the interface. Additionally, in samples with a Ni-interlayer, the lowest hardness values were observed in the Ni-interlayer (165 HV0.025).

Shushan et al. [28] investigated the interface between diffusion bonded austenitic stainless steel to low alloy steel. Tensile testing in air at room temperature showed that failure occurred in the decarburized region of the steel, away from the interface. Although the specimens in the work of Shushan et al. was diffusion bonded, as opposed to bonding by hot rolling, a lot of the same characteristics were observed, such as a decarburized region in the steel, precipitation of Cr carbides in the stainless steel close to the interface and high local hardness values in the carbide rich region. Additionally, a thin band of martensite was observed at the interface towards the low alloy steel side.

Additionally, machining of the CT specimens investigated in this work by electro-discharge machining (EDM) may have relieved the residual stresses in the clad adjacent to the interface, thus rendering the BM side immediately adjacent to the interface and/or Ni-interlayer the path of least resistance for crack propagation. The influence of EDM on the residual stresses would have to be further investigated.

6.2.3. Influence of Test Parameters and Specimen Size and Geometry

The specimen size and geometry was designed to be in accordance with BS 7448-1[71], except for the presence of a fatigue pre-crack. This is addressed below. Post-testing measurements also confirmed that the specimens were within the specifications given in the abovementioned standard, see Appendix A. It should be noted that the measurements of the initial crack length a_0 after testing was only performed at 5 locations, rather than the specified 9. As the crack was machined, rather than pre-cracked, the length will be much more uniform, thus limiting the need for extensive mapping of the initial crack length. Additionally, the small size of the specimens, and the fact that the goal was to compare fracture toughness, rather than assess it, deemed this acceptable. The 5 measurements of the initial crack were fairly consistent for all cases, indicating that this was a suitable approach.

The loading rate was based on stress intensity rate, rather than machine displacement rate. As the sample size is small relative to the test setup, the initial loading will yield a somewhat unreliable displacement rate, as the components and loading pins settle in. Additionally, it was difficult to obtain literature regarding the loading rate for compact tension (CT) specimens under hydrogen charging, as most of the relevant work involved single-edge bend specimens, which differ in geometry, rendering them incomparable. The use of stress intensity rate to determine the loading rate was therefore deemed more appropriate. The stress intensity rate was based on previous work [73] investigating the effect of hydrogen, meaning that the selected stress intensity rate should produce a suitable loading rate for testing under CP. As can be seen for the samples without a Ni-interlayer, the presence of hydrogen noticeably lowered the maximum load and CTOD, indicating that the loading rate was sufficiently small to allow for adequate hydrogen diffusion. For the samples containing the Ni-interlayer, the crack appears to propagate slightly into the Ni-interlayer close to the clad, which has a high solubility of hydrogen, thus requiring significantly higher hydrogen concentrations in order to suffer embrittlement. For testing under CP, the initial part of the crack propagated in the BM, which showed a brittle fracture surface, indicative of embrittlement of the BM by hydrogen. The applied pre-charging time is also deemed sufficient, as previous work [58, 59] involving investigations of significantly larger specimens only preformed 48 hours of pre-charging.

For fracture toughness testing, the manufactured pre-crack should ideally be as sharp as possible, in order to represent the true properties of the material tested. A sharp crack is more critical than a blunt crack, which will result in more conservative fracture toughness values. In experiments performed by Milititsky et al. [58], samples that were fatigue pre-cracked showed lower fracture toughness values than samples that contained a crack produced by EDM. The area of investigation in this work, i.e. the dissimilar interface, deemed the use of fatigue pre-cracking unsuitable. As the dissimilar interface was the desired region of interest, introducing a fatigue pre-crack which propagated *exactly* along this interface would not be feasible. For this reason, the samples were notched by EDM rather than fatigue pre-cracked. There have been performed small-scale fracture mechanical investigations [59, 60] of dissimilar interfaces, where the use of a machined notch has been used, for the exact same reasons. Additionally, as the goal of these investigations was to study the effect of CP with respect to the dissimilar interface, rather than determine the exact fracture toughness, the use of a notched crack was deemed suitable. Nevertheless, it should be noted that the fracture toughness values obtained in this work are not absolute, and may be on the less conservative side, compared to standardized fracture toughness tests using fatigue pre-cracked specimens.

Another aspect which may influence the test results is the specimen size and geometry. For ductile materials, like those tested in this work, a maximum load plateau is typically obtained. Upon reaching the maximum load, there is no significant change in the load-displacement curve, except a reduction in loading rate as the crack propagates and the sample cross section is reduced. For these samples, the CTOD at maximum load is typically reported. However, this value is very dependent on specimen size, and thus only provides an indication of the fracture toughness.[49] Additionally, fracture toughness specimens should have a thickness corresponding to the full through-thickness of the material to be tested. [71] In this work, this was not feasible. As the dissimilar interface was the region to be investigated, the thickness of the clad layer (~ 3 mm) determined the dimensions of the CT specimen. The fracture toughness values obtained in this work are therefore not absolute, but gives an indication of the fracture toughness, which is utilized for comparison of the different material and environment combinations.

Additionally, the method used to obtain the fracture toughness values should be mentioned. The CMOD and CTOD values were calculated based on the correlation between load-CMOD and load-displacement for specimens tested in air, as clip gages could not be used under CP testing. As this indicates, the calculated, or rather estimated, CMOD and CTOD values may not represent the true properties of the material, but rather give an indication of the approximate fracture toughness. The curves used to obtain the correlation was, however, quite consistent, and was deemed the most accurate and suitable approach for these experiments.

Finally, it should be noted that only 4 tests were performed in this work due to time limitations. Ideally, a higher number of tests should have been performed in order to obtain a more representative selection of results. Nevertheless, the results obtained are consistent, which renders comparison possible.

Ideally, the aforementioned previous work performed by Fenske and Dodge [58-60] would be used as a ground for comparison of fracture toughness. However, the fracture toughness data is either not available, i.e. presented in a closed report, or presented in the form of crack growth resistance curves, which is not available for the results in this work. Additionally, the referenced investigations have focused mainly on the crack path and morphology with respect to the presence of hydrogen and/or post-weld heat treatment (PWHT). Generally, the fracture toughness, or resistance to crack growth is significantly reduced in the presence of hydrogen, and excessive PWHT, the latter being attributed to carbide precipitation in the planar solidification region. Although a direct comparison is not feasible, the reduction in fracture toughness of dissimilar alloys in the presence of hydrogen corresponds well with the observations made in this work.

6.3. Summary

This thesis has investigated both the metallurgical and mechanical aspects of the dissimilar interface in clad pipes. As this discussion illustrates, the material system of clad pipes is quite complex. This section will try to provide a brief summary of the most relevant part of the discussion.

TEM investigations showed the presence of $Cr_{23}C_6$ in the clad immediately adjacent to the interface, both inside grains and at grain boundaries. The carbides were small and finely dispersed. Diffraction patterns and EDS mapping was used to characterize the carbides. Further into the clad no carbides were observed, despite strong indications that there should be grain boundary precipitates in this region. As the austenite grains are quite large, it could be attributed to the fact that no grain boundaries were encountered in this work, so that more samples should be investigated in order to ensure a more representative result.

The dissimilar interface region was thick, and sometimes wedge shaped, thus giving poor contrast in TEM microscopy mode. In STEM mode, the interface was found to have a jagged distribution of Ni towards the clad side, and segregation of Cr to carbides. Diffraction patterns showed a BCC structure on the BM side immediately adjacent to the interface, but the poor contrast made it impossible to assess the presence of low carbon BCC martensite. However, SEM images and the evaluated literature in combination with the material system and applied heat treatment, indicates that there may be martensite present at the interface. Further investigations of the dissimilar interface depends on providing samples that are sufficiently thin at the interface region. A different approach to the sample preparation should thus be the focus of any further work regarding the dissimilar interface.

Slow strain rate (SSR) testing was performed on miniature CT specimens to evaluate the effect of material and environment on the fracture toughness of the dissimilar interface. In samples with a Ni-interlayer, the crack propagated slightly into the Ni-interlayer, close to the BM, whereas samples with no Ni-interlayer had crack propagation alternating between the BM and the dissimilar interface when tested in air. The presence of hydrogen from simulated CP in seawater showed no significant change in crack path for samples without a Ni-interlayer. For samples with a Ni-interlayer however, the crack initiated in the BM for testing under CP, only to propagate slightly into the Ni-interlayer, i.e. the same as for testing in air. The samples with the Ni-interlayer showed no significant change in maximum load and CTOD when tested under CP, whereas the samples without a Ni-interlayer showed a significant reduction of said values when tested under CP. This resulted in three different material-environment populations, and is ascribed to the crack propagating in the austenitic Ni-interlayer for sample A, and in the ferritic BM for sample B.

For all samples, no part of the crack propagated into the previously suspected crack susceptible region found in the HAZ of the clad in welded samples. The samples investigated in this work are not welded, and does not contain a HAZ, which may introduce residual shear and tensile stresses. Additionally, the SSR tests involves tensile loading, which could indicate that Ni is beneficial under shear loading, but not so much under direct tensile loading, in which it will present itself as a soft zone where the crack will propagate. The BM adjacent to the interface also represents a softer zone compared to the bulk clad and BM, due to decarburization during production.

Regarding the validity of the test results, some remarks must be made. The CMOD could not be measured during CP testing, so that a correlation between load-displacement and load-CMOD from testing in air was established in order to calculate the CTOD for testing under CP. This, in combination with the use of a machined notch, rather than fatigue pre-cracking, and the fact that the dimensions of the specimens do not represent the full thickness of the pipe, shows that the fracture toughness values cannot be taken as absolute, but used rather as a ground for comparison. Additionally, testing of more samples would have provided a more representative selection of results, however the results obtained were consistent, deeming comparison possible.

7. Conclusions

In the present master's thesis, the dissimilar interface between clad pipes has been investigated. Samples with and without a Ni-interlayer between the clad and base metal (BM) have been investigated. Transmission electron microscopy (TEM) has been performed to characterize the dissimilar interface region and carbides in the clad adjacent to the interface. Scanning electron microscopy (SEM) has been performed to assess the appearance and size of the dissimilar interface region. Slow strain rate (SSR) tensile testing was performed on miniature compact tension (CT) specimens in air and under cathodic protection (CP) to evaluate the fracture mechanical properties of the dissimilar interface with respect to material combination and environment. The fracture surfaces and crack path was investigated using SEM and light optical microscopy (LOM). From this, the following conclusions can be drawn:

Fracture toughness

- Successful fracture mechanical testing of miniature compact tension specimens of the dissimilar interface in clad pipes has been performed.
- Samples without a Ni-interlayer tested in air showed the highest fracture toughness values, followed by samples with a Ni-interlayer tested in both air and under CP. The lowest fracture toughness values were obtained for samples without a Ni-interlayer tested under CP.
- For samples with a Ni-interlayer, the CTOD was 0.116 mm in air and 0.108 mm under cathodic protection (CP), corresponding to a reduction of 7 %.
- For samples without a Ni-interlayer, the CTOD was 0.195 mm in air and 0.045 mm under CP, corresponding to a reduction of 77 %.
- Samples with a Ni-interlayer failed slightly into the Ni-interlayer, close to the base metal (BM) when tested in air. In the presence of hydrogen, fracture initiated in the base metal, followed by propagation in the Ni-interlayer.
- Samples without a Ni-interlayer failed in the base metal (BM) immediately adjacent to the interface, and along the dissimilar interface for testing in both environments.

Dissimilar interface characteristics

- The clad immediately adjacent to the dissimilar interface consisted of small, finely dispersed $Cr_{23}C_6$ carbides, both inside grains and on grain boundaries.
- The dissimilar interface had a lath-like structure, however there was no clear evidence of martensite.
- The dissimilar interface showed a jagged distribution of Ni towards the clad, and segregation of Cr to carbides.

8. Further Work

This work has investigated the dissimilar interface of clad pipes with respect to microstructure and fracture toughness. The exact mechanisms behind cracking in the clad of welded samples are still unknown. Additionally, the dissimilar interface has not been thoroughly characterized. Based on the findings in this report, the following work should be performed.

- Physical weld simulations on miniature compact tension specimens in order to introduce a heat affected zone (HAZ) to assess the influence of welding with respect to the interface microstructures under fracture mechanical testing.
- Numerical weld simulations to assess residual stresses after welding.
- A crack free area from the girth weld of a pipe should be investigated in order to compare the microstructure and properties of areas containing cracks, and areas without cracks, to determine the driving force behind the cracking in the hardened region in the clad.
- Additional slow strain rate (SSR) testing under CP should be performed to obtain a more representative selection of results, in order to utilize the results for modelling.
- If the dissimilar interface is to be further investigated, a more suitable sample preparation for TEM should be established, as the sample preparation used in this work did not provide sufficiently thin specimens to investigate the interface region properly. Extraction of samples should be performed by a focused ion beam (FIB) method. The work of Fenske [59] is recommended as a guide.
- Nanoindentation should be performed in the interface region suspected to contain martensite.

References

1. Norwegian Petroleum Directorate, *Facts 2014 - The Norwegian Petroleum Sector*, Y. Tormodsgard, Editor. 2014.
2. Kloewer, J., R. Behrens, and J. Lettner, *Clad Plates and Pipes in Oil and Gas Production: Applications - Fabrication - Welding*. NACE International.
3. Hval, M., T. Lamvik, and R. Hoff, *Engineering Critical Assessment of Clad Pipeline Installed by S-lay for the Operation Phase.* Procedia Materials Science, 2014. **3**(0): p. 1216-1225.
4. Smith, L. and M. Celant, *CASTI Handbook of Cladding Technology*. Second ed. 2003.
5. Butting. *Clad Pipes – Equal to All Challenges*. [cited 2014 11.11]; Available from: http://www.butting.com/en/clad-pipes/.
6. SINTEF. *ROP, Knowledge Basis for Repair Contingency of Pipelines*. 2014 [cited 2014 11.11]; Available from: http://www.sintef.no/home/SINTEF-Materials-and-Chemistry/Projects1/2014/ROP-Knowledge-basis-for-repair-contingency-of-pipelines/.
7. Det Norske Veritas, *DNV-OS-F101 - Submarine Pipeline Systems*. 2012.
8. Reichel, T., et al., *Production of Metallurgically Cladded Pipes for High End Applications in the Oil & Gas Industry*, in *27th International Conference on Offshore Mechanics and Arctic Engineering (OMAE)*. 2008, ASME: Estoril, Portugal. p. 179-186.
9. Gray, J.M. and F. Siciliano, *High Strength Microalloyed Linepipe: Half a Century of Evolution*. 2009, Microalloyed Steel Institute: Houston, Texas, USA.
10. Solberg, J.K., *Teknologiske metaller og legeringer*. 2008, Institutt for materialteknologi: Norges teknisk-naturvitenskapelige universitet.
11. Bhadeshia, H.K.D.H. and S.R. Honeycombe, *3 - The Iron-Carbon Equilibrium Diagram and Plain Carbon Steels*, in *Steels (Third Edition)*, H.K.D.H.B.R. Honeycombe, Editor. 2006, Butterworth-Heinemann: Oxford. p. 39-70.
12. American Society for Metals, *Metallography and Microstructures, ASM Handbook*. Vol. 9. 2005.
13. Bhadeshia, H.K.D.H. and S.R. Honeycombe, *13 - Weld Microstructures*, in *Steels (Third Edition)*, H.K.D.H.B.R. Honeycombe, Editor. 2006, Butterworth-Heinemann: Oxford. p. 287-306.
14. Kou, S., *Post-Solidification Phase Transformations*, in *Welding Metallurgy*. 2003, John Wiley & Sons, Inc. p. 216-242.
15. Bhadeshia, H.K.D.H. and S.R. Honeycombe, *Stainless Steel*, in *Steels (Third Edition)*, H.K.D.H.B.R. Honeycombe, Editor. 2006, Butterworth-Heinemann: Oxford. p. 259-286.
16. DuPont, J.N., J.C. Lippold, and S.D. Kiser, *Dissimilar Welding*, in *Welding Metallurgy and Weldability of Nickel-Base Alloys*. 2009, John Wiley & Sons, Inc. p. 327-378.
17. Askeland, D.R., P.P. Fulay, and W.J. Wright, *Atom and Ion Movements in Materials*, in *The Science and Engineering of Materials*, H. Gowans, Editor. 2010, Cengage Learning.
18. Lundin, C.D., *Dissimilar Metal Welds - Transition Joints Literature Review.* Welding Research Supplement, 1982.

19. Easterling, K., *Cracking and Fracture in Welds*, in *Introduction to the Physical Metallurgy of Welding*. 1983, Butterworths.
20. Japan Steel Works. *Function of Nickel Plating*. [cited 2014 15.11]; Available from: http://www.jsw.co.jp/en/products/clad/function_of_nickel_plating.html.
21. Smith, L., *Engineering with Clad Steel*, in *Nickel Institute Technical Series No 10 064*. 2012: Nickel Institute.
22. Azar, A.S., *Characterization of Clad Pipelines, SINTEF Report A26507*. 2014.
23. Olden, V., et al. *The Effect of PWHT on the Material Properties and Microstructure in Inconel 625 and Inconel 725 Buttered Joints*. in *22nd International Conference on Offshore Mechanics and Arctic Engineering*. 2003. Cancun, Mexico.
24. Marshall, P., *Martensitic Transformations and the Effect of Ageing on the Microstructure of Austenitic Stainless Steels*, in *Austenitic Stainless Steels - Microstructure and Mechanical Properties*. 1984, Elsevier Applied Science Publishers LTD: Ripple Road, Barking, Essex England.
25. Terao, N. and B. Sasmal, *Precipitation of M23C6 Type Carbide on Twin Boundaries in Austenitic Stainless Steels.* Metallography, 1980. **13**(2): p. 117-133.
26. Singhal, L.K. and J.W. Martin, *The Nucleation and Growth of Widmannstätten M23C6 Precipitation in an Austenitic Stainless Steel.* Acta Metallurgica, 1968. **16**(9): p. 1159-1165.
27. Lo, K.H., C.H. Shek, and J.K.L. Lai, *Recent Developments in Stainless Steels.* Materials Science and Engineering: R: Reports, 2009. **65**(4–6): p. 39-104.
28. Shushan, S.M., E.A. Charles, and J. Congleton, *The Environment Assisted Cracking of Diffusion Bonded Stainless to Carbon Steel Joints in an Aqueous Chloride Solution.* Corrosion Science, 1996. **38**(5): p. 673-686.
29. McGuire, M., *Austenitic Stainless Steels*, in *Stainless steels for design engineers*. 2008, ASM International.
30. Bhadeshia, H.K.D.H. and S.R. Honeycombe, *5 - Formation of Martensite*, in *Steels (Third Edition)*, H.K.D.H.B.R. Honeycombe, Editor. 2006, Butterworth-Heinemann: Oxford. p. 95-128.
31. N. Solomon and I. Solomon, *Deformation Induced Martensite in AISI 316 Stainless Steel.* Revista de metalurgia, 2010. **46**(2): p. 121-128.
32. Sherby, O.D., et al., *Revisiting the Structure of Martensite in Iron-Carbon Steels.* Materials Transactions, 2008. **49**(9): p. 2016-2027.
33. Dawood, M.A., et al., *Thermal Aging of 16Cr–5Ni–1Mo Stainless Steel: Part 1 – Microstructural Analysis.* Materials Science and Technology 2004. **20**(3): p. 363-369.
34. Xie, G., et al., *Interface Characteristic and Properties of Stainless Steel/HSLA Steel Clad Plate by Vacuum Rolling Cladding.* Materials Transactions, 2011. **52**(8): p. 4.
35. DuPont, J.N. and C.S. Kusko, *Technical Note: Martensite Formation in Austenitic/Ferritic Dissimilar Alloy Welds.* Welding Research, 2007. **86**(2).
36. Gittos, M.F. and T.G. Gooch, *The Interface below Stainless Steel and Nickel-alloy Claddings.* Welding Research Supplement, 1992.
37. Hänninen, H., et al., *VTT RESEARCH NOTES 2347: Dissimilar Metal Weld Joints and Their Performance in Nuclear Power Plant and Oil Refinery Conditions*. 2006: VTT Technical Research Centre of Finland.

38. Reichel, T., V. Pavlyk, and T. Loose, *Throughout Simulation of Manufacturing of Longitudinally Welded Steel Pipe with SYSWELD*, in *SYSWELD Forum*. 2009.
39. Anderson, T.L., *Linear Elastic Fracture Mechanics*, in *Fracture Mechanics: Fundamentals and Applications*. 2005, Taylor & Francis: Boca Raton, Fla. p. 621 s. : ill.
40. Askeland, D.R., P.P. Fulay, and W.J. Wright, *Mechanical Properties: Part Two*, in *The Science and Engineering of Materials*, H. Gowans, Editor. 2010, Cengage Learning.
41. Anderson, T.L., *Elastic-Plastic Fracture Mechanics*, in *Fracture Mechanics: Fundamentals and Applications*. 2005, Taylor & Francis: Boca Raton, Fla. p. 621 s. : ill.
42. Anderson, T.L., *Fracture Mechanisms in Metals*, in *Fracture Mechanics: Fundamentals and Applications*. 2005, Taylor & Francis: Boca Raton, Fla. p. 621 s. : ill.
43. Halahan, R. *MSE 2094: Analytic Methods in Materials Engineering - Modes of Fracture*. 1997 [cited 2015 21.05.]; Available from: http://www.sv.vt.edu/classes/MSE2094_NoteBook/97ClassProj/exper/halahan/www/halahan.html.
44. Nibur, K.A., et al., *SAND2010-4633: Measurement and Interpretation of Threshold Stress Intensity Factors for Steels in High-Pressure Hydrogen Gas*. 2010: Sandia National Laboratories.
45. Warnes, W.H. *ENGR322: Homework Set Seven*. 2012 [cited 2015 15.04]; Available from: http://oregonstate.edu/instruct/engr322/Homework/AllHomework/S12/ENGR322HW7.html.
46. Houston Electron Microscopy. *Fracture*. [cited 2015 01.05]; Available from: http://www.houstonem.com/gallery/fractures/.
47. Engineering, S.o.M.S.a. *Failure analysis - Industrial case studies: Part 4 - Characteristics of Fast Fracture in Metals*. [cited 2015 21.05.]; Available from: http://www.tech.plymouth.ac.uk/sme/interactive_resources/tutorials/FailureAnalysis/Fractography/Fractography_Resource4.htm.
48. Callister, W.D., *Failure*, in *Fundamentals of Materials Science and Engineering*, W. Anderson, Editor. 2001, John Wiley & Sons, Inc.: Department of Metallurgical Engineering, The University of Utah.
49. Anderson, T.L., *Fracture Toughness Testing of Metals*, in *Fracture Mechanics: Fundamentals and Applications*. 2005, Taylor & Francis: Boca Raton, Fla. p. 621 s. : ill.
50. Olden, V., *FE Modelling of Hydrogen Induced Stress Cracking in 25% Cr Duplex Stainless Steel*, in *Department of Engineering Design and Materials*. 2008, Norwegian University of Science and Technology: Faculty of Engineering Science and Technology.
51. Callister, W.D., *Corrosion and Degradation of Materials*, in *Fundamentals of Materials Science and Engineering*, W. Anderson, Editor. 2001, John Wiley & Sons, Inc.: Department of Metallurgical Engineering, The University of Utah.
52. Billingham, J., et al., *Research report 105 - Review of the Performance of High Strength Steels Used Offshore* 2003, School of Industrial and Manufacturing Science: Cranfield University.

53. Lynch, S., *Hydrogen Embrittlement Phenomena and Mechanisms*. 2012. p. 105.
54. Anderson, T.L., *Environmentally Assisted Cracking in Metals*, in *Fracture Mechanics: Fundamentals and Applications*. 2005, Taylor & Francis: Boca Raton, Fla. p. 621 s. : ill.
55. Olden, V., C. Thaulow, and R. Johnsen, *Modelling of Hydrogen Diffusion and Hydrogen Induced Cracking in Supermartensitic and Duplex Stainless Steels.* Materials & Design, 2008. **29**(10): p. 1934-1948.
56. Johnsen, R., B. Nyhus, and S. Wästberg. *OMAE2009-79325: Hydrogen Induced Stress Cracking (HISC) of Stainless Steels under Cathodic Protection in Seawater - Presentation of a New Test Method*. in *ASME 2009 28th International Conference on Ocean, Offshore and Arctic Engineering*. 2009. Honolulu, Hawaii, USA.
57. Herms, E., J.M. Olive, and M. Puiggali, *Hydrogen Embrittlement of 316L Type Stainless Steel.* Materials Science and Engineering: A, 1999. **272**(2): p. 279-283.
58. Milititsky, M., et al., *Assessment of Dissimilar Metal Interfaces for Sub-Sea Application under Cathodic Protection*, in *Materials Science & Technology*. 2010: Houston, Texas, USA.
59. Fenske, J.A., *Microstructure and Hydrogen Induced Failure Mechanisms in Iron-Nickel Weldments*, in *Department of Materials Science and Engineering*. 2010, University of Illinois.
60. Dodge, M.F., *The Effect of Heat Treatment on the Embrittlement of Dissimilar Welded Joints*, in *Department of Engineering*. 2014, University of Leicester.
61. Williams, D.B. and C.B. Carter, *The Transmission Electron Microscope*, in *Transmission Electron Microscopy - A Textbook for Materials Science - Part 1: Basics*. 2009, Springer.
62. Hjelen, J., *Scanning elektron-mikroskopi*. 1986, SINTEF, Avdeling for metallurgi: Metallurgisk institutt, NTH.
63. Solberg, J.K. and V. Hansen, *Innføring i transmisjon elektronmikroskopi*. 2014.
64. Reimer, L. and H. Kohl, *Transmission Electron Microscopy - Physics of Image Formation*. 2008: Springer.
65. Berntsen, Ø.U., *Investigation of Co2AlO4/CeO2 Catalyst for N2O Abatement using Electron Microscopy Techniques*, in *Department of Physics*. 2014, Norwegian University of Science and Technology.
66. Williams, D.B. and C.B. Carter, *Amplitude Contrast*, in *Transmission Electron Microscopy - A Textbook for Materials Science - Part 1: Basics*. 2009, Springer.
67. Nellist, P., *Scanning Transmission Electron Microscopy*, in *Science of Microscopy*, P. Hawkes and J.H. Spence, Editors. 2007, Springer New York. p. 65-132.
68. Bjaaland, H., *Metallurgical Reactions in Welding of Clad X60/X65 Pipelines*. 2014: Norwegian University of Science and Technology.
69. ASTM, *Standard Specification for Seamless, Welded, and Heavily Cold Worked Austenitic Stainless Steel Pipes*, in *A312/A312M*. 2014.
70. Manso-Silvan, M., et al., *Preparation of Interfaces for TEM Cross-Section Observation.* Nuclear Instruments and Methods in Physics Research Section B: Beam Interactions with Materials and Atoms, 2007. **257**(1–2): p. 623-626.
71. British Standard, *BS 7448-1: Fracture Mechanics Toughness Tests*, in *Part 1: Method for Determination of KIC, Critical CTOD and Critical J Values of Metallic Materials*. 1991.

72. Hellesvik, A., *Cladpipe Modified CT Geometry*. 2015, SINTEF.
73. Lee, Y. and R. Gangloff, *Measurement and Modeling of Hydrogen Environment–Assisted Cracking of Ultra-High-Strength Steel.* Metallurgical and Materials Transactions A, 2007. **38**(13): p. 2174-2190.
74. Det Norske Veritas, *Recommended Practice DNV-RP-B401 - Cathodic Protection Design.* 2010.
75. Olden, V., A.S. Hauge, and O.M. Akselsen, *The Influence of Plastic Strain on the Effective Hydrogen Diffusion Coefficient and Trapping in Base Metal and Weld Simulated Heat Affected Zone of an X70 Pipeline Steel*, in *The 22nd International Offshore and Polar Engineering Conference*. 2012, International Society of Offshore and Polar Engineers (ISOPE): Rhodes Greece
76. International Organization for Standardization, *ISO 12135:2002 - Metallic Materials - Unified Method of Test for the Determination of Quasistatic Fracture Toughness*, in *Technical Corrigendum 1*. 2008.
77. Bulent, K., *The Interface Morphology of Diffusion Bonded Dissimilar Stainless Steel and Medium Carbon Steel Couples.* Journal of Materials Processing Technology, 2007. **190**(1–3): p. 138-141.
78. Parkinson, R., *Properties and Applications of Electroless Nickel (10081)*. Nickel Development Institute.

Appendix A – Specimen Geometry and Dimensions

The compact tension (CT) specimen geometry is presented in Figure 58. The various dimensions measured are indicated on the specimen geometry sketch, and are presented in Table 7 on the next page. The dimensions are measured from the bottom of the specimen to the various dashed lines, except for the thickness B, which is measured over the cross section of the pipe, along the expected crack path. It should be noted that sample A1 and sample B1 were measured post testing, so that the dimensions B and W-a, and thus a, could not be obtained accurately, and were therefore not measured. The dimensions are in accordance with BS 7448-1.[71]

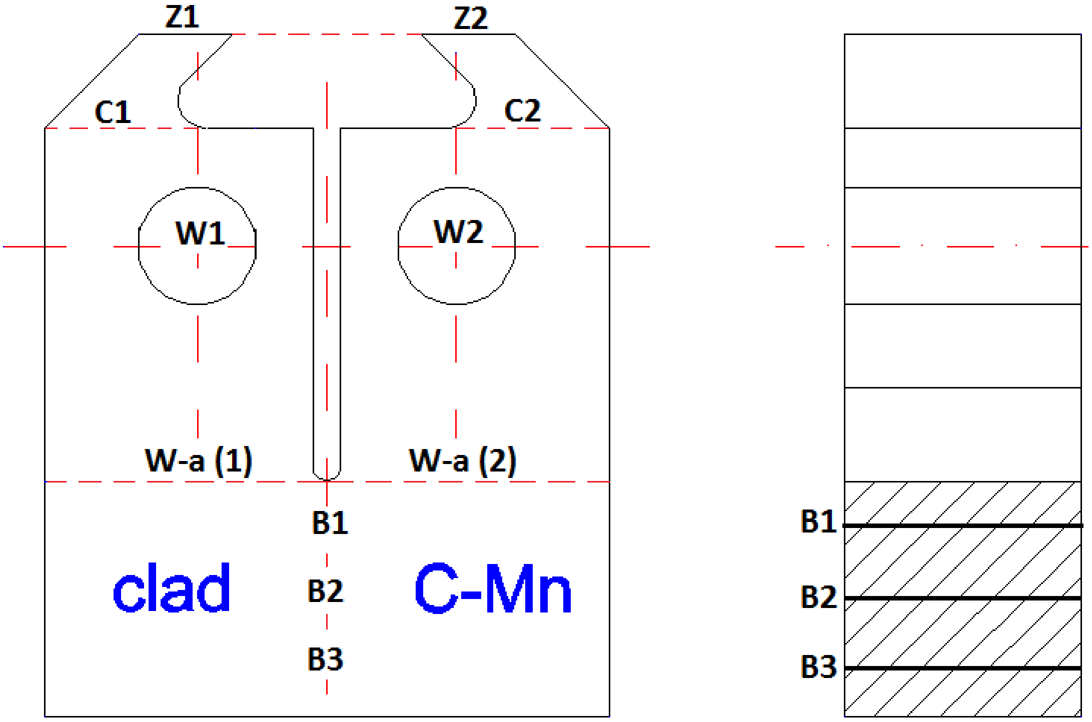

Figure 58 - Compact tension specimen geometry, W = 5 mm, B = 2.5 mm, a = 2.5 mm, C = 6.25 mm, z = 1.0 mm.[72]

Table 7 - Specimen dimensions. Sample A1 and B1 was measured after testing. B and W-a, and thus a, could not be obtained accurately and were not measured.

[mm]	**Ref.**	**A1**	**B1**	**A3**	**B3**	**A4**	**B4**	**A5**	**B5**
B_1	-	-	-	2.4960	2.4980	2.4940	2.4950	2.4920	2.4920
B_2	-	-	-	2.5010	2.4970	2.4940	2.5010	2.4930	2.4970
B_3	-	-	-	2.5000	2.4950	2.4960	2.4980	2.4940	2.4920
B	**2.5000**	**-**	**-**	**2.4990**	**2.4967**	**2.4947**	**2.4980**	**2.4940**	**2.4937**
W_1	-	4.9425	4.9750	4.9300	4.9250	4.9275	4.9200	4.9200	4.9025
W_2	-	4.9325	4.9525	4.9300	4.9300	4.8925	4.9225	4.8975	4.9125
W	**5.0000**	**4.9375**	**4.9638**	**4.9300**	**4.9275**	**4.9100**	**4.9213**	**4.9088**	**4.9075**
W-a $_{(1)}$	-	-	-	2.5100	2.4800	2.4950	2.4850	2.4950	2.4800
W-a $_{(2)}$	-	-	-	2.4900	2.4800	2.4750	2.4950	2.4900	2.500
W-a	**2.5000**	**-**	**-**	**2.5000**	**2.4800**	**2.4850**	**2.4900**	**2.4925**	**2.4900**
a	**2.500**	**-**	**-**	**2.4300**	**2.4475**	**2.4250**	**2.4313**	**2.4163**	**2.4175**
C $_{(1)}$	-	6.2400	6.2450	6.2300	6.2100	6.2350	6.2200	6.2300	6.2150
C $_{(2)}$	-	6.2300	6.2550	6.2250	6.2200	6.2250	6.2250	6.2150	6.2100
C	**6.2500**	**6.2350**	**6.2500**	**6.2275**	**6.2150**	**6.2300**	**6.2225**	**6.2225**	**6.2125**
z $_{(1)}$	-	0.9950	0.9900	0.9900	0.9950	1.0000	1.0000	0.9950	0.9900
z $_{(2)}$	-	0.9950	0.9900	0.9950	0.9800	0.9900	0.9900	0.9900	0.9900
z	**1.000**	**0.9950**	**0.9900**	**0.9925**	**0.9875**	**0.9950**	**0.9950**	**0.9925**	**0.9900**

The initial crack length a_0 was measured after testing, and the results are presented in Table 8. a_1 and a_5 correspond to the two outermost measurements. For all cases, $0.45 \leq a_0/W \leq 0.55$, is fulfilled, and the difference between any of the two crack measurements does not exceed 10% of a_0.

Table 8 - Initial crack length measurements.

[mm]	**A1**	**B1**	**A3**	**B3**	**A4**	**B4**	**A5**	**B5**
a_1	2.5063	2.4988	2.4775	2.4925	2.4300	2.4188	2.5063	2.4250
a_2	2.5013	2.4688	2.4825	2.4925	2.4500	2.4138	2.5563	2.4400
a_3	2.5113	2.5088	2.5125	2.4825	2.4150	2.4188	2.5863	2.4450
a_4	2.5113	2.4888	2.4725	2.4775	2.4450	2.4788	2.5213	2.4450
a_5	2.4713	2.4788	2.4725	2.4825	2.5550	2.4688	2.4363	2.4050
a_0	2.5031	2.4888	2.4856	2.4850	2.4506	2.4388	2.5338	2.4363
a_0/W	0.5070	0.5012	0.5041	0.5043	0.4991	0.4956	0.5162	0.4964
$a_{max}-a_{min}$	0.04	0.04	0.04	0.02	0.14	0.07	0.15	0.04
10% a_0	0.25	0.25	0.25	0.25	0.25	0.24	0.25	0.24

Appendix B – Loading Rate

The loading rate (N/min) was determined from the elastic part of the load-CMOD plot, as seen for sample A and sample B in Figure 59 and Figure 60, respectively. For both samples, calculations were based on the linear section between 99-300 N.

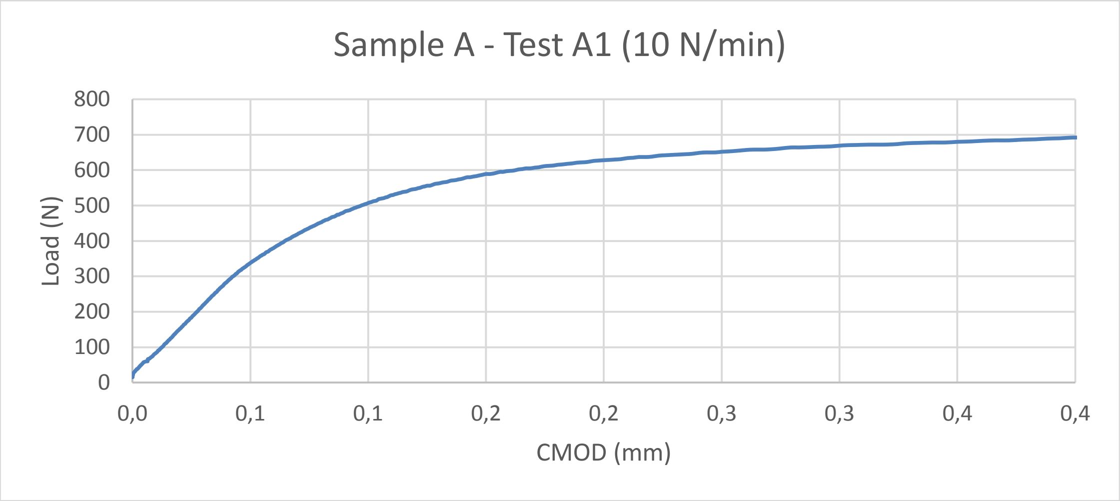

Figure 59 - Sample A: Load-CMOD plot in air.

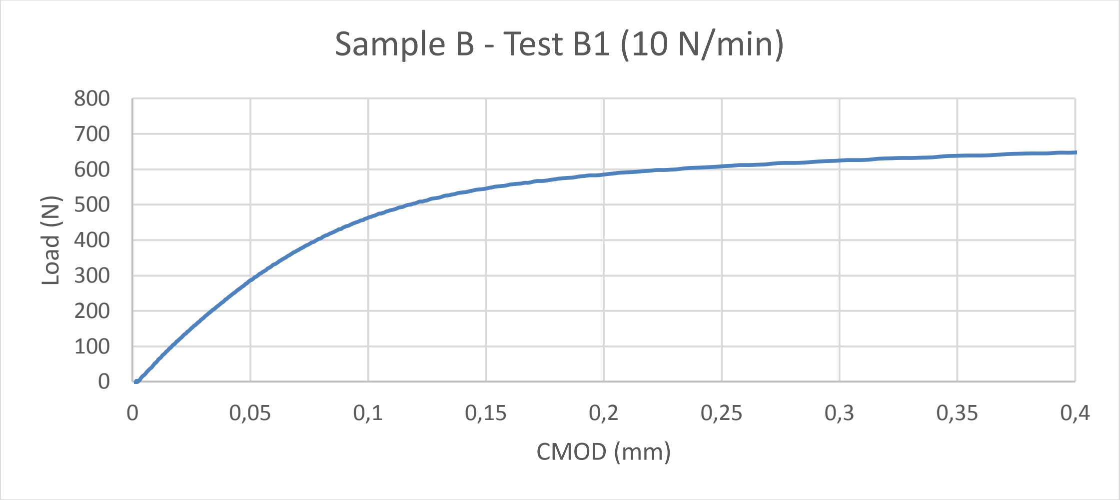

Figure 60 - Sample B: Load-CMOD plot in air.

The values for time and displacement are extracted directly from the raw data sets, and are thus not included. The stress intensity factor is calculated from equation 2.3, resulting in a dK/dt approximately 13.5 times higher than desired, as seen in Table 9.

$$K_I = \frac{P}{B\sqrt{W}} f\left(\frac{a}{W}\right) \tag{2.3}$$

Table 9 – Data from linear part of load-CMOD curves.

	ΔP (N)	**Δt (s)**	**Δdisplacement (m)**	**ΔK (MPa*sqrt(m))**	**dK/dt (MPa*sqrt(m)*s^{-1})**
Sample A	201	1200	$6.54 \cdot 10^{-5}$	10.98	$9.2 \cdot 10^{-3}$
Sample B	202	1200	$8.65 \cdot 10^{-5}$	11.04	$9.2 \cdot 10^{-3}$
Ref. [73]	-	-	-	-	$6.8 \cdot 10^{-4}$

To obtain the desired dK/dt, the initial loading rate of 10 N/min was reduced by a factor 13.5, corresponding to a loading rate of 0.74 N/min. This loading rate was applied for all other testing, both in air and under CP.

Due to time limitations, the calculation of dK/dt was performed before the specimens were measured. However, upon inserting the measured values, the values calculated above do not change significantly, so that the initial calculations should still apply for the estimate of loading rate with respect to dK/dt.

Appendix C – Load-CMOD Correlation

The following operations were performed on all 4 test sets from testing in air. The approach is shown with the test results from sample A, test 1 (air, 10 N/min).

The measured displacement was corrected in order to ensure that the steepest section of the linear part of the curve fit through the x-y origin, as seen in Figure 61. The plastic displacement was obtained from equation D.1, where all parameters are given by the plot in Figure 61.

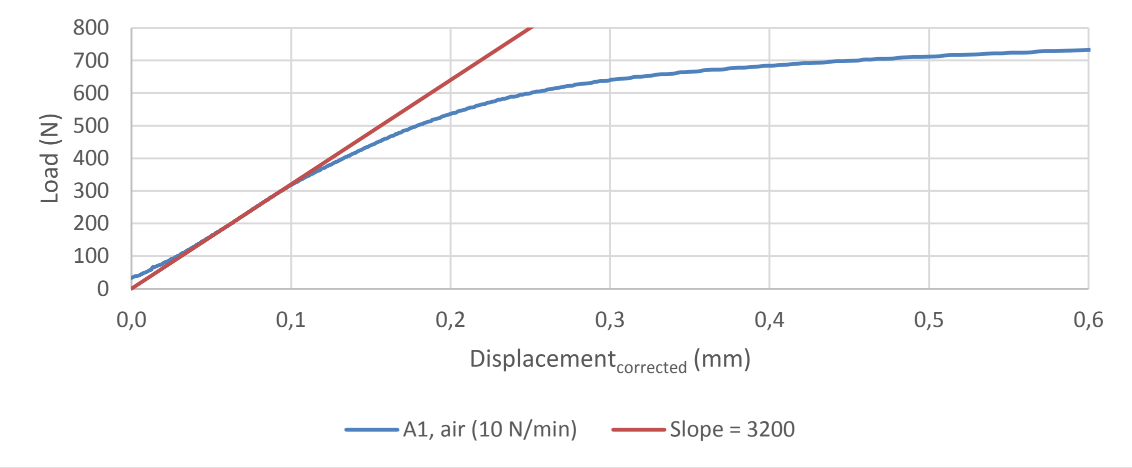

Figure 61 - Load-displacement$_{corrected}$ plot for sample A, tested in air (10 N/min).

$$Displacement_{plastic} = Displacement_{corrected} - \frac{Load}{slope_{displacement}} \qquad \text{(D.1)}$$

The measured CMOD was corrected in order to ensure that the curve fit through the x-y origin of the graph, as seen in Figure 62. The plastic CMOD, V_p, was obtained from equation D.2, where all parameters are given by the plot in Figure 62.

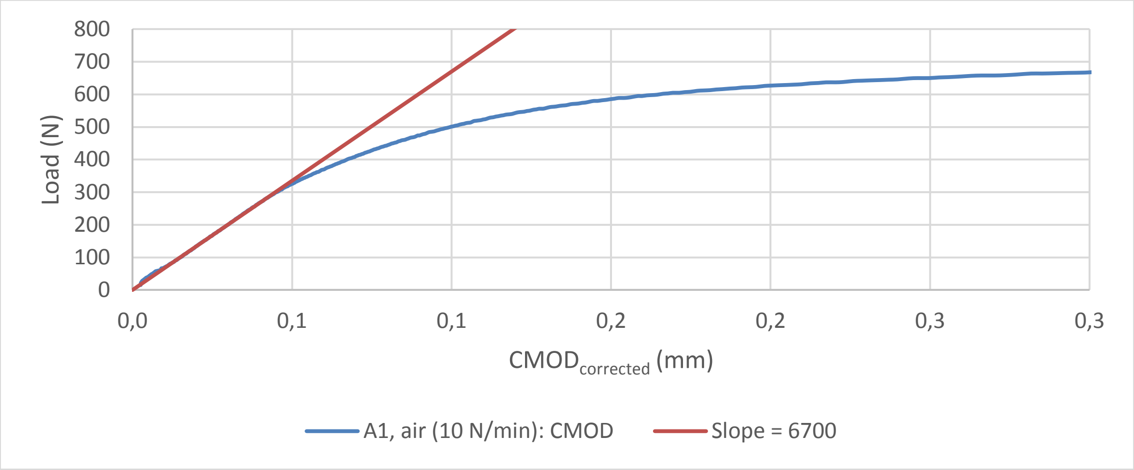

Figure 62 - Load-CMOD plot for sample A, tested in air (10 N/min).

$$V_p = CMOD - \frac{Load}{slope_{CMOD}} \qquad (D.2)$$

The slopes for the displacement and CMOD corrections are given in Table 10.

Table 10 - Slopes for corrected displacement and CMOD.

	A1	**A3**	**A4**	**A5**	**B1**	**B3**	**B4**	**B5**
Slope$_{\text{displacement}}$	3200	2450	2350	2100	2350	2800	2400	2200
Slope$_{\text{CMOD}}$	6700	6200	-	-	6600	6000	-	.

The relationship between V_p and plastic displacement was described by equation D.3

$$\frac{V_p}{Displacement_{plastic}} = Factor \qquad (D.3)$$

The factor at maximum load was calculated for all tests in air, and the results are summarized in Table 11.

Table 11 - Factors describing the relationship between V_p and displacement$_{\text{plastic}}$.

	A1	**A3**	**B1**	**B3**
Factor	1.43	1.66	1.63	1.59

For samples tested under CP, where the use of clip gages to measure the CMOD was not possible, the factors found for testing in air were utilized as illustrated in equation D.4 and D.5. The factors from test A3 and B3 was selected, as these were performed at the same loading rate as testing under CP. The plastic displacement for testing under CP was obtained in the same manner as for testing in air, as described above.

$$V_p(Sample\ A) = 1.66 * Displacement_{plastic} \tag{D.4}$$

$$V_p(Sample\ B) = 1.59 * Displacement_{plastic} \tag{D.5}$$

From these equations, load-V_p curves were plotted for testing under CP. For the samples tested in air, V_p was calculated from the measured CMOD. The correlation between V_p based on the measured CMOD and V_p based on the measured displacement is illustrated for sample A, test 1, in Figure 63, showing a good correlation between the two. The plastic CMOD, V_p, at maximum load for the specimens tested under CP was extracted from the load-V_p curves.

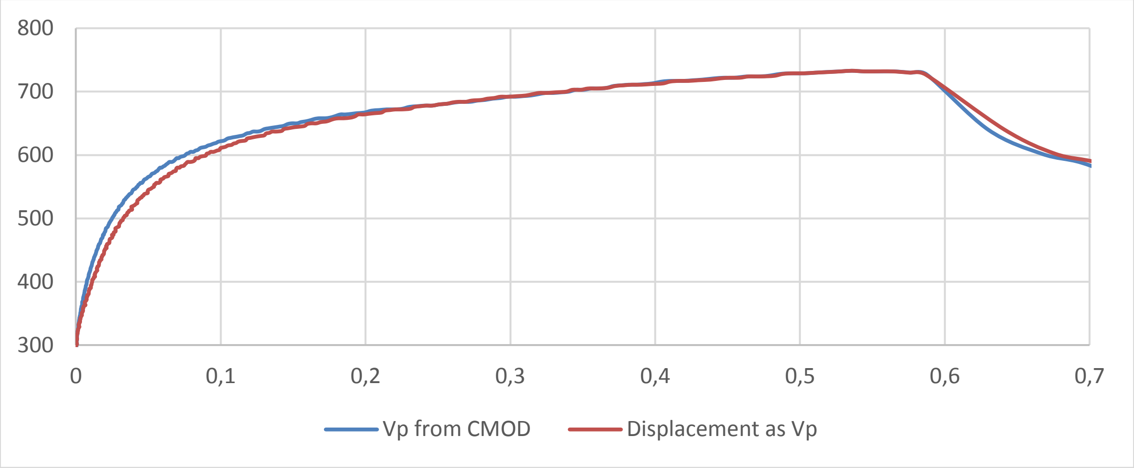

Figure 63 - Correlation between V_p from CMOD and V_p from displacement (plastic).

Appendix D – Load-V_p Curves

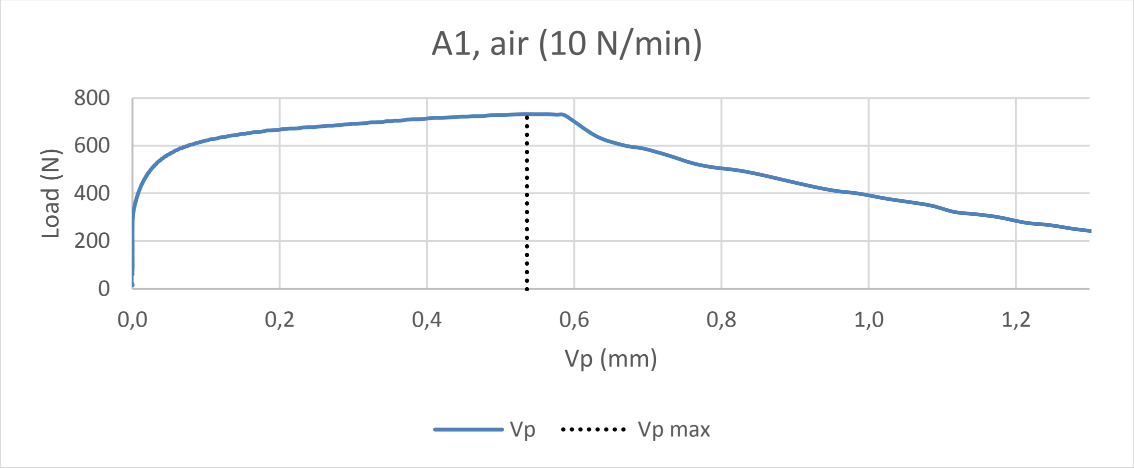

Figure 64 - Load-V_p curve for sample A, tested in air at a loading rate of 10 N/min.

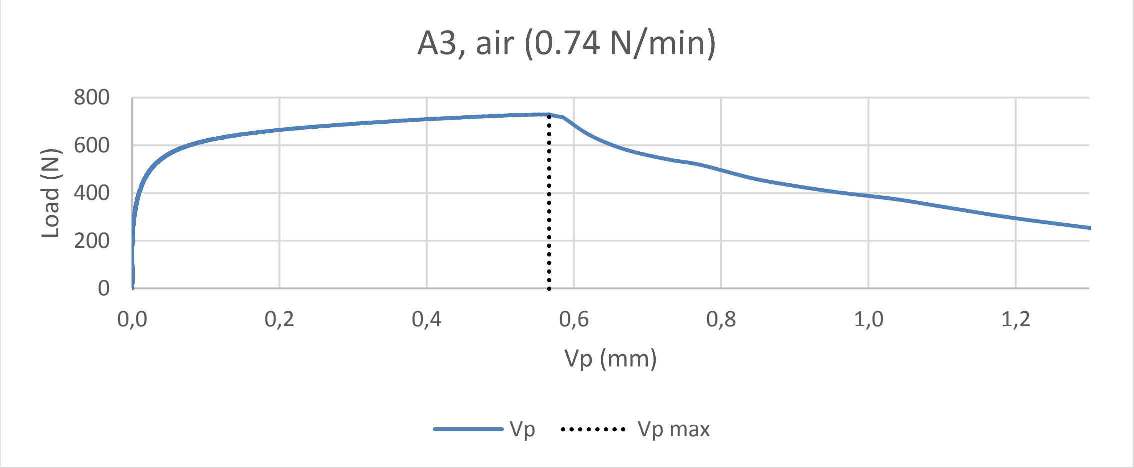

Figure 65 - Load-V_p curve for sample A, tested in air at a loading rate of 0.74 N/min.

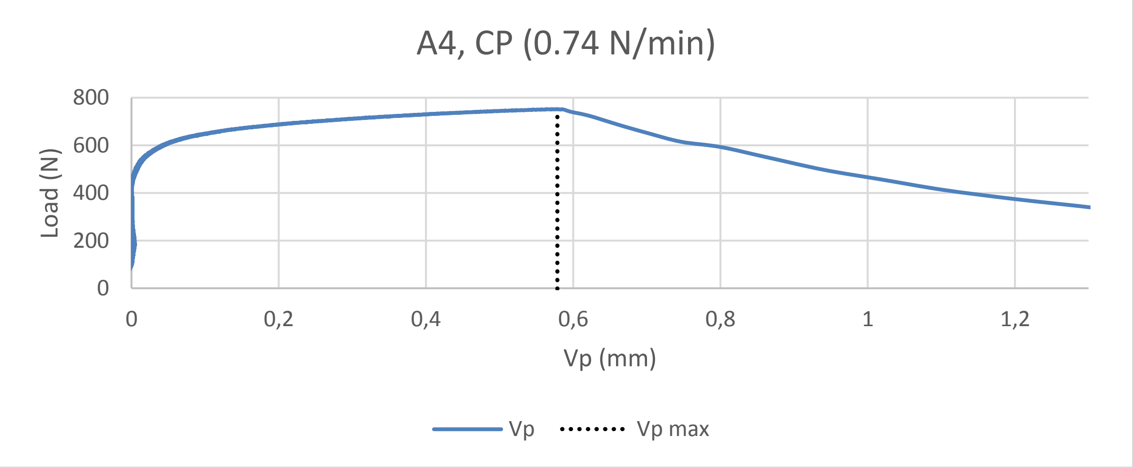

Figure 66 - Load-V_p curve for sample A, tested under CP at a loading rate of 0.74 N/min.

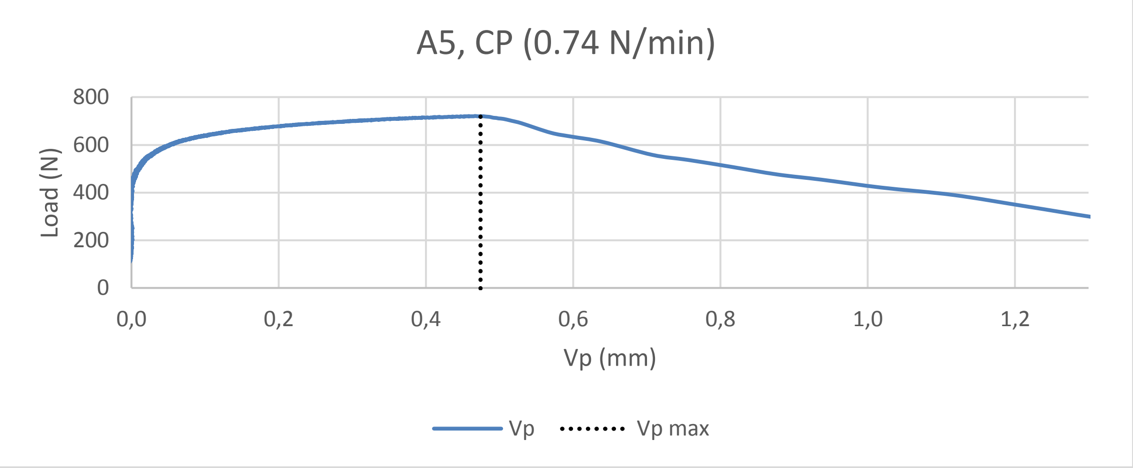

Figure 67 - Load-V_p curve for sample A, tested under CP at a loading rate of 0.74 N/min.

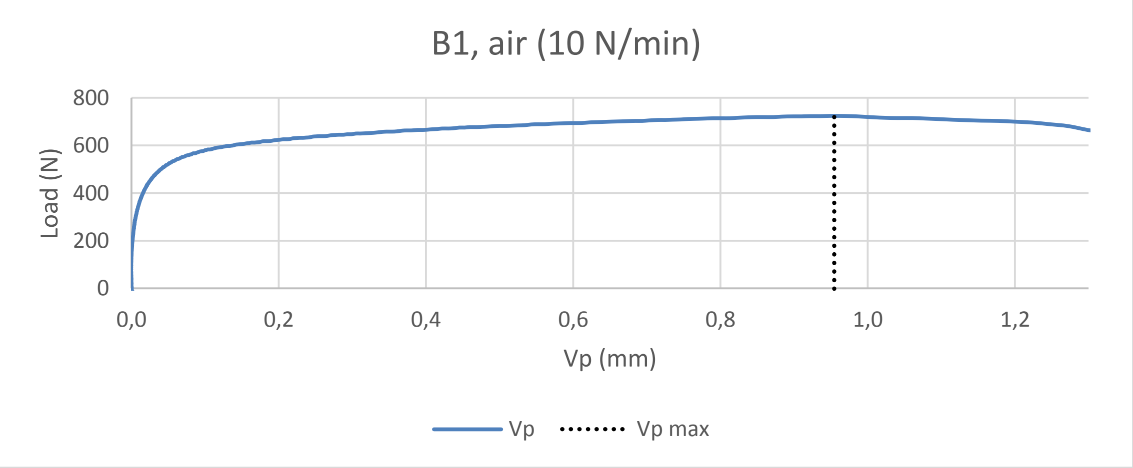

Figure 68 - Load-V_p curve for sample B, tested in air at a loading rate of 10 N/min.

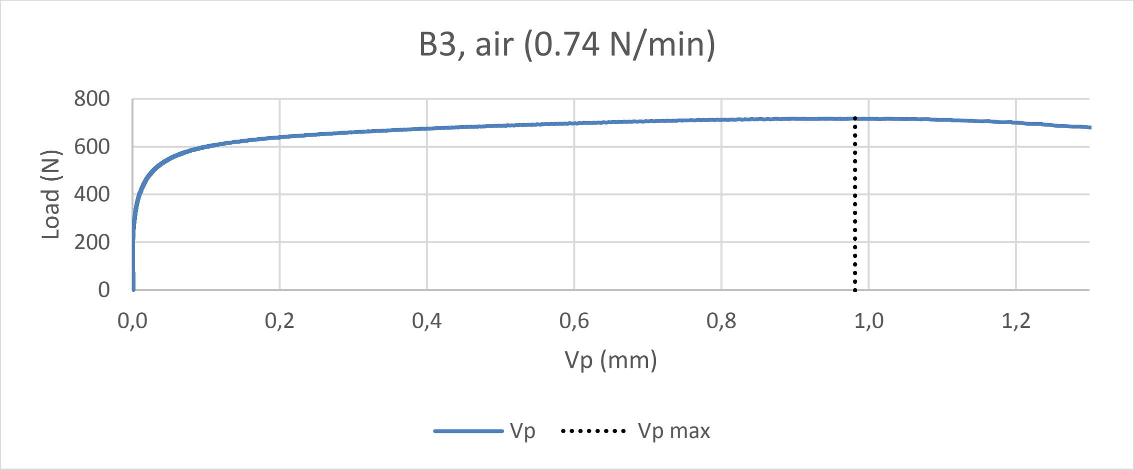

Figure 69 - Load-V_p curve for sample B, tested in air at a loading rate of 0.74 N/min.

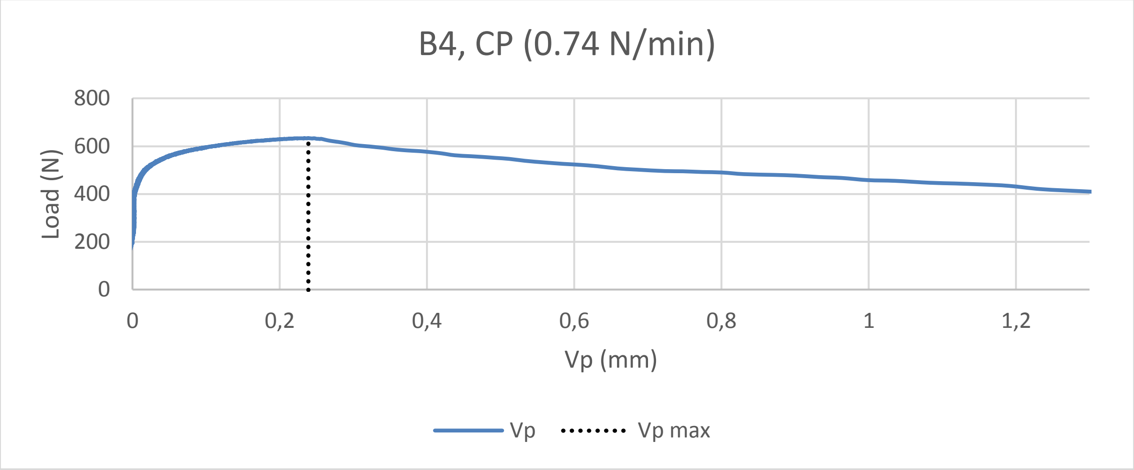

Figure 70 - Load-V_p curve for sample B, tested under CP at a loading rate of 0.74 N/min.

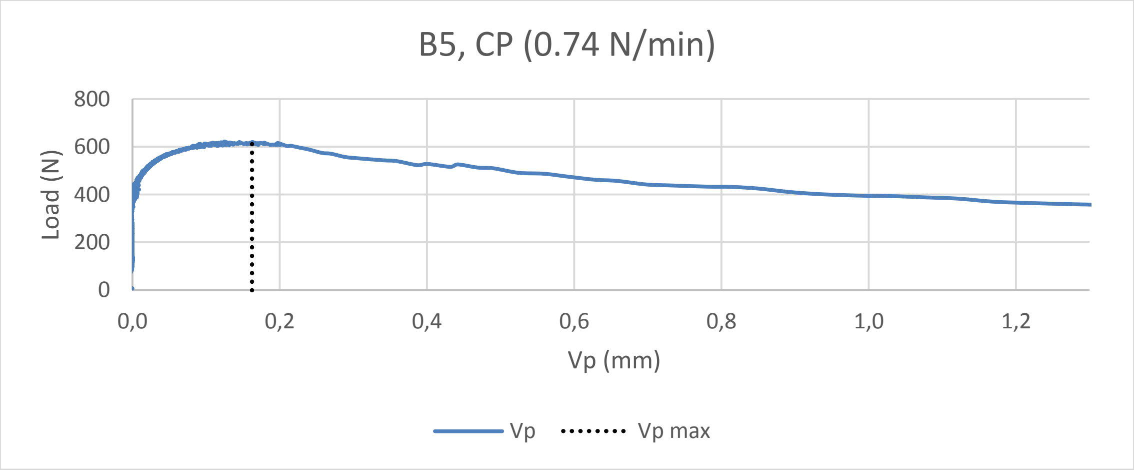

Figure 71 - Load-V_p curve for sample B, tested under CP at a loading rate of 0.74 N/min.

Appendix E – Fractographs

Investigations of the fracture surfaces was performed on all specimens. However, only a selection of the most relevant images are included here, as a lot of the images showed the same features.

For testing in air, the following is included

- A3, fracture surface on clad section of specimen.
- B3, fracture surface on clad and BM section of specimen.

For testing under CP, the following is included

- A5, fracture surface on clad and BM section of specimen.
- B4, fracture surface on clad and BM section of specimen.

It should be noted that the term “clad section of specimen” and “BM section of specimen” refers to which part of the fracture CT specimen was investigated. Whether the fracture surface is from the clad or BM is discussed in section 5.5 for selected samples.

Testing in air:

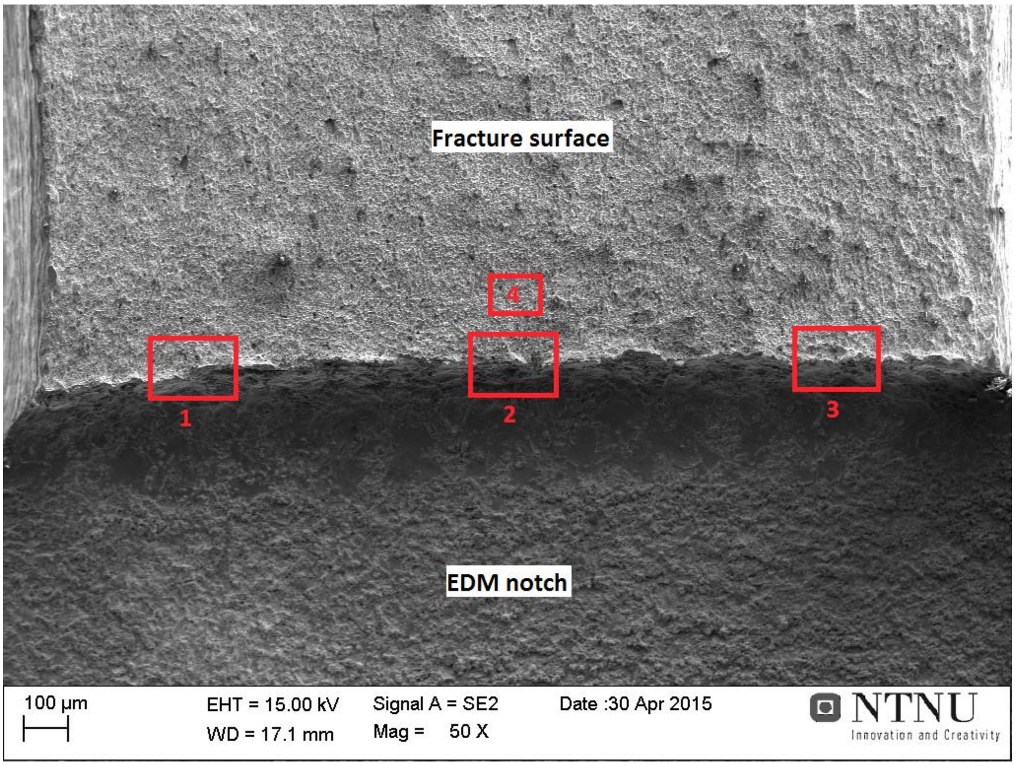

Figure 72 - Sample A, test 3, fracture surface on clad section of specimen.

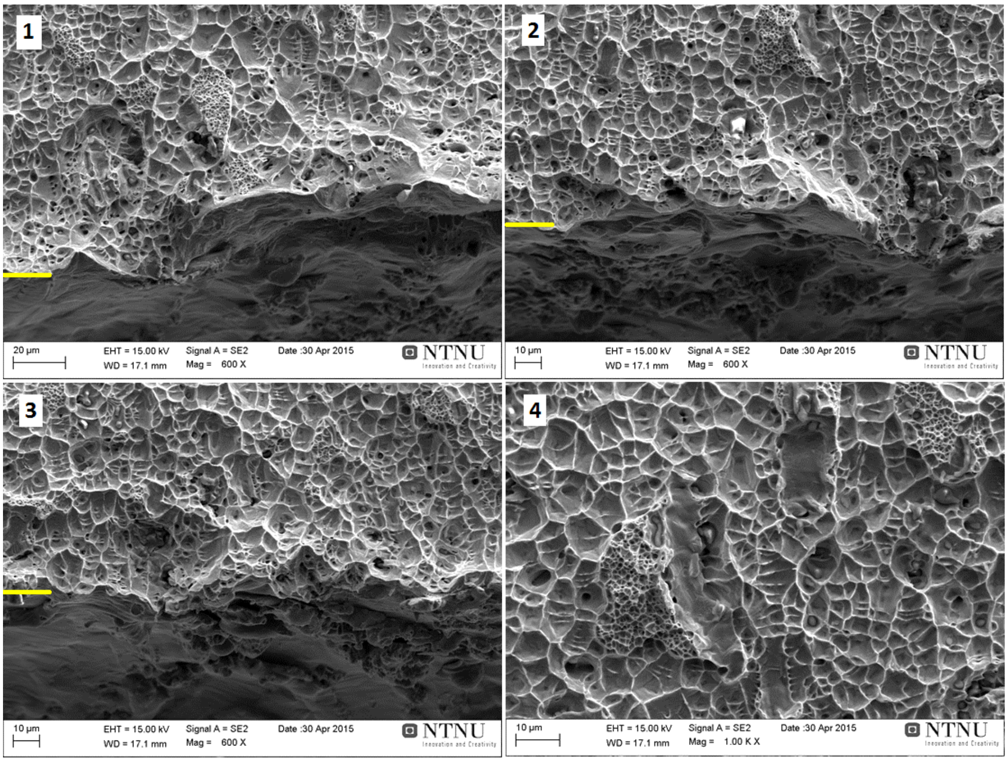

Figure 73 - Sample A, test 3, clad section of specimen. The fracture surface is above the yellow line. The areas 1-4 are indicated in Figure 72 above.

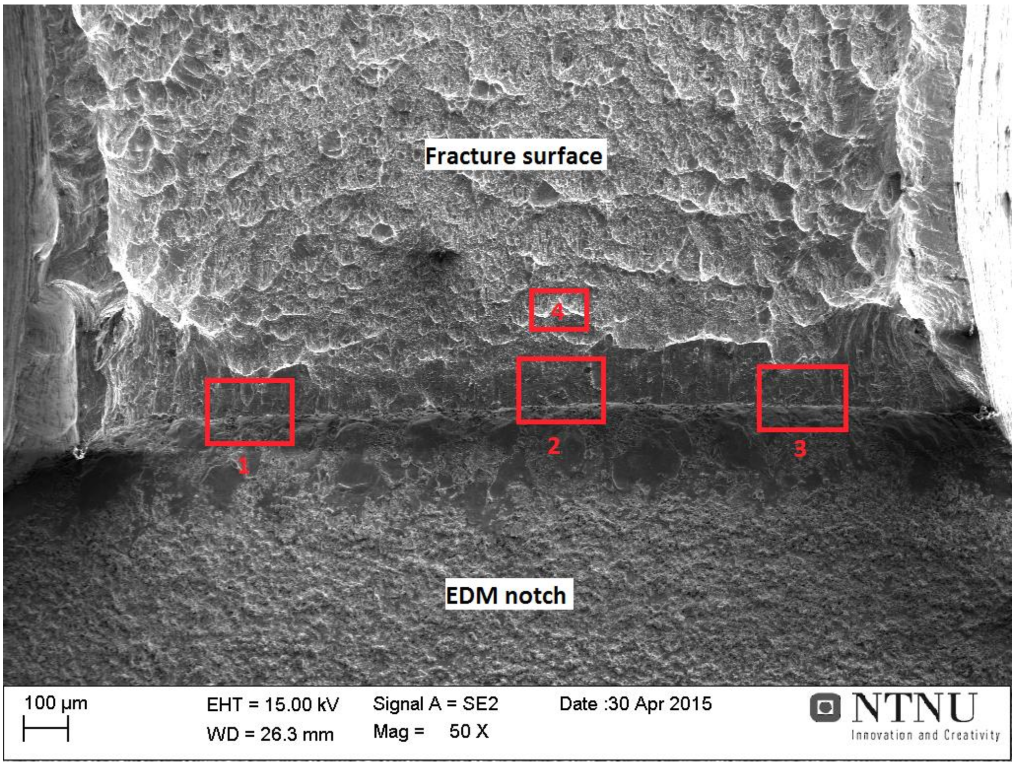

Figure 74 - Sample B, test 3, fracture surface on clad section of specimen..

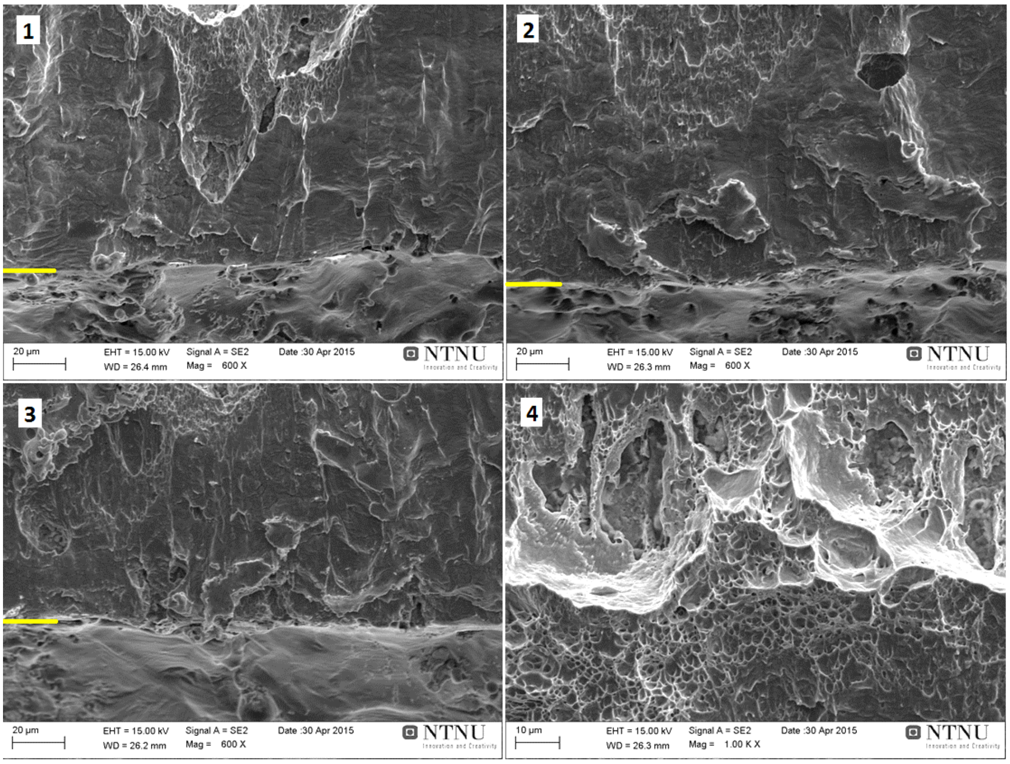

Figure 75 - Sample B, test 3, clad section of specimen. The fracture surface is above the yellow line. The areas 1-4 are indicated in Figure 74 above.

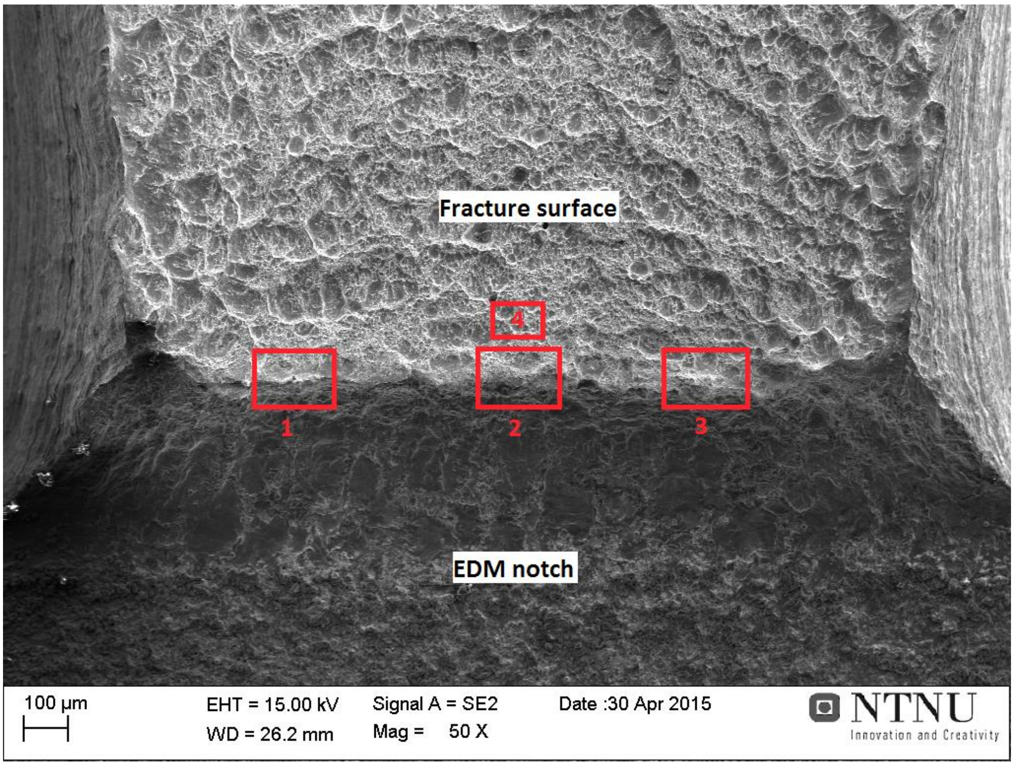

Figure 76 - Sample B, test 3, fracture surface on BM section of specimen.

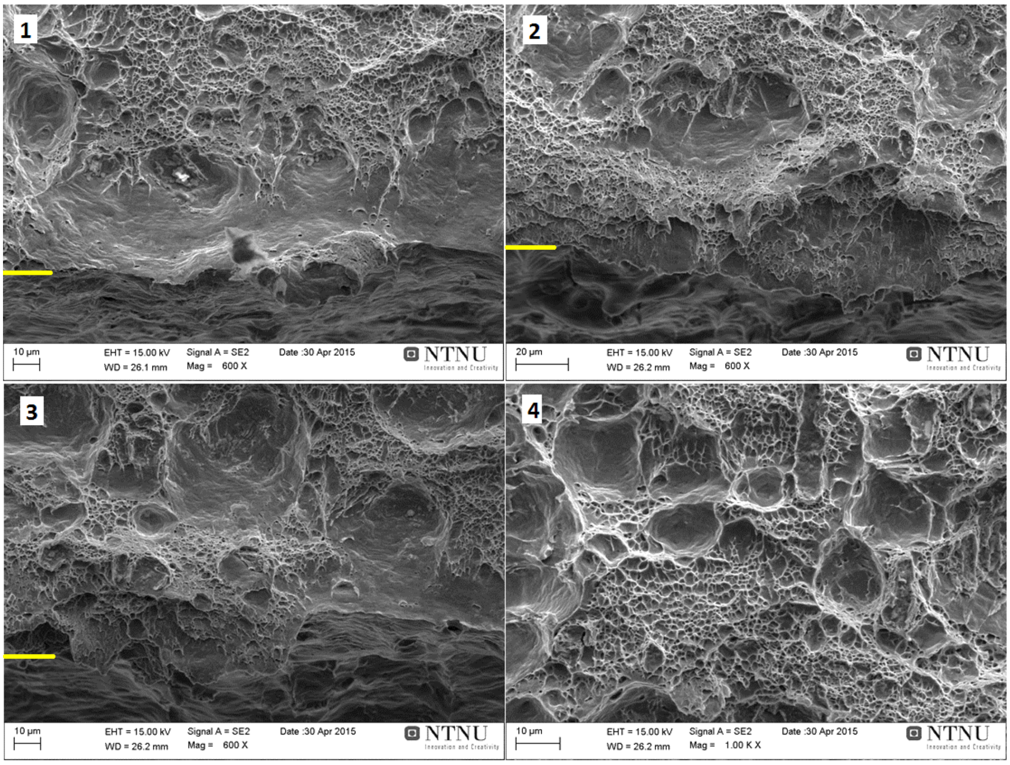

Figure 77 - Sample B, test 3, BM section of specimen. The fracture surface is above the yellow line. The areas 1-4 are indicated in Figure 76 above.

Testing under CP:

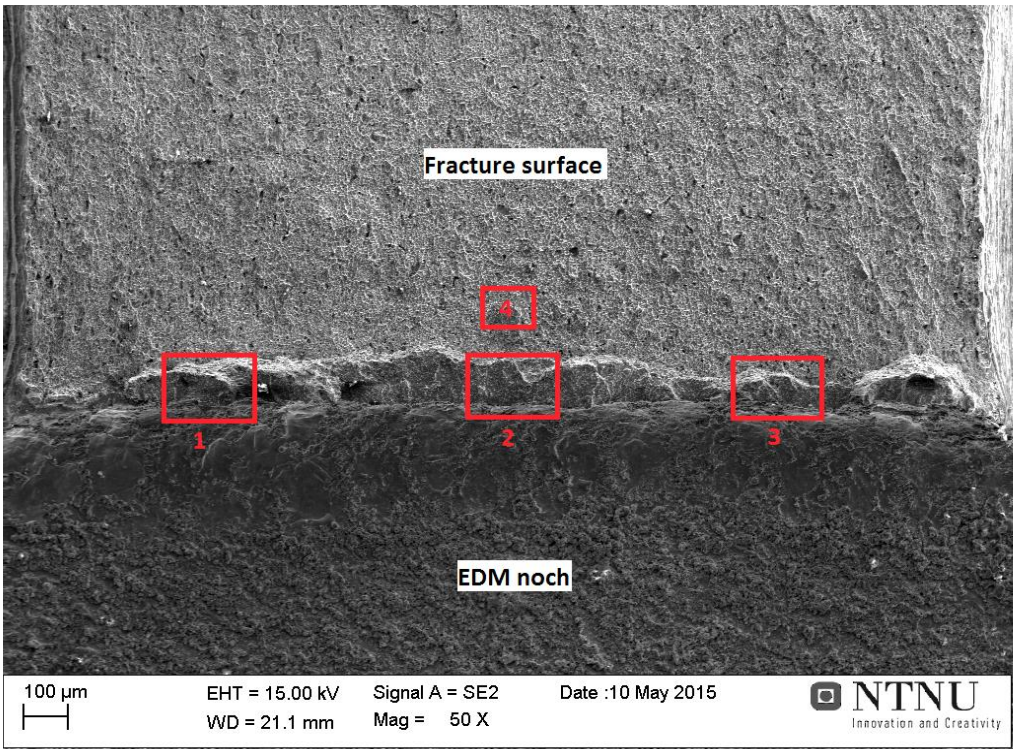

Figure 78 - Sample A, test 5, fracture surface on clad section of specimen.

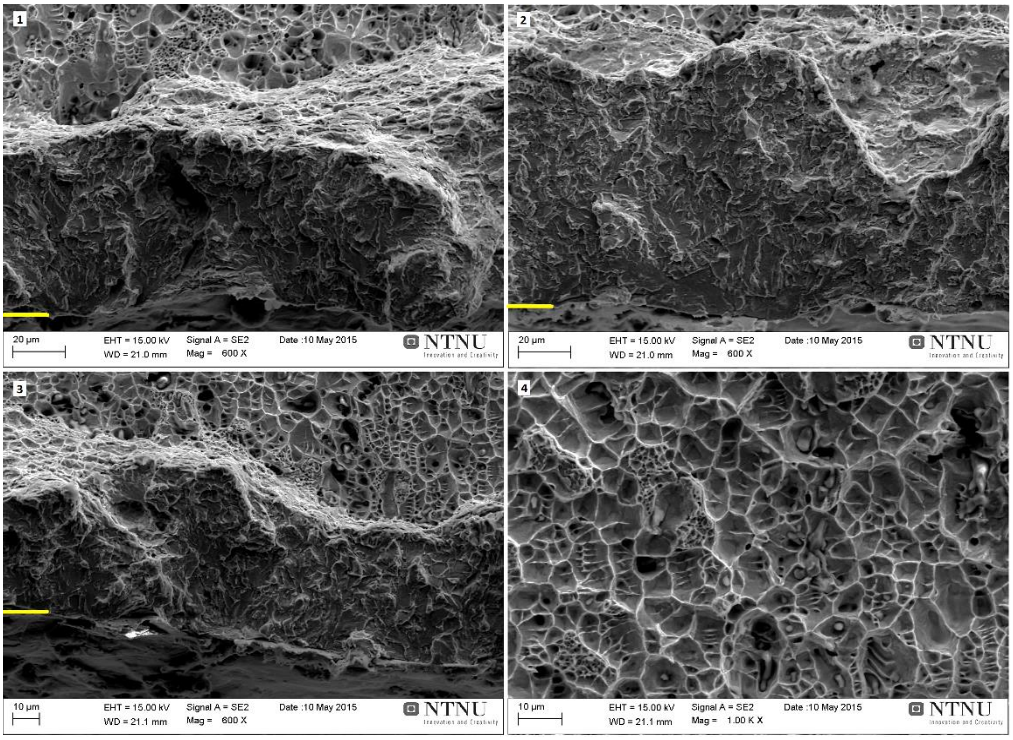

Figure 79 - Sample A, test 5, clad section of specimen. The fracture surface is above the yellow line. The areas 1-4 are indicated in Figure 78 above.

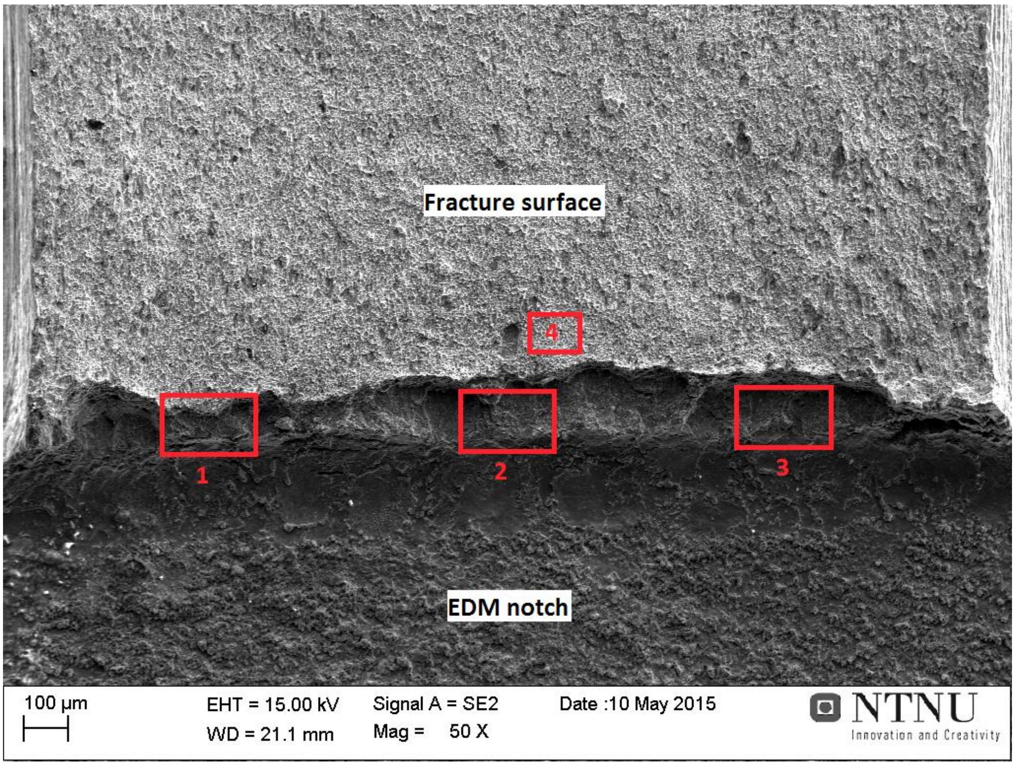

Figure 80 - Sample A, test 5, fracture surface on BM section of specimen.

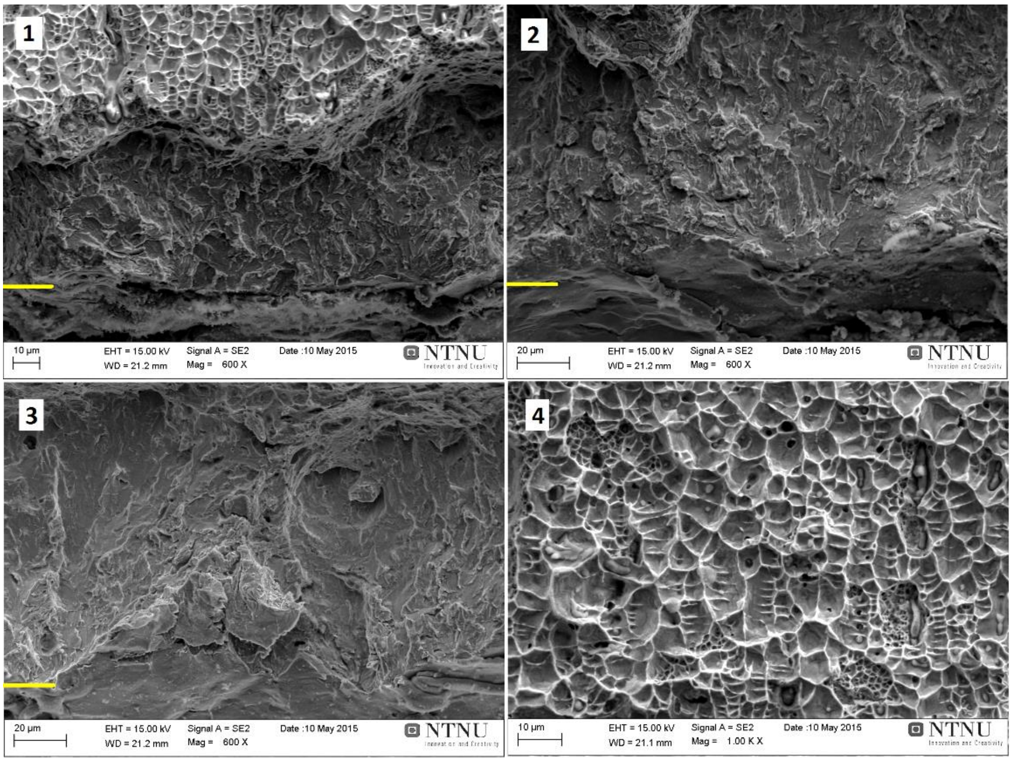

Figure 81 - Sample A, test 5, BM section of specimen. The fracture surface is above the yellow line. The areas 1-4 are indicated in Figure 80 above.

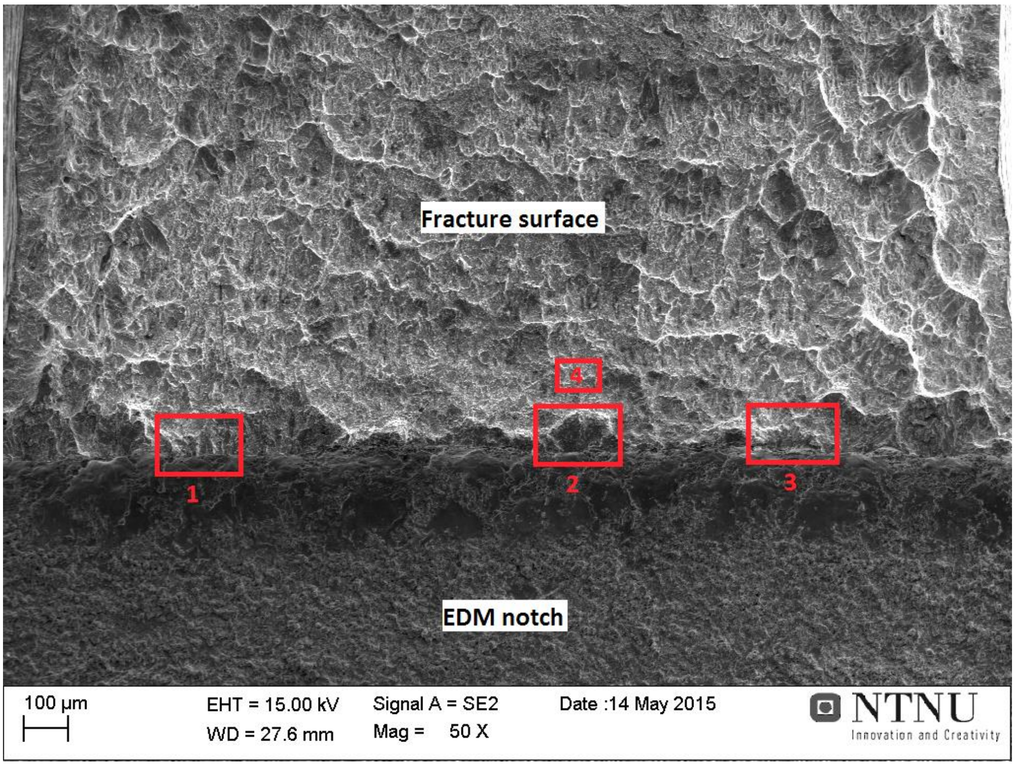

Figure 82 – Sample B, test 4, fracture surface on clad section of specimen.

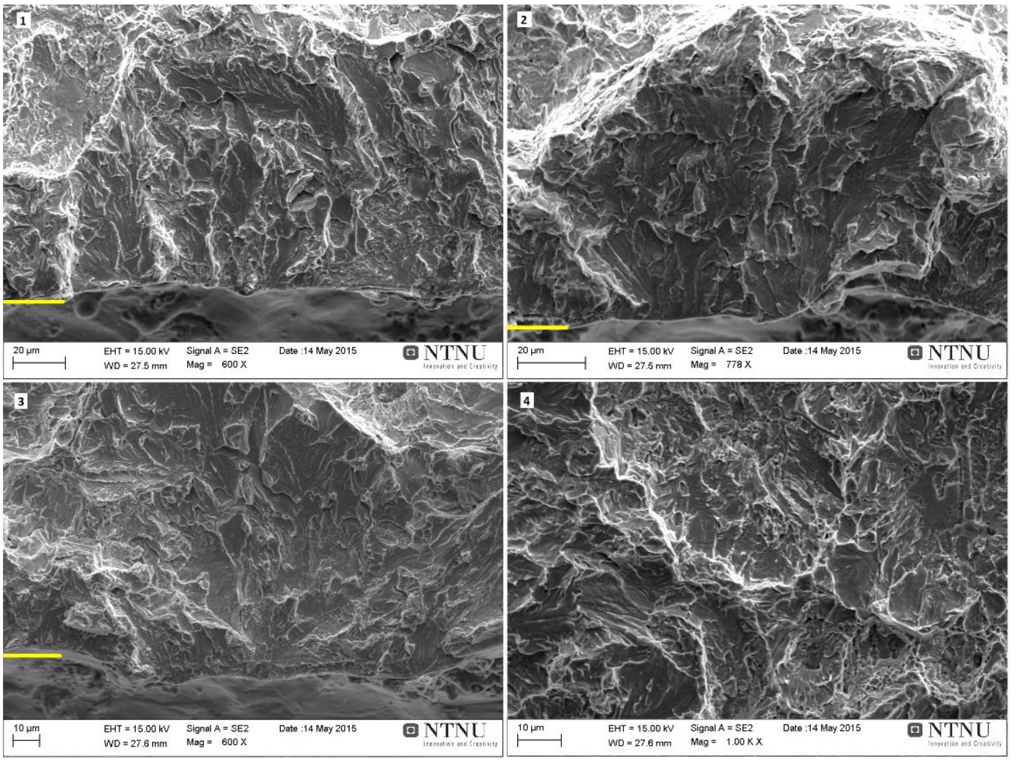

Figure 83 - Sample B, test 4, clad section of specimen. The fracture surface is above the yellow line. The areas 1-4 are indicated in Figure 82 above.

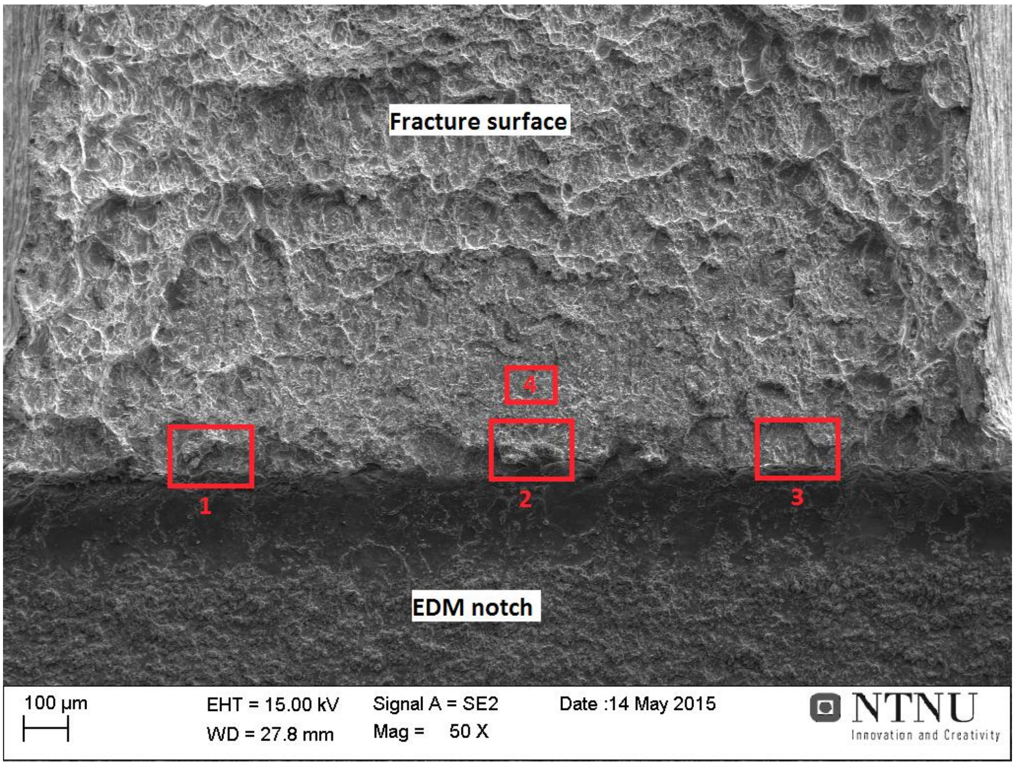

Figure 84 - Sample B, test 4, fracture surface on BM section of specimen.

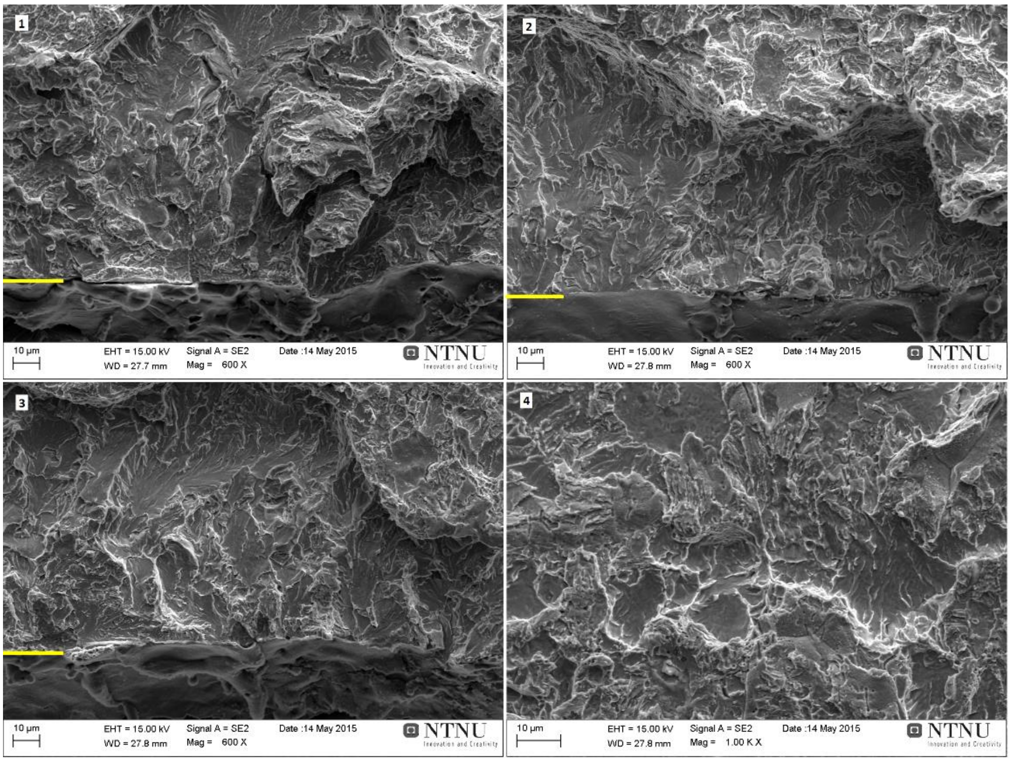

Figure 85 - Sample B, test 4, BM section of specimen. The fracture surface is above the yellow line. The areas 1-4 are indicated in Figure 84 above.

Appendix F - Master Thesis Description and Formal Requirements

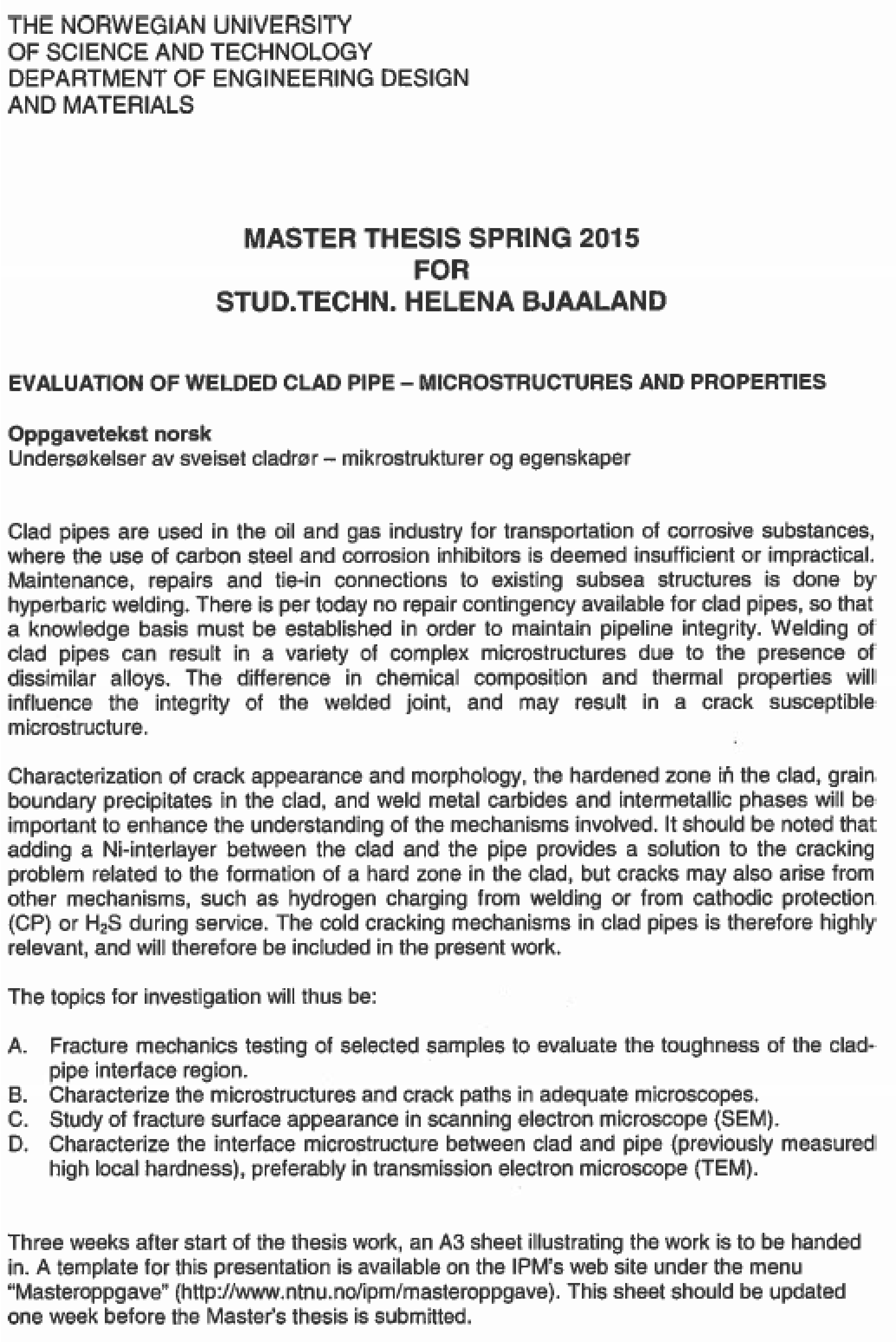

THE NORWEGIAN UNIVERSITY
OF SCIENCE AND TECHNOLOGY
DEPARTMENT OF ENGINEERING DESIGN
AND MATERIALS

MASTER THESIS SPRING 2015
FOR
STUD.TECHN. HELENA BJAALAND

EVALUATION OF WELDED CLAD PIPE – MICROSTRUCTURES AND PROPERTIES

Oppgavetekst norsk
Undersøkelser av sveiset cladrør – mikrostrukturer og egenskaper

Clad pipes are used in the oil and gas industry for transportation of corrosive substances, where the use of carbon steel and corrosion inhibitors is deemed insufficient or impractical. Maintenance, repairs and tie-in connections to existing subsea structures is done by hyperbaric welding. There is per today no repair contingency available for clad pipes, so that a knowledge basis must be established in order to maintain pipeline integrity. Welding of clad pipes can result in a variety of complex microstructures due to the presence of dissimilar alloys. The difference in chemical composition and thermal properties will influence the integrity of the welded joint, and may result in a crack susceptible microstructure.

Characterization of crack appearance and morphology, the hardened zone in the clad, grain boundary precipitates in the clad, and weld metal carbides and intermetallic phases will be important to enhance the understanding of the mechanisms involved. It should be noted that adding a Ni-interlayer between the clad and the pipe provides a solution to the cracking problem related to the formation of a hard zone in the clad, but cracks may also arise from other mechanisms, such as hydrogen charging from welding or from cathodic protection (CP) or H_2S during service. The cold cracking mechanisms in clad pipes is therefore highly relevant, and will therefore be included in the present work.

The topics for investigation will thus be:

A. Fracture mechanics testing of selected samples to evaluate the toughness of the clad-pipe interface region.
B. Characterize the microstructures and crack paths in adequate microscopes.
C. Study of fracture surface appearance in scanning electron microscope (SEM).
D. Characterize the interface microstructure between clad and pipe (previously measured high local hardness), preferably in transmission electron microscope (TEM).

Three weeks after start of the thesis work, an A3 sheet illustrating the work is to be handed in. A template for this presentation is available on the IPM's web site under the menu "Masteroppgave" (http://www.ntnu.no/ipm/masteroppgave). This sheet should be updated one week before the Master's thesis is submitted.

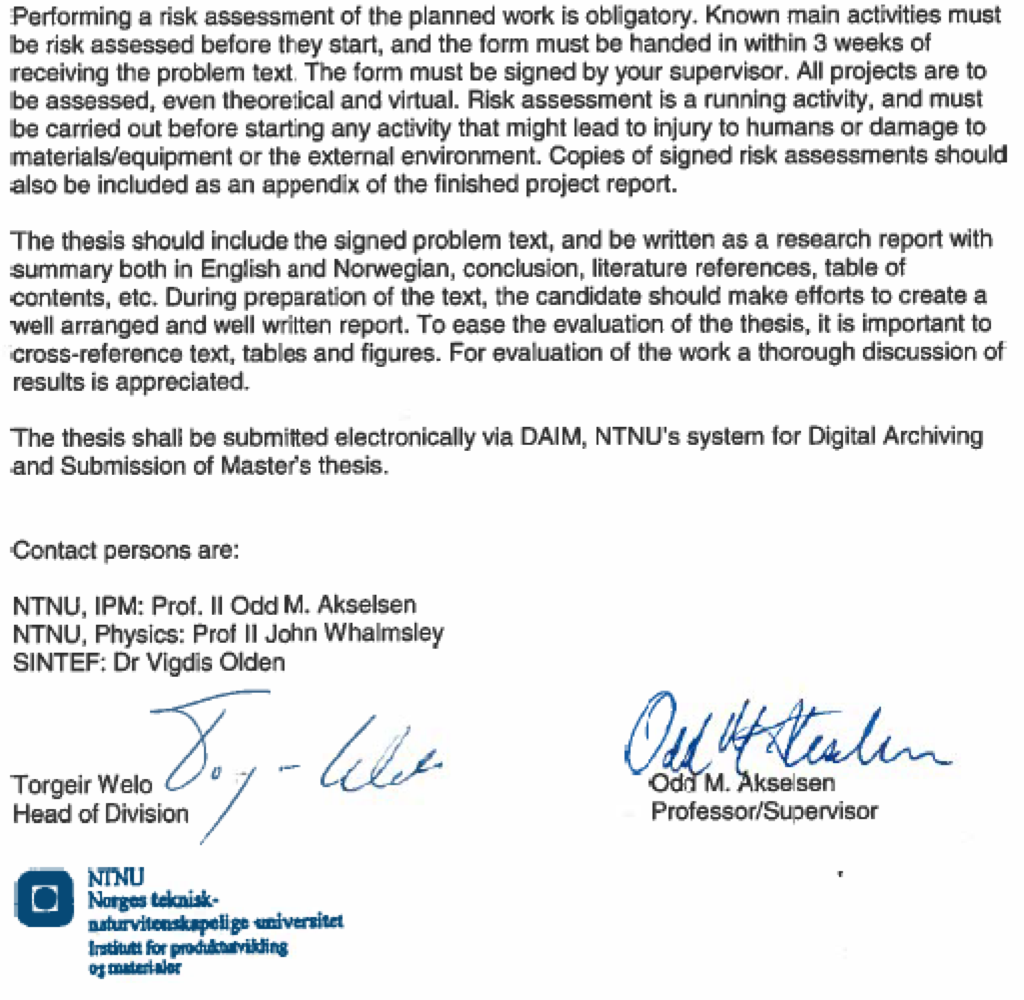

Performing a risk assessment of the planned work is obligatory. Known main activities must be risk assessed before they start, and the form must be handed in within 3 weeks of receiving the problem text. The form must be signed by your supervisor. All projects are to be assessed, even theoretical and virtual. Risk assessment is a running activity, and must be carried out before starting any activity that might lead to injury to humans or damage to materials/equipment or the external environment. Copies of signed risk assessments should also be included as an appendix of the finished project report.

The thesis should include the signed problem text, and be written as a research report with summary both in English and Norwegian, conclusion, literature references, table of contents, etc. During preparation of the text, the candidate should make efforts to create a well arranged and well written report. To ease the evaluation of the thesis, it is important to cross-reference text, tables and figures. For evaluation of the work a thorough discussion of results is appreciated.

The thesis shall be submitted electronically via DAIM, NTNU's system for Digital Archiving and Submission of Master's thesis.

Contact persons are:

NTNU, IPM: Prof. II Odd M. Akselsen
NTNU, Physics: Prof II John Whalmsley
SINTEF: Dr Vigdis Olden

Torgeir Welo
Head of Division

Odd M. Akselsen
Professor/Supervisor

NTNU
Norges teknisk-
naturvitenskapelige universitet
Institutt for produktutvikling
og materialer

Appendix G – Risk Assessment

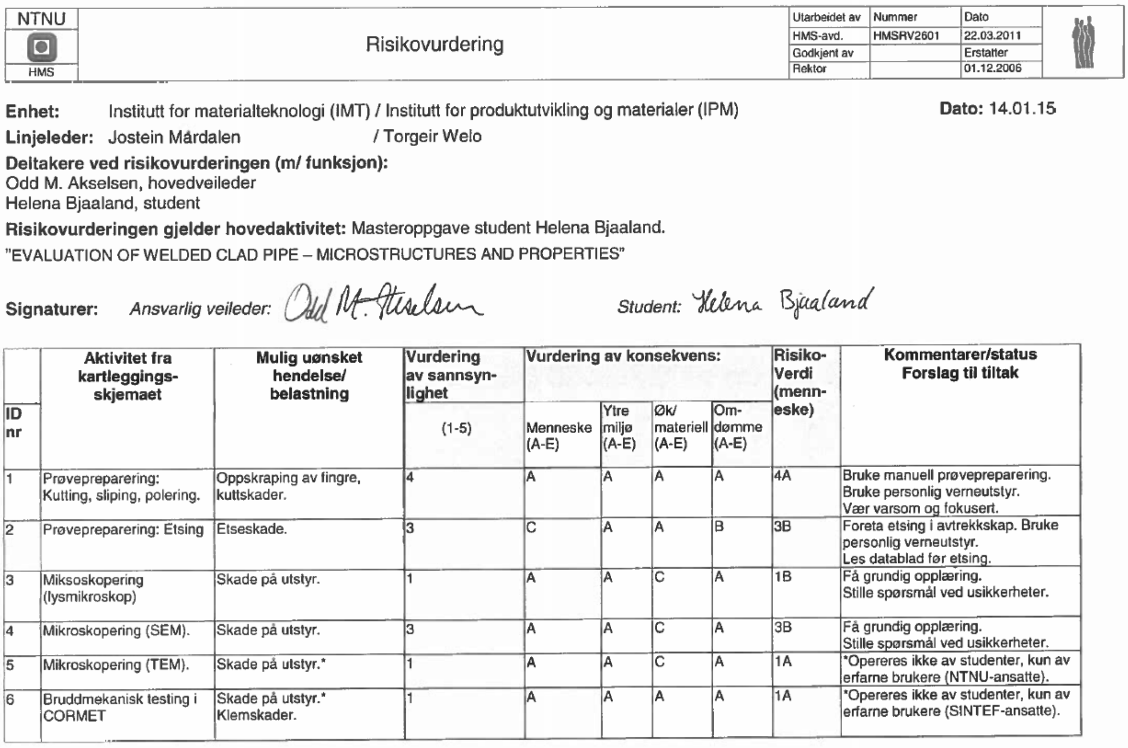

NTNU
HMS

Risikovurdering

Utarbeidet av	Nummer	Dato
HMS-avd.	HMSRV2601	22.03.2011
Godkjent av		Erstatter
Rektor		01.12.2006

Enhet: Institutt for materialteknologi (IMT) / Institutt for produktutvikling og materialer (IPM) **Dato:** 14.01.15
Linjeleder: Jostein Mårdalen / Torgeir Welo
Deltakere ved risikovurderingen (m/ funksjon):
Odd M. Akselsen, hovedveileder
Helena Bjaaland, student

Risikovurderingen gjelder hovedaktivitet: Masteroppgave student Helena Bjaaland.
"EVALUATION OF WELDED CLAD PIPE – MICROSTRUCTURES AND PROPERTIES"

Signaturer: *Ansvarlig veileder:* Odd M. Akselsen *Student:* Helena Bjaaland

ID nr	Aktivitet fra kartleggings-skjemaet	Mulig uønsket hendelse/ belastning	Vurdering av sannsyn-lighet	Vurdering av konsekvens:				Risiko-Verdi (menn-eske)	Kommentarer/status Forslag til tiltak
			(1-5)	Menneske (A-E)	Ytre miljø (A-E)	Øk/ materiell (A-E)	Om-dømme (A-E)		
1	Prøvepreparering: Kutting, sliping, polering.	Oppskraping av fingre, kuttskader.	4	A	A	A	A	4A	Bruke manuell prøvepreparering. Bruke personlig verneutstyr. Vær varsom og fokusert.
2	Prøvepreparering: Etsing	Etseskade.	3	C	A	A	B	3B	Foreta etsing i avtrekkskap. Bruke personlig verneutstyr. Les datablad før etsing.
3	Miksoskopering (lysmikroskop)	Skade på utstyr.	1	A	A	C	A	1B	Få grundig opplæring. Stille spørsmål ved usikkerheter.
4	Mikroskopering (SEM).	Skade på utstyr.	3	A	A	C	A	3B	Få grundig opplæring. Stille spørsmål ved usikkerheter.
5	Mikroskopering (TEM).	Skade på utstyr.*	1	A	A	C	A	1A	*Opereres ikke av studenter, kun av erfarne brukere (NTNU-ansatte).
6	Bruddmekanisk testing i CORMET	Skade på utstyr.* Klemskader.	1	A	A	A	A	1A	*Opereres ikke av studenter, kun av erfarne brukere (SINTEF-ansatte).

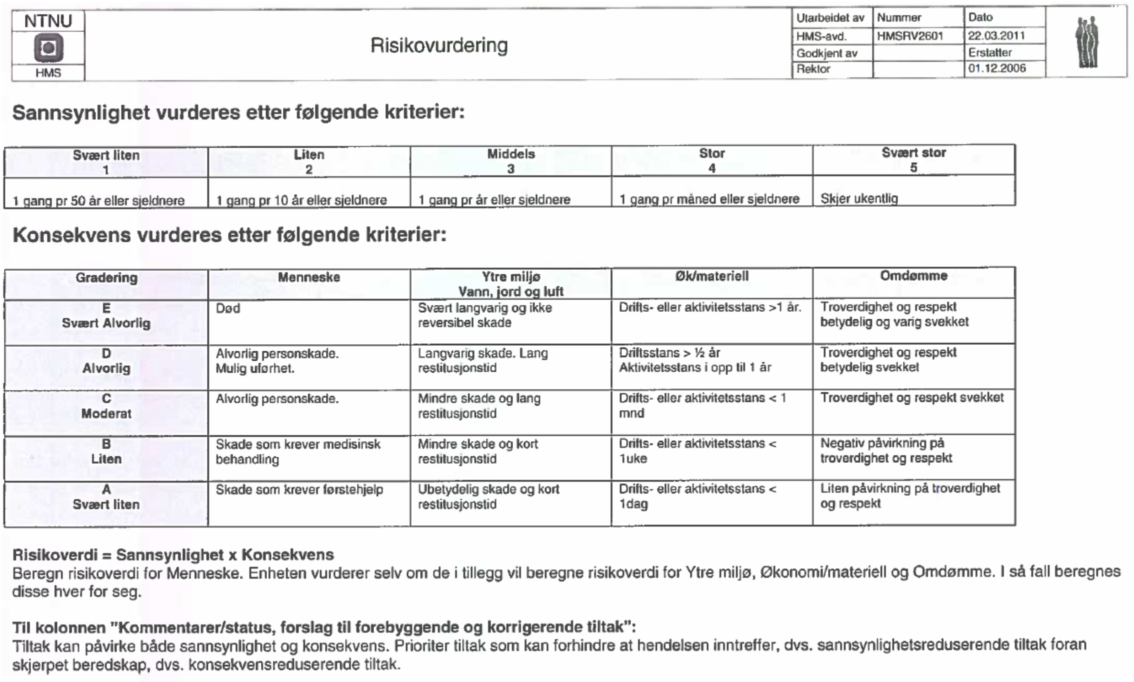

NTNU
HMS

Risikovurdering

Utarbeidet av	Nummer	Dato
HMS-avd.	HMSRV2601	22.03.2011
Godkjent av		Erstatter
Rektor		01.12.2006

Sannsynlighet vurderes etter følgende kriterier:

Svært liten 1	Liten 2	Middels 3	Stor 4	Svært stor 5
1 gang pr 50 år eller sjeldnere	1 gang pr 10 år eller sjeldnere	1 gang pr år eller sjeldnere	1 gang pr måned eller sjeldnere	Skjer ukentlig

Konsekvens vurderes etter følgende kriterier:

Gradering	Menneske	Ytre miljø Vann, jord og luft	Øk/materiell	Omdømme
E Svært Alvorlig	Død	Svært langvarig og ikke reversibel skade	Drifts- eller aktivitetsstans >1 år.	Troverdighet og respekt betydelig og varig svekket
D Alvorlig	Alvorlig personskade. Mulig uførhet.	Langvarig skade. Lang restitusjonstid	Driftsstans > ½ år Aktivitetsstans i opp til 1 år	Troverdighet og respekt betydelig svekket
C Moderat	Alvorlig personskade.	Mindre skade og lang restitusjonstid	Drifts- eller aktivitetsstans < 1 mnd	Troverdighet og respekt svekket
B Liten	Skade som krever medisinsk behandling	Mindre skade og kort restitusjonstid	Drifts- eller aktivitetsstans < 1uke	Negativ påvirkning på troverdighet og respekt
A Svært liten	Skade som krever førstehjelp	Ubetydelig skade og kort restitusjonstid	Drifts- eller aktivitetsstans < 1dag	Liten påvirkning på troverdighet og respekt

Risikoverdi = Sannsynlighet x Konsekvens
Beregn risikoverdi for Menneske. Enheten vurderer selv om de i tillegg vil beregne risikoverdi for Ytre miljø, Økonomi/materiell og Omdømme. I så fall beregnes disse hver for seg.

Til kolonnen "Kommentarer/status, forslag til forebyggende og korrigerende tiltak":
Tiltak kan påvirke både sannsynlighet og konsekvens. Prioriter tiltak som kan forhindre at hendelsen inntreffer, dvs. sannsynlighetsreduserende tiltak foran skjerpet beredskap, dvs. konsekvensreduserende tiltak.

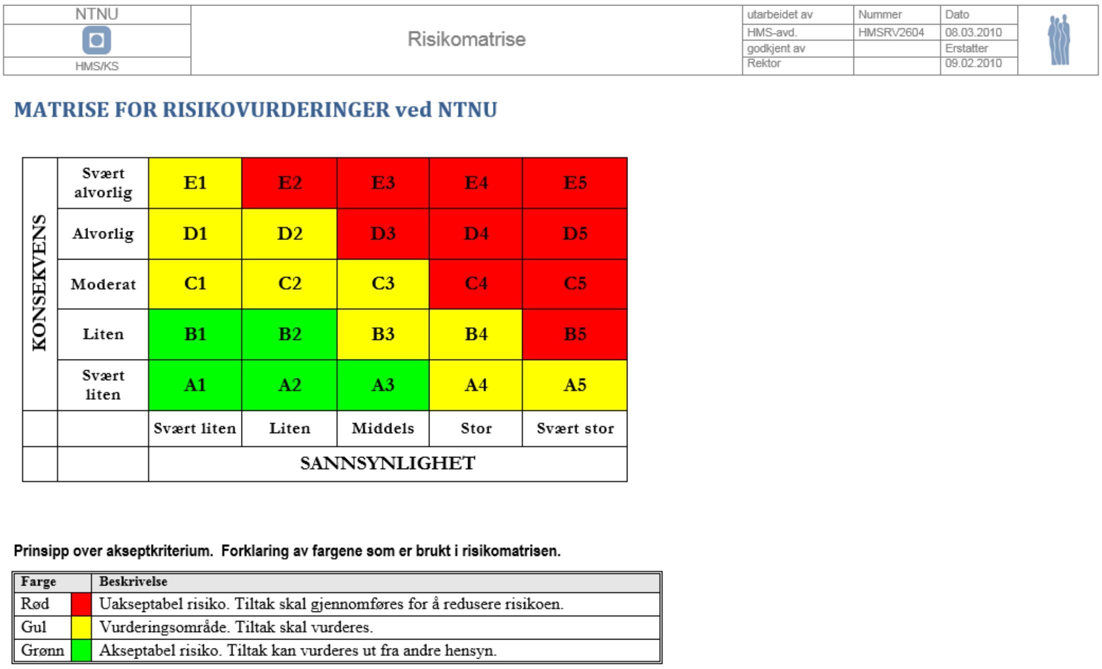

NTNU HMS/KS	Risikomatrise	utarbeidet av HMS-avd.	Nummer HMSRV2604	Dato 08.03.2010
		godkjent av Rektor		Erstatter 09.02.2010

MATRISE FOR RISIKOVURDERINGER ved NTNU

KONSEKVENS	Svært alvorlig	E1	E2	E3	E4	E5
	Alvorlig	D1	D2	D3	D4	D5
	Moderat	C1	C2	C3	C4	C5
	Liten	B1	B2	B3	B4	B5
	Svært liten	A1	A2	A3	A4	A5
		Svært liten	Liten	Middels	Stor	Svært stor
		SANNSYNLIGHET				

Prinsipp over akseptkriterium. Forklaring av fargene som er brukt i risikomatrisen.

Farge		Beskrivelse
Rød	🟥	Uakseptabel risiko. Tiltak skal gjennomføres for å redusere risikoen.
Gul	🟨	Vurderingsområde. Tiltak skal vurderes.
Grønn	🟩	Akseptabel risiko. Tiltak kan vurderes ut fra andre hensyn.